Benjamin Siebers

Spectroscopy of excitons in CdSe/CdS colloidal nanocrystals

Spectroscopy of excitons in CdSe/CdS colloidal nanocrystals

Dissertation

presented to the Faculty of Physics of the
TU Dortmund University, Germany,
in partial fulfillment of the requirements
for the degree of

Doktor rer. nat.

by
Benjamin Siebers

technische universität
dortmund

Dortmund, January 2015

Day of the oral examination: 17.04.2015

Examination board:

Prof. Dr. Dmitri Yakovlev
Prof. Dr. Heinz Hövel
Prof. Dr. Gudrun Hiller
Dr. Bärbel Siegmann

Contents

Chapter 1

Motivation

The awarding of the Nobel prize in physics in 2014 to Akasaki, Amano and Nakamura for the development of blue light-emitting diodes (LEDs) accounts for the great importance of lighting applications in modern society, which is also obvious from the huge share of lighting in power consumption [1] or the wide distribution of display technologies in notebooks, televisions, tablets or smartphones. Thus, fundamental research in this area to exploit opportunities for efficiency and ecological sustainability is highly desirable. In this regard, the achievement of group III/nitride based blue LEDs enabled to produce white light sources with unprecedented efficiency and lifetime. [2] Apart from the material, the optical emission wavelength of semiconductors can be altered by varying the crystal size, if this size is comparable to the de Broglie wavelength of the excited carriers. This phenomenon is termed the "quantum size effect". [4–8] One type of semiconductor structures, which utilize this effect, are colloidal nanocrystals (NCs). These structures have been intensely theoretically and experimentally studied throughout the last three decades, because of their great potential for application in optoelectronic devices, including LEDs, photodetectors or solar cells. [1, 3, 9–14] Notably, the first commercial television, which utilizes colloidal NCs, appeared on the market in 2013. [15]

From a different perspective NCs are especially interesting because many of the electronic and optical processes occuring in these structures are closely related to quantum mechanics, which has become the fundament of modern physics throughout the 20th century. The ability to fabricate nanometersized structures with a high degree of precision greatly extends the possibilities to explore and to make use of quantum mechanical effects, which include for example the already mentioned quantum size effect, the generation of entangled photons [16] or spin related phenomena, such as the exchange interaction. [7] The study and understanding of these phenomena eventually may help to develop novel devices utilizing quantum computing or spin electronics (spintronics), [17–22] concepts, which are just beginning to enter and will maybe revolutionize information technology.

Historically, the ample interest in colloidal NCs began with the observation of the quantum size effect. Like for many other physical phenomena, its experimental discovery in 1983 occurred by accident, when Louis E. Brus and co-workers studied redox reactions on the surface of photoexcited semiconductors. Notably, in order to increase the surface to volume ratio Brus used colloidal dispersed semiconductor clusters and he observed a decrease of the optical band gap over time. He attributed this effect to a change of particle size, due to aggregation of the particles, leading to a varying confinement energy, which results from the Heisenberg uncertainty principle. [4, 23] This newly discovered effect turned out to be useful for optical applications, since it allows to tune the optical band gap of the emitting or absorbing particle by just varying its size, while its material composition remains unchanged. [24] Because NCs, due to the confinement exhibit discrete absorption spectra, they are termed "artificial atoms" and are considered to constitute, in a sense, a new type of matter. [25]

The study by Brus et al. was followed by many experimental and theoretical studies exploring the consequences of the dielectric confinement for photoexcited charge carriers in colloidal NCs, especially for excitons. [5–8, 26–28] The description of the exciton energy structure and its dependence on the NC size, shape and material was of central interest, since it decides fundamental optical properties of NCs. Notably, in this regard the experimental and theoretical discovery of the "dark exciton", which constitutes the exciton ground state in spherical NCs made of cadmium selenide (CdSe) and which therefore strongly affects exciton radiative recombination in NCs, is a milestone in NC research. [28, 29]

The persistent interest in NCs was driven by the continuously improving methods for NC fabrication. For example, apart from high degrees of monodispersity, which could be achieved by colloidal synthesis, [30] methods for growing heteronanostructures, which consist of several materials, [31] or techniques for synthesizing NCs with anisotropic shape, such as nanorods [32] and dot-in-rods (DiRs) [31] have been developed. Importantly, the growth of a shell of different material with a larger band gap around a spherical core led to a considerable improvement of the radiative properties of the NCs, [33–35] which suffered from photoluminescene (PL) intermittency (also known as "blinking") due to Auger processes for a long time, resulting in poor luminescence quantum yield. [25]

Although the benefits of core/shell structures for the luminescence quantum yield were realized already in 1987, [33] the consequences for excitonic processes, notably the exciton relaxation and recombination dynamics as well as the construction of the fine structure are still being investigated nowadays. This thesis aims to contribute to a better understanding of these aspects. Its content and structure is described in the following.

In chapter 2, essential findings of preliminary studies on CdSe colloidal NCs are summarized, in order to provide the knowledge required for understanding the experimental and theoretical results presented later on.

The description of the experimental methods and an overview of the investigated samples as well as details on their synthesis are provided in chapter 3.

One central point of interest of this study is, how the construction of a NC affects its optical properties. The use of a core/shell design for the NC allows to manipulate the dielectric confinement of the electron or the hole individually. Thereby their location inside the nanostructure can be controlled by using specific material combinations. This eventually gives the ability to control the degree of their interaction and thereby affect the exciton fine structure as well as exciton recombination dynamics and greatly extends the possibilities to taylor the optical properties of a NC. [8, 24, 36–38] The experimental study presented in chapter 4 elucidates the role of the shell shape in this regard. To this end, spherical CdSe cores of several sizes, which are surrounded by cadmium sulfide (CdS) shells with varying shapes, were studied by time-resolved PL spectroscopy at low temperatures, at which fine structure effects in this material can typically be observed.

Chapter 5 presents a study of exciton spin relaxation and PL polarization in core/shell NCs subject to an external magnetic field. The application of a magnetic field leads to a Zeeman splitting of fine structure states and gives rise to spin relaxation processes of excitons and circular polarized PL. Spin relaxation in nanostructures is of great interest nowadays, because this process is of fundamental importance for spintronic applications. [19, 20, 39–41] In general, nanostructures with confinement in all three spatial dimensions (e.g. quantum dots or NCs) are promising candidates for spin-memory applications, since the interaction of the carrier spin with the environment, due to the discrete energy level structure inside of the NCs, is comparatively weak. [40] However, the processes, which lead to the relaxation of the charge carriers spin are still poorly understood. Especially studies on colloidal NCs in this regard are rare, although NCs offer a couple of advantages over self-assembled substrate-bound quantum dots, such as an improved spatial confinement, resulting in more effective isolation from the environment, or a more flexible processability. [42] Thus, studies, which elucidate the mechanisms giving rise to spin relaxation in NCs, are needed. In this thesis it is examined how spin relaxation in an external magnetic field depends on the geometrical parameters in core/shell NCs, i.e. the core size and the size and shape of the shell. Such information can be useful for the design of spin-preserving environments and the usage of NCs in spin-based storage devices. The dependence of the ensemble PL polarization on magnetic field, temperature and NC shape was subject to several magneto-optical PL experiments [43–45] and has been mathematically described for spherical NCs. [43] However, some experiments reported surprisingly low circular polarization degrees (DCPs) compared to theoretical predictions. [44, 45] In DiRs, as will be shown in this thesis, this is also the case. Therefore, the common model for describing the circular polarization of ensemble PL in magnetic field requires modification. In this thesis it is shown that the strongly varying DCPs observed in experiments can be explained by a theoretical model, which extends the common model and takes into account the exciton fine structure as well as a dielectric enhancement effect, which can occur in anisotropic NCs or core/shell NCs with anisotropic shell shapes. [46, 47]

Chapter 6 is dedicated to the discussion of mechanisms, which enable the radiative recombination of the dark exciton. The exciton ground state in spherical CdSe NCs is termed "dark", because its radiative recombination is principally forbidden in the electric dipole approximation. This results from the necessity of conservation of angular momentum during the transition from the excited to the vacuum state: The exciton ground state in spherical NCs has an angular momentum projection of $F = \pm 2$, whereas a photon has an angular momentum of 1. Therefore, recombination accompanied solely by the emission of a single photon cannot fulfill the momentum conservation requirement. This theoretically results in an infinite lifetime of an exciton in its ground state. However, it has been shown, that the radiative recombination is possible by coupling of the exciton to acoustic and optical phonons, which take a part of the angular momentum, or by the mixing of optically-forbidden (dark) and optically-allowed (bright) states by a magnetic field. [28] The observation of a zero phonon line, which increases with the application of an external magnetic field, in fluorescence line narrowing (FLN) experiments on CdSe NCs demonstrated the importance of the latter mechanism. [48] Since the zero phonon line can be observed also in the absence of an external magnetic field, internal fields have to be present, which lead to the mixing of dark and bright excitons. The origin of these fields still remains unclear, although it has been widely debated in the past three decades. A recent theoretical study proposes dark exciton radiative recombination resulting from the interaction between excitons and surface dangling bonds. [157] Here, the radiative recombination occurs by a simultaneous spin flip of electron and dangling bond spins, converting the initial dark state into a virtual bright state, which can radiatively recombine. Further, this theory predicts the formation of a state termed "dangling-bond magnetic polaron" (DBMPs), due to dynamical dangling bond spin polarization resulting from the carrier-dangling bond interaction. It is assumed, that this polarization leads to a suppression of dangling bond assisted dark exciton radiative recombination at low temperatures. In this work, experimental results are presented, which support the picture of dangling bond-assisted dark exciton radiative recombination and the formation of a DBMP in CdSe NCs.

In chapter 7 a summary of the results and an outlook on future studies is given.

Chapter 2

Fundamentals of CdSe nanocrystals

This chapter summarizes essential results of previous scientific work on CdSe based semiconductor NCs, which are important for the understanding of the relevance and the discussion of the experimental findings presented in this thesis. In the beginning of this chapter the architecture and synthesis of colloidal NCs are briefly described. As was stated in the motivation, the focus in this thesis is laid on processes related to the exciton fine structure, therefore in the second part of this chapter emphasis is given to the discussion of its origin. On the one hand, this requires the description of the crystal structure of the material, since it determines fundamental electronic and optical properties. On the other hand, quantum mechanical effects, such as quantum confinement and the electron-hole (eh) exchange interaction, which occur and are enhanced in nanometer-sized crystals and therefore strongly affect excitonic processes, are equally important. The study of exciton spin dynamics and PL polarization is accomplished by application of an external magnetic field, therefore its effect on the exciton fine structure is discussed as well. In the third part of this chapter exciton dynamics in NCs is reviewed with special attention to spin relaxation processes. Finally, the dependences of the PL polarization on the exciton fine structure and on the shape of the nanoparticles are discussed.

2.1 Synthesis and structural properties

Nanocrystals are tiny crystals with spatial extensions in the range of nanometers and typically such crystals consist of hundreds to a few thousands of atoms. If the size of the electronic host material encounters the regime of the Bohr radius of the excited carriers, quantum mechanical effects, such as quantum confinement, start to occur and offer new abilities for electronic and optical applications. One important result of this confinement is the size dependent energy gap: By varying the size of the NC, one can modify the absorption and emission energies of the particles without changing their chemical composition. [24]

Nanometersized crystals can be fabricated by different methods, such as molecular-beam-epitaxy or metalorganic-chemical-vapor-deposition. However, in the last two decades the production of NCs by colloidal or "wet chemical" synthesis has become more and more popular, since it provides an alternative to the aformentioned techniques, which is comparatively easy to accomplish, cheap and very suitable for mass production. In this technique metal-organic precursors are injected into a hot coordinating solvent, resulting in thermal decomposition of the precursor reagents and supersaturation of the solution. This process is followed by nucleation of particles, whose growth is further controlled by adding additional monomers with sufficiently small concentration to prevent further nucleation. [30] A more detailed description of the chemical synthesis of the particles investigated in this thesis is given in chapter 3. The outcome of this synthesis are "free standing" nanoparticles dispersed in a solvent. This is one aspect, which makes them very different from typically substrate-bound epitaxial produced nanostructures and favours processability for fabrication of NC based devices, for example by NC printing. [49]

Figure 2-1 (a) shows the common design of a colloidal NC. It consists of a core, which is typically overcoated by a second material of small lattice mismatch and with larger band gap. This shell confines excited carriers to the core and protects them from dangling bonds (i.e. unsatisfied valences at the surface atoms) or defects at the surface of the NC, which can act as carrier traps and therefore enhance nonradiative processes and thereby reduce the quantum yield. [35, 50] Passivation of the surface is further obtained by the addition of organic ligands, which constitute the outermost part of the NC. Apart from the chemical and electronic passivation of the surface, they prevent clustering of nanoparticles, determine the distance between neighboring NCs and they can be used as a "handle" for synthesizing NC assemblies such as superlattices or artificial solids. NC superlattices make use of the properties of individual NCs in combination with optical and electronical interactions between NCs in an ensemble. These interactions can be controlled by varying the interparticle spacing by choice of specific ligands. [24] The continuous improvement of NC growth techniques nowadays allows to produce NCs with size dispersions below 5%. [51] A typical transmission electron microscopy (TEM) image of an ensemble constituted by spherical NCs is depicted in Fig. 2-1 (b). Also complex structures, such as tetrapods, nanorods or heteronanostructures, which combine a spherical core with a rod-shaped shell, commonly termed dot-in-rod (DiR), can be fabricated by directional growth techniques. [31] A typical TEM image of DiRs is depicted in Fig. 2-1 (c).

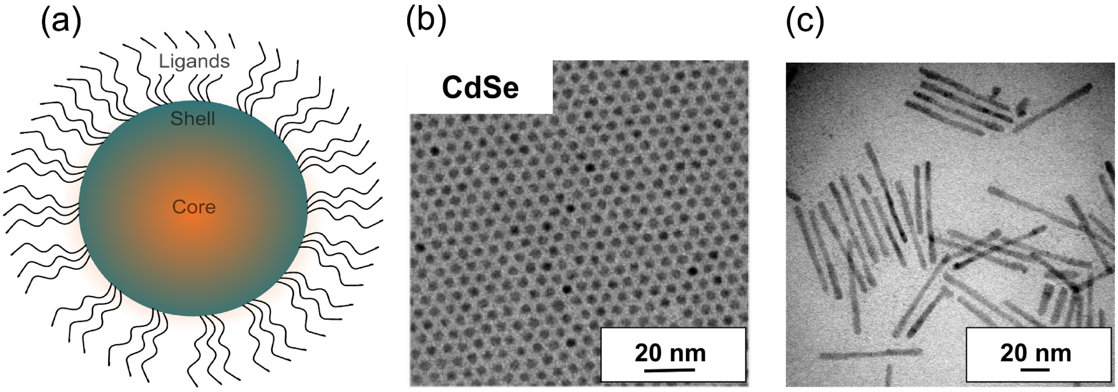

Figure 2-1: (a) Sketch of a spherical colloidal core/shell NC and TEM images of (b) spherical CdSe NCs (adapted from Ref. [24]) and (c) core/shell CdSe/CdS dot-in-rod NCs.

2.2 Electronic structure

During the past three decades CdSe has been the material of choice for the synthesis of NCs and it is the most studied material system for NCs nowadays. It allows to tune the optical band gap by changing the particle size throughout the full visible spectral range, [13] narrow size dispersions can be achieved, [30] it can be combined fairly easy with a wide range of other materials and due to its anisotropic crystalline form in case of wurtzite CdSe is suitable for directional growth. [52]

CdSe is a II-VI binary compound semiconductor and it occurs in three different crystalline forms, namely in zincblende-, NaCl- and wurtzite-structure. In the following only the wurtzite type will be discussed, since all crystals investigated in this thesis exhibit this crystal structure.

2.2.1 Crystal- and energy band-structure

Figure 2-2 (a) shows a sketch of the crystalline architecture of wurtzite CdSe. Each rhomboedric unit cell contains four atoms, two Se^{2-} anions located at $\mathbf{t_1} = (0,0,0)$ and $\mathbf{t_2} = (a_0/\sqrt{3}, 0, c_0/2)$, as well as two Cd^{2+} cations at $\mathbf{t_3} = (a_0/\sqrt{3}, 0, c_0/8)$ and $\mathbf{t_4} = (0, 0, 5c_0/8)$. The lattice constants are $a_0 = 4.2985$ Å for the hexagonal side and $c_0 = 7.0152$ Å along the z-direction. Each ion has four next neighbors forming tetrahedal s-p^3-bonds. [53, 54] Figure 2-2 (b) shows the first Brillouin zone with high symmetry points.

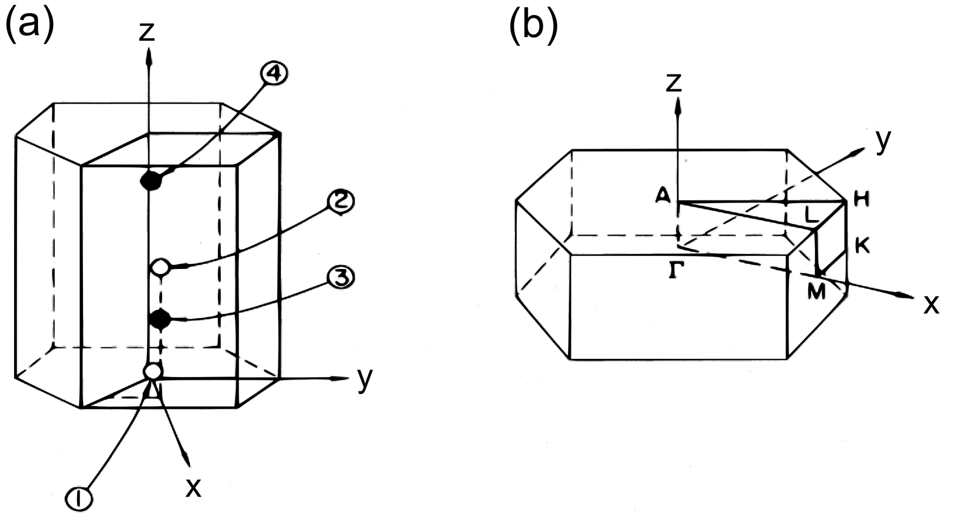

Figure 2-2: (a) Wigner-Seitz cell and (b) first Brillouin zone of wurtzite CdSe. Empty circles are cation sites, solid circles are anion sites. The numbers are indices of the four unit cell atoms. Capital letters denote the high symmetry points of the Brillouin zone. Adapted from Ref. [53].

According to Bloch's theorem a particle inside a crystalline solid can be described in terms of Bloch-functions

$$\psi_{n\mathbf{k}}(\mathbf{r}) = e^{i\mathbf{kr}} u_{n\mathbf{k}}(\mathbf{r}), \tag{2.1}$$

where $u_{n\mathbf{k}}(\mathbf{r}) = u_{n\mathbf{k}}(\mathbf{r} + \mathbf{T})$ is a function with the periodicity of the crystal lattice with

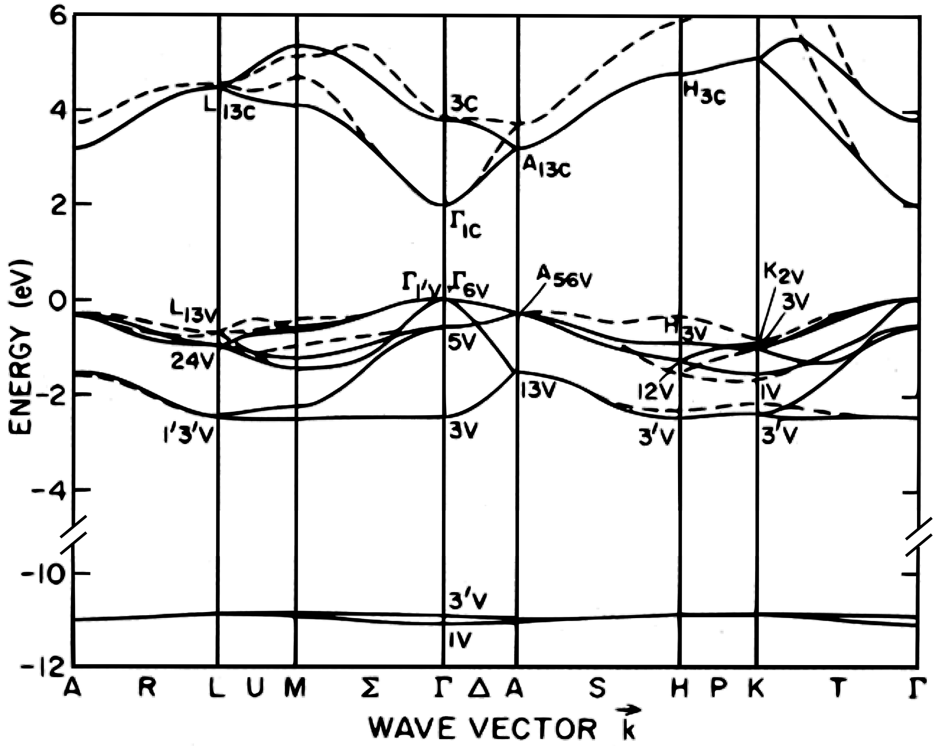

Figure 2-3: Semi-empirical tight-binding calculation of the band structure of wurtzite CdSe. Adapted from Ref. [53].

the Bravais-lattice vector **T**. The wavevector **k** lies in the first Brillouin-zone. [55] By solving the single particle Schrödinger equation

$$\hat{H}\psi_{n\mathbf{k}}(\mathbf{r}) = \left(-\frac{\hbar^2}{2m_0}\nabla^2 + V_{lattice}(\mathbf{r})\right)\psi_{n\mathbf{k}}(\mathbf{r}) = E_{n\mathbf{k}}\psi_{n\mathbf{k}}(\mathbf{r}) \tag{2.2}$$

for the carrier wavefunction $\psi_{n\mathbf{k}}(\mathbf{r})$, the energy eigenvalues $E_{n\mathbf{k}}$ can be calculated. In Eq.(2.2) $V_{lattice}(\mathbf{r}) = V_{lattice}(\mathbf{r}+\mathbf{T})$ is the crystalline periodic potential. The energy values $E_{n\mathbf{k}}$ for fixed n are called energy bands.

Within the tight-binding model, it is assumed, that electrons are tightly bound to their ionic cores and that the interaction with other atoms is small. In this case the Bloch-functions for electrons inside the crystal are taken to be linear combinations of localized atomic wavefunctions $\phi_n(\mathbf{r})$:

$$\psi_{n\mathbf{k}} = \sum_{\mathbf{T}} a_{\mathbf{kT}}\phi_n(\mathbf{r}+\mathbf{T}). \tag{2.3}$$

Figure 2-3 shows a tight-binding calculation of the CdSe energy band structure. Most important, the energetically lowest conduction band state and the highest valence band state occur at $\mathbf{k} = 0$, the center of the Brillouin zone, which is termed Γ-point. Therefore, CdSe has a direct band gap and the optical properties of CdSe can be described by considering only the dispersion in the vicinity of Γ, which is done in the following.

Two effects lead to a rather complex structure of the valence band at the Γ-point, namely the crystal field splitting and the splitting due to the spin-orbit interaction. The

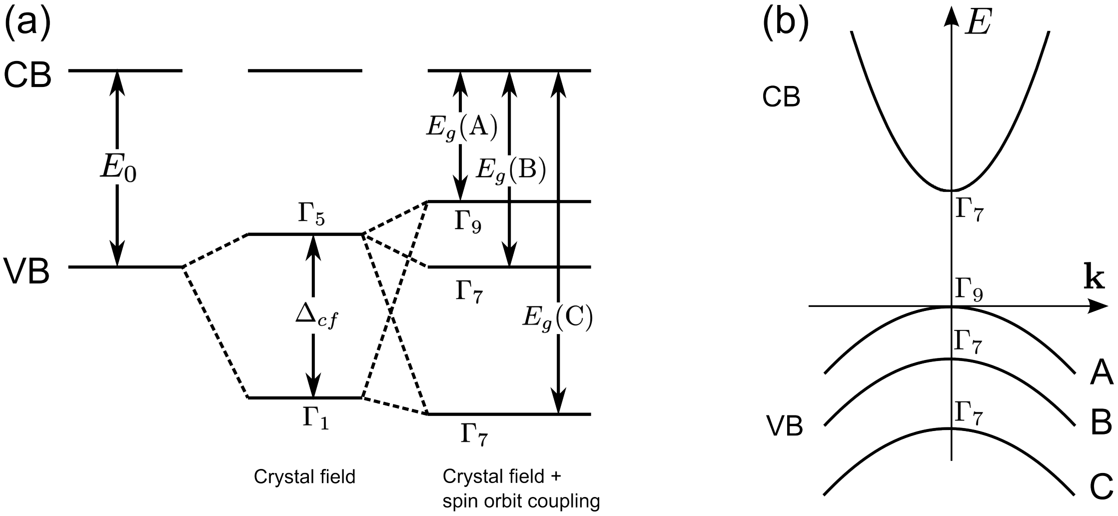

Figure 2-4: (a) Effects of the crystal field and the spin orbit coupling on the energy level structure at the Γ-point of CdSe. The left part shows the crystal field impact, the right one the combined case of crystal field splitting and the spin orbit coupling. Adapted from Ref. [57]. (b) Sketch of the band structure in the vicinity of the Γ-point. Adapted from Ref. [58].

origin of the crystal field splitting lies within the anisotropy of the hexagonal lattice and the spin orbit interaction is induced by coupling of the electron (or hole) spin with the magnetic moment induced by the carrier motion. The valence band states are derived from the 4p orbitals of Se and therefore have an orbital angular momentum $l = 1$, while the conduction bands origin is the 5s orbital of Cd and has $l = 0$. As a result the lowest conduction band state is spatially isotropic and is twofold degenerate with respect to the electron spin. As was calculated by Hopfield within a quasi-cubic model, the p_z-orbital in the valence band is subject to an energy shift different from that of the p_x- and p_y-orbitals due to the crystal field along the z-direction, which arises from the crystal asymmetry. [56]

The spin orbit interaction Hamiltonian can be expressed as

$$\hat{H}_{so} = -\frac{\hbar}{4m_0^2c^2}\boldsymbol{\sigma} \cdot \hat{p} \times (\nabla V) \,, \tag{2.4}$$

where $\boldsymbol{\sigma}$ is the spin operator and $\hat{p}$ the momentum operator. The spin orbit interaction splits the valence band states with total angular momentum $J = 1/2$ and $J = 3/2$, where $J = L + S$. [59]

The result of both combined effects are three valence subbands labeled A (Γ_9), B (Γ_7) and C (Γ_7), ordered in decreasing energy, as depicted in Fig. 2-4 (a). [57] The expressions Γ_i are the irreducible representations in Koster-notation, describing the symmetry transformation properties of the bands. [60] The order of magnitude of these effects are $\Delta_{cf} \approx 24$ meV for the crystal field splitting and $\Delta_{so} \approx 430$ meV for the spin-orbit splitting. [61] Due to the magnitude of the latter splitting, band C can typically be neglected when the radiative recombination of excitons in CdSe is discussed. As sketched in Fig. 2-4 (b), the valence bands as well as the conduction bands are approximately parabolic near the Γ-point. [58] The curvature of the bands in this regime is related to the effective mass of the particles by the equation

$$\left(\frac{1}{m_{eff}}\right)_{i,j} = \frac{1}{\hbar^2}\frac{\partial^2 E(\mathbf{k})}{\partial k_i \partial k_j}\bigg|_{\mathbf{k}=0} \qquad i,j = x,y,z. \tag{2.5}$$

Band A, constituted by holes with total angular momentum projection $|M| = 3/2$, is called the “heavy hole (hh)” band and band B with $|M| = 1/2$ is called the “light hole (lh) band”. Band C is often referred to as the “split-off (so) band”. Typically, the effective masses are highly anisotropic in wurtzite type crystals, leading to a lower effective mass perpendicular to the hexagonal c-axis in comparison to the parallel case. [58]

2.2.2 Quantum confinement in heteronanostructures

The basic optical properties of bulk CdSe can be understood with the model described above. However, when the size of the crystal is decreased into the nanometer-range, quantum mechanical effects occur and can strongly affect the optical and electronic properties. The most prominent one is the quantum size effect, which is discussed in the following.

Heisenbergs uncertainty principle states, that it is impossible to know the exact position and the exact momentum of a particle at the same time. This may be expressed as $\Delta x \Delta p \geq \hbar/2$. If an energy barrier, constituted for example by the surface between a crystal and its surroundings, confines a particle in space to the length x, the uncertainty of its momentum is on the order of $\hbar/x$. This uncertainty in momentum leads to an additional kinetic energy term and this is called the “confinement energy”. If the extension of the potential well is comparable to the de Broglie wavelength of the particle, the resulting energies for the particle are quantized and are inversely proportional to the quadratic size of the well

$$E_n \propto \frac{1}{x^2}, \tag{2.6}$$

where x is the size of the potential well and n the state index. [62] As a consequence, one can alter the particle energies and thereby optical emission and absorption energies, which were previously determined by the material composition, by changing the size of the potential well (i.e. the crystal size). [5, 6]

The quantum confinement in core/shell colloidal NCs can analytically be investigated by a method described by Haus et al. in Ref. [8], which is based on a single band effective mass approximation and is sometimes referred to as the ”particle in a box model”. This approach is applicable as long as the carrier envelope function slowly varies on the length scale of the crystal lattice. [63, 64]

In the strong confinement regime, the Coulomb interaction between electron and hole can be neglected as a first approximation, because the confinement energies yield the dominant part of their energy. Electrons and holes are represented by their envelope wavefunctions. The Schrödinger equation for the respective envelope function in each band reads

$$\left(-\frac{\hbar^2}{2}\nabla \cdot \frac{1}{m_a}\nabla + V_a(\mathbf{r})\right)\psi_a = E_a \psi_a, \tag{2.7}$$

where m_a is the effective mass and the subscript $a = e, h$ denotes electron (e) or hole (h). The effective mass can depend on the region of the hetero-nanostructured particle. Figure 2-5 (a) depicts a sketch of a spherical particle with regions $n = 1 \ldots N$ with different

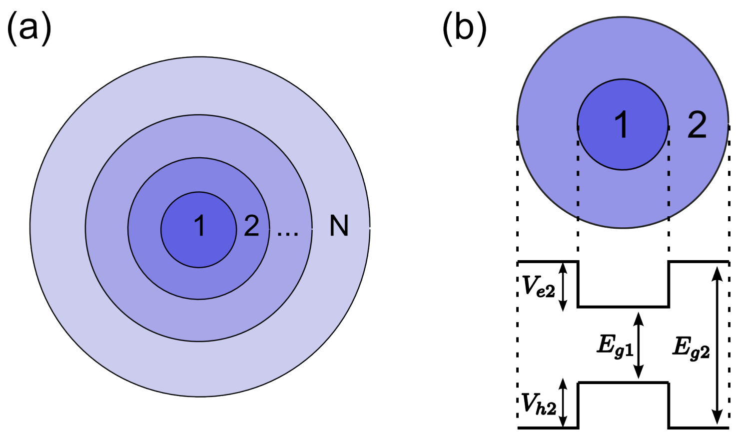

Figure 2-5: (a) Sketch of a spherical NC with N regions. (b) Conduction and valence band alignment for a core/shell particle. Adapted from Ref. [8].

potential values and different effective masses in each region. For a spherical symmetric particle the general analytical solution of Eq.(2.7) is

$$\psi_{lm}^{an} = [A_{lm}^{an} j_l(k_{an} r) + B_{lm}^{an} n_l(k_{an} r)] Y_{lm}(\theta, \phi), \tag{2.8}$$

where $j_l(z)$ and $n_l(z)$ are the spherical Bessel and Neumann functions and $Y_{lm}(\theta, \phi)$ are the spherical harmonics. The particle wavevector k_{an} can be written as

$$k_{an} = \left(\frac{2m_{an}(E_a - V_{an})}{\hbar^2} \right)^{\frac{1}{2}}, \tag{2.9}$$

where m_{an} is the effective mass of the electron or the hole and V_{an} is the valence band or conduction band potential in region n.

At the interfaces between succeeding regions of the particle, the following continuity equations for the wavefunction and the probability current must be fulfilled:

$$A_{lm}^{an} j_l(k_{an} r_n) + B_{ln}^{an} n_l(k_{an} r_n) = A_{lm}^{an+1} j_l(k_{an+1} r_n) + B_{lm}^{an+1} n_l(k_{an+1} r_n) \tag{2.10}$$

and

$$\begin{aligned} &\frac{k_{an}}{m_{an}} \left(A_{lm}^{an} j_l'(k_{an} r_n) + B_{ln}^{an} n_l'(k_{an} r_n) \right) = \\ &\frac{k_{an+1}}{m_{an+1}} \left(A_{lm}^{an+1} j_l'(k_{an+1} r_n) + B_{lm}^{an+1} n_l'(k_{an+1} r_n) \right). \end{aligned} \tag{2.11}$$

Typically NCs are surrounded by a medium with a small dielectric constant. Therefore one can assume that the carrier wavefunctions vanish at the boundary between the NC and its environment:

$$A_{lm}^{aN} j_l(k_{aN} r_N) + B_{lm}^{aN} n_l(k_{aN} r_N) = 0. \tag{2.12}$$

Through a recursion formula the wavefunction coefficients of the outer shell wavefunction are related to the inner ones. For a NC consisting of a core with radius R, which is surrounded by a single shell, as depicted in Fig. 2-5 (b), the coefficients of the shell are related to those of the core by:

$$A^{a2}_{lm} = -\frac{m_{a2}(k_{a2}R)^2}{k_{a2}}\left(\frac{k_{a2}}{m_{a2}}n'_l(k_{a2}R)j_l(k_{a1}R) - \frac{k_{a1}}{m_{a1}}n_l(k_{a2}R)j'_l(k_{a1}R)\right)A^{a1}_{lm} \tag{2.13}$$

and

$$B^{a2}_{lm} = -\frac{m_{a2}(k_{a2}R)^2}{k_{a2}}\left(\frac{k_{a2}}{m_{a2}}j'_l(k_{a2}R)j_l(k_{a1}R) - \frac{k_{a1}}{m_{a1}}j_l(k_{a2}R)j'_l(k_{a1}R)\right)A^{a1}_{lm}. \tag{2.14}$$

Here, the indices 1,2 denote the core and the shell, respectively. By substituting these coefficients into Eq.(2.12) the energies E_a can be calculated. Often one is interested in the lowest lying 1S states with $l = m = 0$. In this case the radial part of the carrier wavefunctions can be rewritten to

$$\Psi^a(r) = \begin{cases} N^a \frac{\sin(k_{a1}r)}{r\sin(k_{a1}R)} & \text{for } 0 \leq r < R \\ N^a \frac{\sin[k_{a2}(R+S-r)]}{r\sin(k_{a2}S)} & \text{for } R \leq r < R+S\ , \end{cases} \tag{2.15}$$

where the upper equation describes the electron or hole wavefunction in the core and the lower equation the respective wavefunction in the shell. S is the thickness of the shell and N_a is a normalization constant, which is derived from the condition, that the probability to find the carrier inside the NC volume is 1. The energy values for the 1S transition then can be derived as the lowest root from

$$(1 - k_{a1}R\cot(k_{a1}R))\frac{m_{a2}}{m_{a1}} = 1 + k_{a2}R\cot(k_{a2}S), \tag{2.16}$$

which follows from Eq.(2.12). [8, 36]

The described approach allows to approximate the quantum size levels of electrons and holes in core/shell NCs and also gives the ability to study their probability of presence inside different parts of the NC. Depending on the conduction and valence-band offsets [V_{e2} and V_{h2} in Fig. 2-5 (b)] between core and shell, the confinement of electrons and holes can be different, leading to a spatial separation of the carriers. This gives the ability to taylor the overlap of electron and hole wavefunctions and thereby control the strength of their interaction and probability of recombination. [8, 36, 65, 66] This field of research is sometimes referred to as ”band gap engineering” or ”wavefunction engineering”. By proper choice of materials with certain band gaps specific conduction and valence band alignments between core and shell can be achieved. This considerably extends the possibilities to tune optical properties of colloidal NCs, as will be discussed in detail in chapter 4.

2.2.3 Band-edge exciton fine structure

The particle-in-a-box model, which approximates the conduction and valence states as single isotropic and parabolic bands, can give only a rough approximation to the realistic electronic behaviour, since, as described in section 2.2.1, the real CdSe valence band structure is rather complex due to the internal crystal anisotropy and the spin-orbit interaction. Moreover, NCs in reality are never perfectly spherical and also the Coulomb interaction between electron and hole has been neglected so far.

The internal crystal anisotropy, the shape anisotropy and the eh-exchange interaction, which is found to be enhanced in nanostructures compared to bulk material, lift the degeneracy of the band-edge exciton ground state and give rise to an exciton fine structure, which gouverns the optical properties of the NC especially at low temperatures. The origin of the exciton fine structure in CdSe was extensively theoretically studied with different approaches, including tight-binding [67] or many-body pseudopotential calculations. [68] The following discussion, however, is based on the multiband effective mass theory, as reported by Efros et al. in Ref. [28].

Similar to the approach in the preceding section, the multiband effective mass approach starts from the spherical approximation (i.e. a spherically symmetric NC with cubic lattice structure). The conduction band ground state $1S_e$ is doubly degenerate with respect to its spin projection, while the valence band ground state is assumed to be of the type $1S_{3/2}$ and is fourfold degenerate with respect to its angular momentum projections $M = 3/2, 1/2, -1/2, -3/2$. The exciton ground state $1S_{3/2}1S_e$ is therefore eightfold degenerate in the spherical approximation.

As was discussed in section 2.2.1 the internal crystal field lifts the degeneracy of the valence band states with respect to $|M|$ and splits the hh and lh band by $\Delta_{cf} = 24$ meV in bulk CdSe. However, in NCs the magnitude of this splitting is reduced by approximately a factor of five compared to the bulk value. In case of NCs the splitting may be expressed as

$$\Delta_{int} = v(\beta)\Delta_{cf}, \tag{2.17}$$

where $v(\beta)$ is a dimensionless function, which depends on the ratio of the lh and hh effective masses β, which is $\beta = 0.28$ in CdSe. [69] The evolution of $v(\beta)$ is described in Ref. [28].

Real NCs are always slightly asymmetric, which leads to an additional splitting between hh and lh states. The asymmetry of the NC is quantified by the ellipticity $\mu = b/d - 1$ where d and b are the minor and major elliptical axes, respectively. In case of small ellipticity the resulting splitting of the lh and hh bands can be expressed as

$$\Delta_{sh} = 2\mu u(\beta)E_{3/2}(\beta). \tag{2.18}$$

Here, $E_{3/2}(\beta)$ is the energy of the hole ground state $1S_{3/2}$, which, due to quantum confinement, is inversely proportional to the square radius of the crystal. As a result, the splitting of the hole states, due to the shape asymmetry, is sensitive to the size of the NC. [70] The total splitting of the hh and lh bands is given as the sum of the crystal field splitting and the shape splitting $\Delta = \Delta_{sh} + \Delta_{int}$. Notably, the function $u(\beta)$, which is also given in Ref. [28], can have negative values. In case of prolate NCs ($\mu > 0$) this leads to a decreasing splitting between the hh and lh states with decreasing size. In small

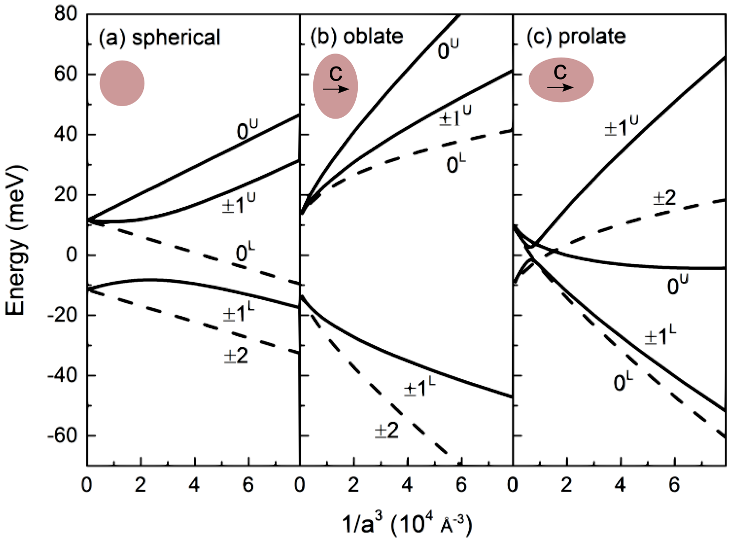

Figure 2-6: Dependence of the CdSe exciton fine structure on the NC radius a, calculated for various crystal shapes. Dashed lines correspond to optically inactive states, solid lines to optically active states. The indices U, L serve as labels for upper and lower states, respectively. The insets illustrate the geometry of the particle. The image is adapted from Ref. [74].

NCs hh and lh bands may even change the ordering, leading to an exciton ground state with $|M| = 1/2$. In the spherical and oblate ($\mu < 0$) case, however, the exciton ground state is always constituted by the heavy hole.

The exciton fine structure is further affected by the eh-exchange interaction, which can be considered as originated by the Coulomb interaction becoming spin-dependent. It arises from the necessity of an anti-symmetric wavefunction of two fermions with respect to interchange of location and spin. [71] The exchange Hamiltonian can be expressed as

$$\hat{H}_{exch} = -\frac{2}{3}\epsilon_{exch}(a_0)^3\delta(\mathbf{r}_e - \mathbf{r}_h)\boldsymbol{\sigma}\cdot\mathbf{J}, \tag{2.19}$$

where a_0 is the lattice constant, ϵ_{exch} is the exchange strength constant and $\boldsymbol{\sigma}$ and $\mathbf{J}$ are the electron and hole spin operators. The exchange interaction splits spin singlet and triplet states into an optically active state with total angular momentum $|F| = 1$ and an optically passive state with $|F| = 2$. In wurtzite crystals the magnitude of this splitting may be expressed as

$$\hbar\omega_{ST} = \frac{8}{3}\left(\frac{a_0}{a_{ex}}\right)^3 \epsilon_{exch}, \tag{2.20}$$

where a_{ex} is the bulk exciton Bohr radius. For bulk CdSe the exchange splitting is $\hbar\omega_{ST} = 0.12$ meV. [72] In NCs, however, since the strength of the interaction is proportional to the eh-wavefunction overlap and electrons and holes are closely spaced, the exchange splitting is strongly enhanced in nanostructures. As it was calculated by Takagahara and experimentally confirmed by Chamarro et al., for small NCs this enhancement is inversely proportional to the cubic NC radius. For a CdSe NC of size 3 nm the exchange energy calculates to $\hbar\omega_{ST} = 24$ meV. [7,73]

Altogether, the former 8-fold degenerate exciton ground state is split by the described effects into five exciton states, which constitute the exciton fine structure. The level ordering and the magnitude of the splitting between succeeding states strongly depends on the size and the shape of the NC, as shown in Fig. 2-6. [28] In spherical as well as oblate ($\mu < 1$) NCs the exciton ground state has a total angular momentum projection $F = \pm 2$, which is split from an energetically higher lying $F = \pm 1^L$ state by a couple of meV (see (a) and (b) in Fig. 2-6). The state with $|F| = 2$ is often referred to as the "dark exciton", since due to momentum conservation requirements it is optically inactive. However, as explained before, in prolate NCs the situation can change. In this case, for sufficiently small NCs the valence bands A and B switch their ordering and a lh state $|M| = 1/2$ becomes the hole ground state (see (c) in Fig. 2-6). This is a consequence of the anisotropy of effective masses in hexagonal crystals, as was pointed out at the end of section 2.2.1.

The dark exciton ground state plays a crucial role for the optical response of CdSe colloidal NCs, since in the electric dipole approximation radiative recombination from these state is forbidden, which should theoretically result in an infinite long radiative lifetime of the exciton ground state. Experiments, however, clearly demonstrate radiative recombination of these states with long but finite lifetimes on the order of μs at low temperatures. [48] The origin of dark exciton radiative recombination is not fully elucidated yet. Possible recombination pathways are, for example, optical phonon assisted recombination, where phonons take up a part of the angular momentum. However, fluorescence line narrowing experiments clearly demonstrate the existence of a zero phonon line (ZPL), suggesting an alternative recombination pathway apart from phonon assisted transitions. [28] One additional pathway for dark exciton radiative recombination occurs in the presence of an external or internal magnetic field. This aspect will be discussed in the following section.

2.2.4 Exciton fine structure in external magnetic fields

Due to the internal crystal anisotropy in wurtzite lattices and in NCs with shape anisotropy the rotational symmetry of the exciton spin is broken. As a result the hole and electron spins point in the direction of the hexagonal c-axis. Thus, the impact of an external magnetic field $\mathbf{B}$ is dependent on the angle between the field direction and the c-axis. [43] It can be described by the Hamiltonian [28]

$$\hat{H}_B = \frac{1}{2} g_e \mu_B \boldsymbol{\sigma} \cdot \mathbf{B} - g_h \mu_B \mathbf{J} \cdot \mathbf{B}, \tag{2.21}$$

where g_e and g_h are the electron and hole g factors of the $1S_e$ electron and the $1S_{3/2}$ hole state, respectively. μ_B is the Bohr magneton and σ and $\mathbf{J}$ are the electron and hole spin operators. If the magnetic field can be treated as a pertubation, i.e. when the Zeeman-splitting is small compared to the splittings between fine structure states, the resulting perturbation matrix

$$\hat{E}_H = \langle \psi_{\alpha,M} | \, \mu_B^{-1} \hat{H}_B \, | \psi_{\alpha',M'} \rangle \tag{2.22}$$

can be used to analyze the effect on the fine structure. Here, α and M denote the electron and hole angular momentum projections. The matrix elements can be written as

$$
\begin{array}{c|cccccccc}
 & \uparrow,3/2 & \uparrow,1/2 & \uparrow,-1/2 & \uparrow,-3/2 & \downarrow,3/2 & \downarrow,1/2 & \downarrow,-1/2 & \downarrow,-3/2 \\
\hline
\uparrow,3/2 & \frac{B_z(g_e-3g_h)}{2} & \frac{-i\sqrt{3}g_hB_-}{2} & 0 & 0 & \frac{g_eB_-}{2} & 0 & 0 & 0 \\
\uparrow,1/2 & \frac{i\sqrt{3}g_hB_+}{2} & \frac{B_z(g_e-g_h)}{2} & -ig_hB_- & 0 & 0 & \frac{g_eB_-}{2} & 0 & 0 \\
\uparrow,-1/2 & 0 & ig_hB_+ & \frac{B_z(g_e+g_h)}{2} & \frac{-i\sqrt{3}g_hB_-}{2} & 0 & 0 & \frac{g_eB_-}{2} & 0 \\
\uparrow,-3/2 & 0 & 0 & \frac{i\sqrt{3}g_hB_+}{2} & \frac{B_z(g_e+3g_h)}{2} & 0 & 0 & 0 & \frac{g_eB_-}{2} \\
\downarrow,3/2 & \frac{g_eB_+}{2} & 0 & 0 & 0 & \frac{-B_z(g_e+3g_h)}{2} & \frac{-i\sqrt{3}g_hB_-}{2} & 0 & 0 \\
\downarrow,1/2 & 0 & \frac{g_eB_+}{2} & 0 & 0 & \frac{i\sqrt{3}g_hB_+}{2} & \frac{-B_z(g_e+g_h)}{2} & -ig_hB_- & 0 \\
\downarrow,-1/2 & 0 & 0 & \frac{g_eB_+}{2} & 0 & 0 & ig_hB_+ & \frac{-B_z(g_e-g_h)}{2} & \frac{-i\sqrt{3}g_hB_-}{2} \\
\downarrow,-3/2 & 0 & 0 & 0 & \frac{g_eB_+}{2} & 0 & 0 & \frac{i\sqrt{3}g_hB_+}{2} & \frac{-B_z(g_e-3g_h)}{2}
\end{array}
$$

, where $B_\pm = B_x \pm iB_y$. Components of the magnetic field, which are perpendicular to the hexagonal c-axis (it is assumed to be the z-axis here) of the crystal lead to an admixture of the dark $F = \pm 2$ with the bright $F = \pm 1$ exciton states. Due to this admixture the dark exciton states gain oscillator strength and can radiatively recombine. This aspect will be of great importance for results presented in chapter 6.

A magnetic field parallel to the hexagonal c-axis lifts the degeneracy of the $F = \pm 2$ and $F = \pm 1$ states and leads to a Zeeman-splitting, which is proportional to the exciton g factor and the magnetic field strength

$$\Delta E_Z = g_{ex}\mu_B B\cos\Theta, \tag{2.23}$$

where Θ is the angle between the magnetic field and the hexagonal c-axis of the crystal. The exciton g factor g_{ex} is different for bright and dark exciton states and can be derived from the perturbation matrix, Eq.(2.22). Notably, for the dark exciton ground state it calculates as $g_{ex,2} = g_e - 3g_h$. [75] The $F = 0$ states exhibit no splitting in a magnetic field.

2.3 Exciton dynamics

The optical response of a NC strongly depends on the dynamics of excitons after excitation, as illustrated in Fig. 2-7. In general, the generation of eletrons and holes in semiconductors can be realized by different methods, for example by electrical injection or by optical excitation with a laser, which is considered in the following. When a semiconductor is excited by an incident light beam with an energy $\hbar\omega_{\mathrm{ex}} > E_g$, where E_g is the band gap energy, electrons are promoted from the valence to the conduction band and a hole is left in the valence band. If the energy of the incident light is larger than the energy of the lowest optically allowed excited state, one speaks of non-resonant excitation. The carriers are then promoted to energetically higher lying states and can be subject to several intraband relaxation processes before recombination. During the excitation process a photon of energy $\hbar\omega_{\mathrm{ex}} = E_g + \Delta E_{exc}$ is absorbed. The excess energy ΔE_{exc} is distributed among the electrons and holes in form of kinetic energy. The relaxation of the system then occurs in three steps. In the beginning, on timescales below 100 fs the carriers thermalize, i.e. they achieve a thermal equilibrium among themselves via carrier-

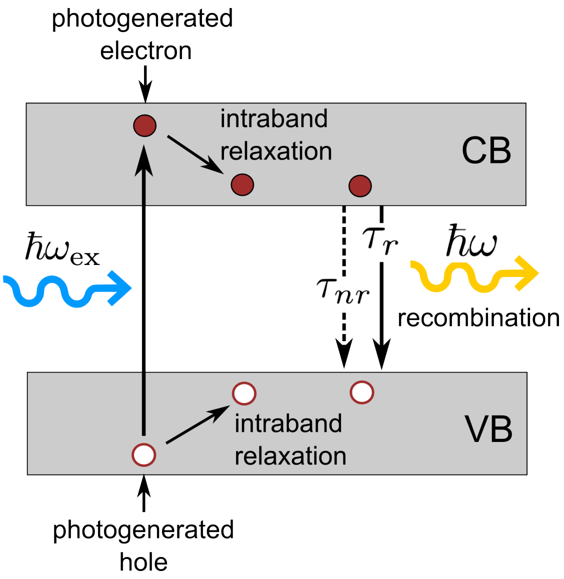

Figure 2-7: Illustration of photoexcitation, relaxation and subsequent radiative or nonradiative recombination of electrons and holes in semiconductors. Adapted from Ref. [77].

carrier scattering. If the temperature, which corresponds to the Boltzmann-distribution temperature of the carriers in thermal equilibrium, is higher than the temperature of the surrounding lattice, one speaks of “hot carriers”. In the second stage these carriers achieve thermal equilibrium with the lattice, this process is termed “carrier cooling”. In II-VI semiconductors, such as CdSe, this relaxation occurs due to interaction with longitudinal optical phonons (LO phonons) and longitudinal acoustic phonons (LA phonons). In the last step the carriers recombine radiatively or nonradiatively, with characteristic times τ_r and τ_{nr}, respectively. [76]

The focus of this thesis with respect to exciton dynamics lies on processes, which belong to the second and the third stage, namely the build-up of thermal equilibrium with the crystal lattice and subsequent radiative or nonradiative recombination. Importantly, in the presence of an external magnetic field spin relaxation, i.e. spin flip processes between Zeeman-split fine structure states, can be observed during the establishment of thermal equilibrium. These are of prominent interest in this study. In the following, the processes of intraband carrier relaxation, radiative and nonradiative recombination and exciton spin relaxation are reviewed in more detail.

2.3.1 Intraband relaxation

In bulk II-VI semiconductors the most important energy relaxation mechanism is the coupling to LO phonons via the Fröhlich-interaction. In NCs, however, phonon scattering is strongly suppressed because of restrictions imposed by the requirement of the conservation of momentum and energy. [78] While in bulk material the energy bands consist of a quasi-continuum of states in low-dimensional structures the energy levels are quantized and even in case of weak confinement are separated by at least a few meV. As will be explained in the following, this decreases the carrier-phonon scattering rate, which can be determined by Fermi's golden rule

$$\tau_{i\rightarrow f}^{-1} = \frac{2\pi}{\hbar} \int d^3q |M(q)|^2 \delta(E^f - E^i - \hbar\omega_q)(N_{\omega_q} + 1), \tag{2.24}$$

where i and f denote the initial and final state and $E^i - E^f = \hbar\Omega$ corresponds to the energy spacing of the initial and final state, respectively. $\hbar\omega_q$ is the phonon energy for a phonon with wavevector q and $M(q)$ is the electron-phonon scattering matrix element. N_{ω_q} is the thermal phonon distribution function. The energy spacing, because of energy conservation, defines the phonon energy and thereby the possible phonon wavevector q. As was shown in Ref. [79] for high q (i.e. $qL > 1$, where L is the lateral size of the NC) the interaction matrix element $M(q)$ for the scattering of the phonon and the carrier decreases, leading to a decreasing scattering rate for increasing energy spacings. [79, 80] In case of strong confinement the spacing between subsequent energy states can also easily exceed the typical LO phonon energy, which is 25 meV in CdSe NCs. [48] Therefore transitions can be mediated only by multi-phonon processes, which occur with much smaller probability, especially at low temperatures. [81] Moreover, the NC size also changes the phonon density of states (DOS), therefore low energy and long wavelength acoustic phonons are suppressed due to boundary conditions. [82–85] Both of these effects, although different in their origin, are sometimes referred to as a "phonon bottleneck effect". They are however similar in a way, that they hinder the energy relaxation of hot electrons and holes by phonons. For holes, though, because of their relatively high effective mass, the energy spacings between quantized states are one order of magnitude smaller compared to electrons and therefore hole-phonon scattering is believed to be much more efficient. [78, 86]

Nevertheless, experiments employing ultrafast transient absorption pump-probe techniques evidenced efficient electron energy relaxation on sub-picosecond timescale, which is the same order of magnitude compared to electron-phonon scattering in bulk material. [87, 88] Notably a faster relaxation was found for smaller NCs, which excludes a phonon-assisted mechanism, since the energy level spacings are much larger in this case. The fast relaxation rates were attributed to the occurrence of Auger-like thermalization, where the electron energy is transferred to the hole via the Coulomb interaction. The hole is then lifted to a higher energy state and subsequently relaxes via phonon-scattering through the quasi-continuum of valence band states. In NCs, due to their small size, the Coulomb interaction between electron and hole becomes much stronger compared to bulk material, therefore this type of eh-scattering plays a crucial role in these structures. [25, 86, 89] Both types of energy relaxation in NCs, namely phonon-assisted and Auger-relaxation, are illustrated in Fig. 2-8 (a) and (b), respectively.

2.3.2 Radiative recombination

Typically the intraband relaxation times in NCs are small compared to the radiative lifetime of excitons. [88] Thus after relaxation the excitons are in thermal equilibrium with the lattice and distributed within k_BT from the exciton ground state. Subsequently, the excitons recombine spontaneously, either radiatively or nonradiatively for example via Auger-processes.

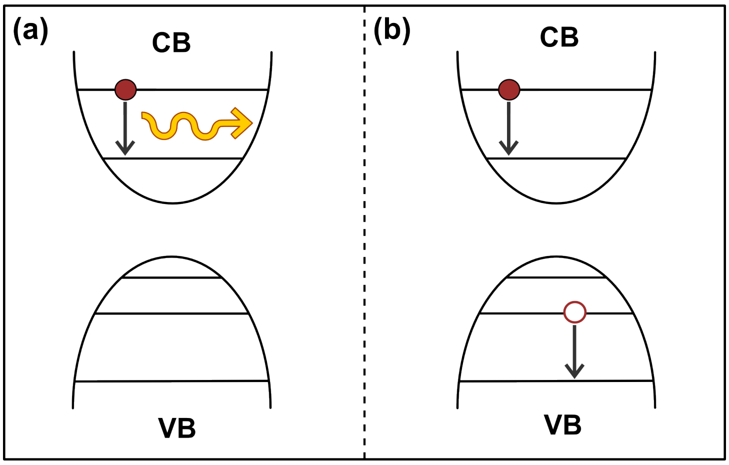

Figure 2-8: Illustration of (a) phonon-assisted electron relaxation and (b) Auger-relaxation.

In general, the spontaneous emission of excitons can be described by the rate equation

$$\frac{dN_2}{dt} = -A_{21}N_2, \tag{2.25}$$

where N_2 is the number of excitons, the index denotes the inital (2) and final (1) state and A_{21} is the Einstein coefficient for this transition. The probability for detecting a photon is proportional to the number of excitons in the excited state and to the Einstein coefficient. The solution of the rate equation is a single exponential decay $N_2(t) = N_2(0)\exp(-A_{21}t) = N_2(0)\exp(-t/\tau_r)$, where $\tau_r = 1/A_{21}$ is the radiative lifetime and $N_2(0)$ the initial population of the excited state at time $t = 0$. The radiative decay time of the excited state depends on the optical selection rules. [90]

The probability for radiative recombination of an exciton state with angular momentum projection F in the dipole approximation is

$$P = |\langle 0|\,\mathbf{e}\cdot\hat{p}\,|\psi_F\rangle|^2, \tag{2.26}$$

where $|0\rangle = \delta(\mathbf{r}_e - \mathbf{r}_h)$, $\mathbf{e}$ is the polarization vector of the emitted light and $\hat{p}$ is the momentum operator. ψ_F is the exciton wavefunction. The radiative lifetime of the fine structure states can be obtained from Eq.(2.26) by summing over all light polarizations. As shown in Ref. [28] the radiative rate for the $F = 0^U$ state calculates as

$$\frac{1}{\tau_0} = \frac{8\omega n_r P^2 K}{9 \times 137 m_0^2 c^2}. \tag{2.27}$$

Here, m_0 is the free electron mass, ω the frequency of the emitted light, n_r the refractive index and $P = \langle S|\,\hat{p}_z\,|Z\rangle$ the Kane interband matrix element. Importantly, the radiative rate is proportional to K, which is the square of the eh-overlap integral, and it does not depend on the crystal radius. The radiative rates of the $|F| = 1^{U,L}$ states are proportional to $1/\tau_0$, with a prefactor, which depends on the eh-exchange constant η and the splitting between hh and lh states Δ, which are size dependent. As mentioned before, radiative recombination from exciton states with $F = \pm 2$ is forbidden in the electric dipole approximation, since photons cannot have an angular momentum of ± 2, resulting in an infinitely long radiative lifetime. In the presence of a magnetic field, however, it gains oscillator strength due to the admixture of optical allowed states. This leads to a shortening of the $F = \pm 2$ radiative lifetimes with increasing magnetic field. [28]

2.3.3 Spin dynamics

Spin dynamics occur throughout the equilibration of an excited spin system. In, general one distinguishes two processes: spin relaxation and spin dephasing. These two processes are characterized by a specific time T_1 and T_2 (the spin relaxation time and spin dephasing time), respectively. These can be derived from the phenomenological Bloch-Torrey equations, which describe the evolution of a magnetiziation $\mathbf{M}$ in time, in the presence of an external magnetic field. Neglecting diffusion, these can be written as

$$\frac{\partial M_x}{\partial t} = \gamma(\mathbf{M} \times \mathbf{B})_x - \frac{M_x}{T_2}, \tag{2.28}$$

$$\frac{\partial M_y}{\partial t} = \gamma(\mathbf{M} \times \mathbf{B})_y - \frac{M_y}{T_2}, \tag{2.29}$$

$$\frac{\partial M_z}{\partial t} = \gamma(\mathbf{M} \times \mathbf{B})_z - \frac{M_z - M_z^0}{T_1}, \tag{2.30}$$

where $\gamma = \mu_B g_e/\hbar$ is the electron gyromagnetic ratio with Bohr-magneton μ_B and electron g factor g_e. M_z^0 is the equilibrium magnetization in direction of the magnetic field (z-direction). [20] Spin relaxation is the change of the magnetization along the magnetic field direction and occurs by coupling to phonons. After relaxation the spin system is in thermal equilibrium with the lattice. Spin dephasing describes the loss of phase in an ensemble of spins, which were initially precessing in phase around the magnetic field. In the following only spin relaxation is considered in more detail.

In semiconductors there are four mechanisms, which are typically made responsible for spin relaxation. These are the D'yakonov-Perel, Elliot-Yafet, Bir-Aronov-Pikus and the hyperfine interaction mechanism.

The D'yakonov-Perel mechanism occurs in non-centrosymmetric structures, such as wurtzite CdSe, where the inversion symmetry is broken due to two distinct atoms in the Bravais lattice. The lack of inversion symmetry gives rise to an effective magnetic field $\mathbf{\Omega}(\mathbf{k})$, about which the electrons in the conduction band precess. By momentum scattering processes this effective magnetic field progressively changes its direction and this, in combination with the electron spin precession, causes spin relaxation.

In contrast, the Elliot-Yafet mechanism also occurs in centrosymmetric structures and results from the admixture of electronic states with opposite spin due to spin-orbit interaction, which is caused by the lattice ions. While in the absence of spin-orbit interaction the single-electron Bloch-functions are eigenstates of $\hat{\sigma_z}$, in the presence of spin-orbit coupling the eigenstate is a mixture of spin-up and spin-down. The strength of the admixture depends on the strength of the spin-orbit coupling, therefore in narrow gap semiconductors this effect is dominant. Spin relaxation in this case is caused by the variation of the admixture of the distinct spin-states, which occurs during momentum-scattering processes with impurities, boundaries or phonons. [20, 91]

The Bir-Aronov-Pikus mechanism describes the coupling of electron with the hole spin via the exchange interaction. The electron feels an effective magnetic field generated by the hole spin and the electron spin precesses about this field, which fluctuates and therefore gives rise to electron spin relaxation. The strength of the interaction between electron and hole depends on the eh-wavefunction overlap and is therefore especially relevant in nanometersized structures or heavily p-doped semiconductors at low temperatures. [20]

Finally, the hyperfine interaction gives rise to spin relaxation due to the magnetic interaction between electron spins and nuclei magnetic moments and is especially important in quantum confined structures, where the electron is strongly localized. Since electrons in bulk material travel long distances and experience the fields of many atoms, this effect averages out.

In low-dimensional semiconductors the D'yakonov-Perel and Elliot-Yafet mechanism are believed to be ineffective, due to the stong localization of the electron, which suppresses spin-orbit coupling. [20] In NCs, the hyperfine interaction and relaxation via the eh-exchange interaction were proposed to be most relevant. [92–95] However, only the long-range part of the eh-exchange interaction (anisotropic part) can mix opposite spin states. [96] While the anisotropic exchange interaction plays an important role for self-assembled quantum dots this type of interaction is typically neglected in fine structure calculations based on the effective mass approximation approach in spherical or nearly spherical NCs. [70] On the other hand, more recent studies predict a non-vanishing long range part also for CdSe NCs [97, 98] and several experimental studies evidence anisotropic exchange splittings in zero magnetic field, which were formerly observed only for self-assembled quantum dots. [99–102]

The aforementioned mechanisms could be relevant for relaxation between different spin states $|\pm 1, \pm 2\rangle$ during the thermal equilibration of the system. In the presence of an external magnetic field additional relaxation between the Zeeman-split sublevels occurs. In general, since during the relaxation process energy and angular momentum need to be conserved, spin relaxation requires an interplay of phonons and one of the described mechanisms. As will be discussed in chapter 5, in NCs and at low temperatures LA acoustic phonons play a central role in this regard.

2.4 Photoluminescence polarization

A specific polarization of the PL arises from the spin orientation of excitons, since angular momentum needs to be conserved during radiative recombination. Thus, the level ordering in the fine structure strongly affects the polarization properties of the PL at low temperatures, at which only the lowest lying exciton states are populated.

Transitions from exciton states with total angular momentum $F = 0$ to the ground state are linearly polarized parallel to the hexagonal axis of the NC. This is one reason for the high linear PL polarization typically observed for CdSe nanorods. [32, 47] In these structures, the linear polarized transitions are dielectrically enhanced, due to their anisotropic shape. This aspect will be discussed in more detail at the end of this section.

The PL from the $F = \pm 1$ exciton states is circularly polarized. However, since states with similar absolute value of angular momentum but opposite sign are energetically degenerate in general, the transitions from either one of these states occur with equal probability and thus the degree of circular polarization (DCP) of the low temperature

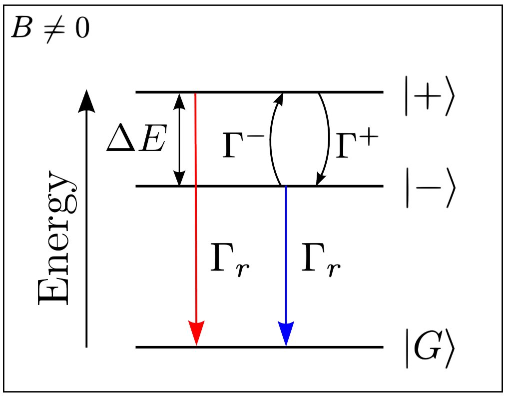

Figure 2-9: Sketch of a Zeeman-split fine structure state with relaxation and recombination pathways. Blue color corresponds to a $\sigma-$ and red color to a $\sigma+$ polarized transition.

PL detected in the experiment is typically zero. This changes with the application of an external magnetic field. As discussed in section 2.2.4, a magnetic field parallel to the hexagonal axis of CdSe NCs lifts the degeneracy of the $F = \pm 1$ and $F = \pm 2$ exciton states, giving rise to circular polarized PL. Its mathematical description is described in the following.

2.4.1 Circular polarization in external magnetic fields

The mathematical derivation presented here is adapted from Ref. [74]. Figure 2-9 shows a Zeeman-split exciton state at a given non-zero magnetic field. The magnitude of the splitting is denoted as ΔE, the states $|+\rangle$ and $|-\rangle$ are the Zeeman-sublevels with opposite spin orientation and $|G\rangle$ is the vacuum state. The rates Γ^+ and Γ^- are the spin relaxation rates from $|+\rangle$ to $|-\rangle$ and vice versa. The radiative recombination rate Γ_r is assumed to be equal for both states.

The dynamics of this three level system is described by the rate equations

$$\frac{dN^+}{dt} = -N^+(\Gamma_r + \Gamma^+) + N^-\Gamma^- + G^+(t) \tag{2.31}$$

$$\frac{dN^-}{dt} = -N^-(\Gamma_r + \Gamma^-) + N^+\Gamma^+ + G^-(t), \tag{2.32}$$

where N^+ and N^- are the populations of the Zeeman-sublevels and $G^+(t)$ and $G^-(t)$ are excitations from the vacuum state to either the upper or the lower Zeeman-sublevel, respectively. In the steady state regime, i.e. $dN^\pm/dt = 0$, the degree of spin polarization ρ_{ex} in this system can be expressed by

$$\rho_{ex} = \frac{N^- - N^+}{N^- + N^+} = \rho_0 \frac{\tau_r}{\tau_r + \tau_s}, \tag{2.33}$$

where $\tau_r = 1/\Gamma_r$ is the radiative decay time of the exciton states, $\tau_s = 1/(\Gamma^+ + \Gamma^-)$ is the spin relaxation time and $\rho_0 = (\Gamma^+ - \Gamma^-)/(\Gamma^+ + \Gamma^-)$. In case of nonresonant excitation by an infinitely short δ-pulse, where $N^+(t = 0) = N^-(t = 0) = N_0/2$, with the initial number of excitons N_0, the time evolution of the spin polarization is described by

$$\rho_{ex}(t) = \frac{N^- - N^+}{N^- + N^+} = \rho_0[1 - \exp(-t/\tau_s)]. \tag{2.34}$$

For large t, $\rho_{ex}(t) \rightarrow \rho_0$, where ρ_0 is the spin polarization in equilibrium. It can be described by a thermal Boltzmann-distribution

$$\rho_0 = \tanh(\Delta E/2k_BT). \tag{2.35}$$

The circular polarization of the PL of NCs in magnetic field arises from the exciton population of the Zeeman-split sublevels. For spherical CdSe NCs it is generally assumed, that the population of the dark exciton ground state is the relevant thermodynamic quantity, that radiative recombination occurs by coupling to the $F = \pm 1$ states and that the coupling between $F = +2$ and $F = +1$ states and between the $F = -2$ and the $F = -1$ states occur with equal probability. [43] According to the electric dipole approximation, the probability for detecting circular polarized light at an angle Θ with respect to the magnetic field axis is proportional to $(1 \pm \cos\Theta)^2$. [28] Thus, the $\sigma+$ and $\sigma-$ polarized intensities become angle dependent

$$I^{\pm} = 1 + x^2 \mp 2x\rho_0(B, x, T), \tag{2.36}$$

where $x = \cos(\Theta)$. [44] As discussed in section 2.2.4 the magnitude of the Zeeman-splitting due to the crystal anisotropy is angle dependent as well, therefore ρ_0 is a function of x. In thermal equilibrium the DCP of a single NC can be written as

$$p_c^{\mathrm{eq}} = \frac{I^+ - I^-}{I^+ + I^-} = -\frac{2x\rho_0(B, x, T)}{1 + x^2}. \tag{2.37}$$

The time-dependent DCP after pulsed excitation is then described by

$$p_c(t) = p_c^{\mathrm{eq}}[1 - \exp(-t/\tau_s)]. \tag{2.38}$$

In many experimental situations, one investigates not only single NCs but ensembles of many NCs with varying orientations, depending on the NC shape and the method of sample preparation. In case of spherical NCs one assumes a random distribution of c-axis orientations with respect to the magnetic field. In this case, one has to integrate expressions (2.37) and (2.38) over all possible angles:

$$P_c^{\mathrm{eq}} = -\frac{\int_0^1 2x\rho_0(B, x, T)dx}{\int_0^1 (1 + x^2)dx} \tag{2.39}$$

and

$$P_c(t) = P_c^{\mathrm{eq}}(1 - \exp(-t/\tau_s)). \tag{2.40}$$

Generally, an NC oriented parallel to the magnetic field axis can emit 100% circular polarized light. In contrast, a NC oriented perpendicular to the magnetic field shows no circular polarization, due to the vanishing Zeeman-splitting. In an ensemble of spherical NCs, where the angles between the hexagonal c-axis and the magnetic field are uniformly distributed between 0° and 90°, the maximal DCP, which can be observed, is 75%. [43]

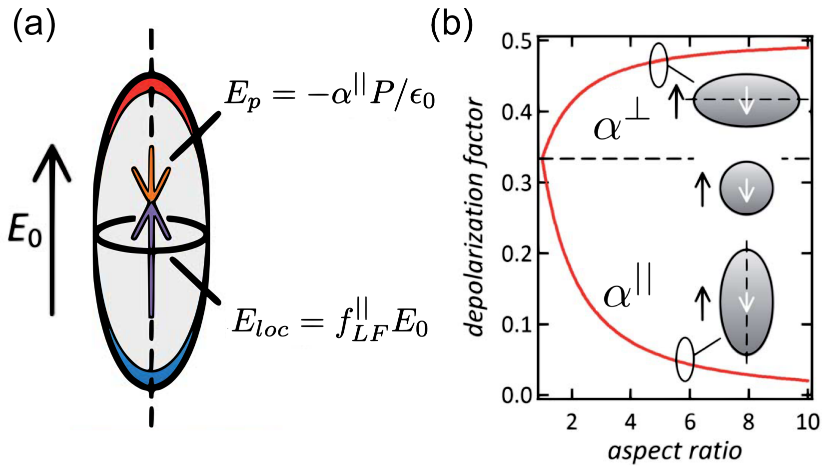

Figure 2-10: (a) Illustration of the depolarization effect in ellipsoidal nanoparticles. (b) Dependence of the depolarization coefficients $\alpha^{||}$ and $\alpha^{\perp}$ on the aspect ratio. Images are adapted from Ref. [104].

In experiments with continuous wave (CW) excitation or if one is not interested in exciton dynamics, the time-integrated DCP is measured. It can be shown that this is equal to

$$P_c^{\text{int}} = P_c^{\text{eq}} \frac{\tau_r}{\tau_r + \tau_s}. \tag{2.41}$$

In the limit $\tau_r >> \tau_s$, P_c^{int} and P_c^{eq} are equal. If, however, τ_s is comparatively large the time-integrated DCP can significantly deviate from the equilibrium DCP. [103]

2.4.2 Dielectric enhancement

Nanocrystals are never perfectly spherical. On the one hand, TEMs of spherical NCs reveal slight ellipticities, which typically become stronger for larger NCs. On the other hand, as mentioned already in section 2.1 NCs with more complex shapes, such as a rod shape for instance, can be fabricated by anisotropic growth methods.

Deviations from the spherical symmetry affect both light absorption and light emission by the so called "dielectric enhancement effect", which results from the large difference of the dielectric constant between the nanoparticle and the surrounding medium. This leads to a depolarization of absorbed and emitted light. The origin of this effect is illustrated in Fig. 2-10 (a). The NC is approximated as an ellipsoid. An external electric field E_0 parallel to the long axis of the NC induces an opposing field $E_P = -\alpha^{||}P/\epsilon_0$ inside the NC by polarization. Here, P is the polarization and $\alpha^{||}$ is the depolarization coefficient parallel to the long axis of the ellipsoid. Inside the NC the effective field (local field) E_{loc} is therefore smaller compared to E_0. The strength of this effect is described by the local field factor $f_{LF}^{||}$, which can be written as

$$f_{LF}^{||} = \frac{1}{(1-\alpha^{||}) + \alpha^{||}\kappa_s/\kappa_m}, \tag{2.42}$$

where κ_s and κ_m are the dielectric constants of the semiconductor and the surrounding medium, respectively. Due to the anisotropic shape, the described effect is different for the semi-major axis b and the semi-minor axis d of the ellipsoid, as illustrated in Fig. 2-10 (b). This figure shows the depolarization coefficients as a function of the aspect ratio (b/d) of the ellipsoid, as they are reported in Ref. [105]. In case of a sphere, the depolarization is equal for both directions, parallel and perpendicular to the light electric field. However, for fields perpendicular to the semi-major axis, the depolarization is stronger compared to fields parallel to it. In other words, the electric field along the semi-major axis is enhanced over the field perpendicular to it. The magnitude of this effect is described by the dielectric enhancement factor

$$R_e = \frac{|f_{LF}^{\parallel}|^2}{|f_{LF}^{\perp}|^2} = \left(\frac{\kappa_m + (\kappa_s - \kappa_m)\alpha^{\perp}}{\kappa_m + (\kappa_s - \kappa_m)\alpha^{\parallel}} \right)^2 . \tag{2.43}$$

According to Refs. [47, 105], for ellipsoids with $b \gg d$ the depolarization coefficients can be written as $\alpha^{\perp} = (1 - \alpha^{\parallel})/2$ and $\alpha^{\parallel} = d^2[\ln(2b/d) - 1]/b^2$.

Notably, it has been shown, that the dielectric enhancement effect increases the linear polarization of the PL of CdSe nanorods, since the transitions with dipole moments parallel to the c-axis are favored. [47] Furthermore, this effect can lead to a selective excitation of nanoparticles with c-axis parallel to the electric field of the incident light. This aspect will be addressed in more detail in chapter 5, where the dielectric enhancement effect and its impact on the PL polarization is discussed for the case of DiR NCs.

Chapter 3

Experimentals

In this chapter the experimental methods, which were used in this study, are described. A common tool for characterizing semiconductor nanostructures is PL spectroscopy. This technique involves the generation of eh-pairs by a laser source and the detection of the light, which is emitted in their recombination process. Structural and electronic properties lead to certain signatures in the emitted light, which can be identified by analyzing spectral- or polarization characteristics of the PL or by detecting the arrival of photons over time. Notably, for investigating exciton dynamics, time resolution of the PL is crucial. Since most of the results, which are discussed in this thesis, are related to exciton dynamics, in the following emphasis is given to time-resolved PL spectroscopy.

Typically, when spectral characteristics of the PL of NC ensembles are studied experimentally, the size and shape dispersion leads to an inhomogeneous broadening, which conceales signatures of - for instance - phonons or multiexcitons. A method to prevent this, is to excite a subensemble of the NCs resonantly, which leads to a narrowing of spectral lines. Thus, this technique is named fluorescence line narrowing (FLN).

In the beginning of this chapter time-resolved PL spectroscopy and notably the time-correlated single photon counting technique (TCSPC) is introduced. Afterwards the the time-resolved PL setup is presented. Following that, the FLN technique is described in more detail and the corresponding experimental configuration is shown. Finally, an overview over the studied samples and details on their synthesis are described.

3.1 Time-resolved photoluminescence spectroscopy

In time-resolved PL spectroscopy the time-evolution of the optical response of the material of interest is used to get insights into the microscopic carrier dynamics, which accompany the process of light emission. For this purpose the material is driven from its equilibrium state by a perturbation, which is a laser pulse in this case. In a semiconductor, which is excited by an incident light beam of sufficient energy, electrons are promoted from the valence to the conduction band. The excited electron and the hole, which is left in the valence band, may spontaneously recombine after some time. In this case the excess energy can be released in form of light, the PL, or in nonradiative processes, such as phonon emission or by transferring energy to other particles (Auger recombination), as described in section 2.3.2.

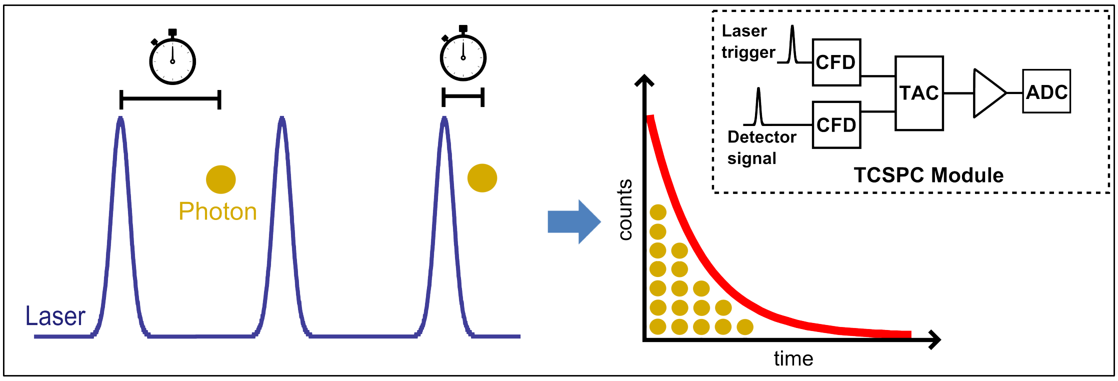

Figure 3-1: Illustration of the principle of a TCSPC measurement. The inset contains a sketch of the construction of a typical TCSPC module.

The goal of time-resolved PL spectroscopy is to elucidate the relevance and mechanisms of possible recombination pathways of an excited state by detecting the spontaneously emitted photons over time. Depending on the probability for the occurrence of radiative or nonradiative processes, the signal, which is measured in the experiment can strongly deviate from the monoexponential decay, which results from spontaneous recombination. The luminescence decay time τ measured in experiments then depends on the rates of all processes

$$\tau = \frac{1}{\Gamma_r + \Gamma_{nr}}, \tag{3.1}$$

where $\Gamma_r = 1/\tau_r$ and $\Gamma_{nr} = 1/\tau_{nr}$ are the radiative and nonradiative rates, respectively.[58] Furthermore, when ensembles of NCs are investigated or several excited states of a single NC are involved, due to fluctuations in radiative and nonradiative rates between different NCs and different states, the measured decay is typically multiexponential.

3.1.1 Time-correlated single photon counting

There are several methods for acquiring an optical waveform over time and these can be categorized in analogue recording and photon counting techniques. Photon counting offers a number of advantages over analogue techniques in terms of noise, time resolution, aquisition time etc. For a detailed discussion the reader is referred to Ref. [106].

Figure 3-1 illustrates the principle of a TCSPC measurement. The sample is excited by a train of laser pulses, whereupon it can emit a photon. The time between the excitation pulse and the photon, which is seen by a detector, is measured. This process is repeated many times and from the measured times between laser pulse and subsequent photon arrival a histogram is build up, whose envelope (shown as a red curve in Fig. 3-1) corresponds to the optical waveform. The TCSPC technique requires the probability for detecting a photon in each excitation period to be small, therefore it is suitable for high excitation repetition rate experiments with a low intensity response. The probability for detecting a photon in one excitation cycle must be less than one, since only a single photon can be detected per cycle.

Technically, TCSPC is realized as depicted in the inset of Fig. 3-1. The pulsed laser, which is used for excitation, as well as the detection electronics are triggered by a synchronisation source, i.e. the same pulse, which triggers the laser serves as a time reference.

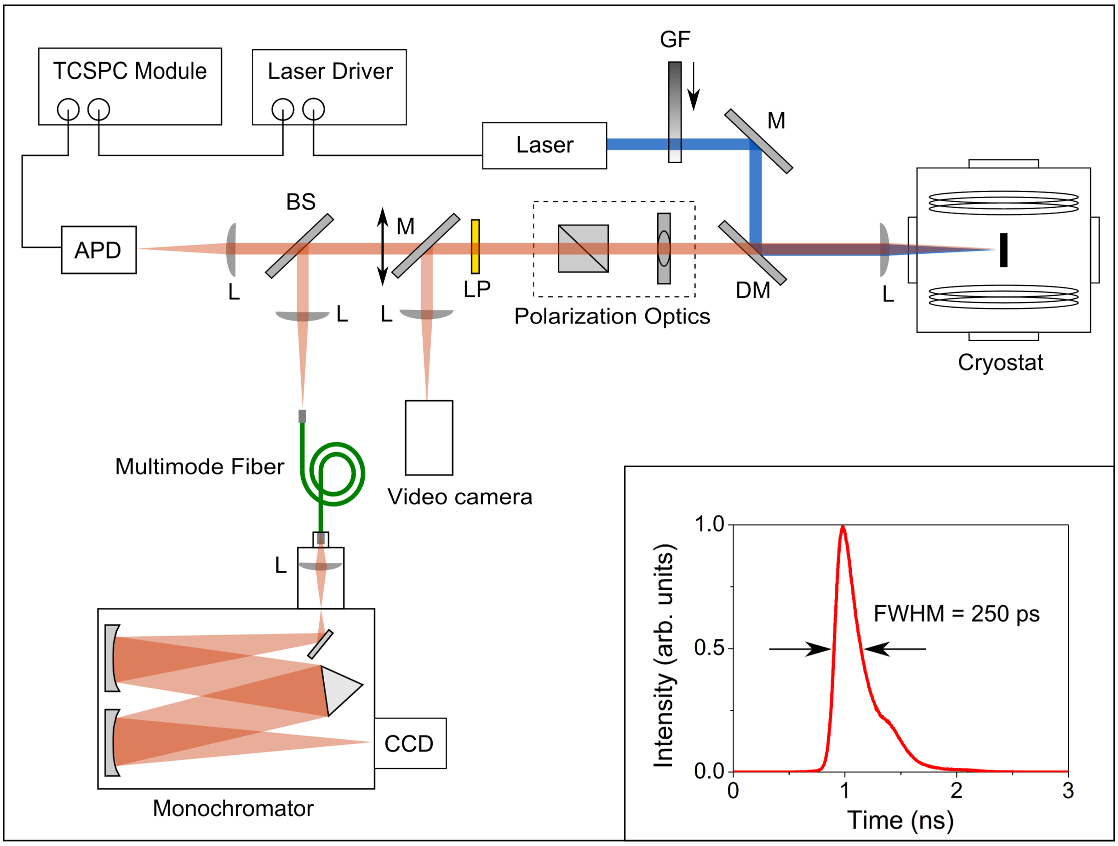

Figure 3-2: Sketch of the time-resolved magneto-photoluminescence setup. Abbreviations: APD - avalanche photodiode, L - lens, BS - beam splitter, M - mirror, DM - dirchoic mirror, GF - gray filter, LP - long pass filter, CCD - charge coupled device. The inset shows the instrumental response function of the system.

If in one excitation cycle a photon is seen by the detector, a voltage pulse is sent to the detection electronics. Both, signal and trigger pulse-trains are cleansed by constant fraction discriminators (CFD) to suppress noise. A time-to-amplitude converter (TAC) generates a voltage signal, whose amplitude is proportional to the time delay between the time reference pulse and the pulse induced by the photon. This voltage signal, after further amplification, is converted by an analog-to-digital converter (ADC) and depending on the amplitude is saved into a specific digital time channel.

3.1.2 Time-resolved magneto-photoluminescence setup

In Fig. 3-2 a sketch of the experimental setup, which was used for time-resolved PL measurements, is depicted. The sample of interest was cooled with liquid helium in an optical cryostat. Thereby, temperatures as low as $T = 2.2$ K could be achieved and by electrical heating the temperature could be increased up to 70 K. The cryostat offered direct optical access and incorporated a superconducting selenoid, which was capable of generating magnetic field strenghts up to 17 T. For excitation a pulsed semiconductor diode laser (I, see Table 3-1), emitting at 405 nm (= 3.06 eV) with repetition rates between 1 Hz and 5 MHz and a nominal pulse duration of 37 ps, was used. The laser power was adjusted with a variable gray filter (GF). The beam was directed along the optical axis by a dichroic mirror (DM) and focused onto the sample by a lens (L), which also served for collecting the emitted PL. In the detection path remaining scattered laser light was removed by a longpass filter (LP). For analyzing the polarization in experiments with an external magnetic field a combination of a quarter wave plate and a Glan-Thomson-prism (GTP, Polarization Optics in Fig. 3-2) was used. A video camera served for imaging the sample and laser beam adjustment. The signal was split by a beam splitter (BS) and was sent, either via a multimode fiber to a monochromator (IIa/b in Table 3-1) with a nitrogen-cooled charge-coupled device (CCD, IIIa/b in Table 3-1) for spectral resolution, or to the time-resolution detection electronics, which consisted of a single photon detector (APD, IV in Table 3-1) in combination with a TCSPC module (V in Table 3-1).

The time-resolution of the system is a crucial parameter, since it limits the capability for measuring the dynamics of the process of interest. Processes occuring on shorter timescales than the lower limit of temporal resolution of the setup cannot be resolved. The time-resolution can be estimated by measuring the instrumental response function, which is affected by the respective time-resolution of each component used in the setup. It was measured by directing scattered excitation light onto the detector. The result is depicted in the inset of Fig. 3-2. The curve has a full width at half maximum (FWHM) of approximately 250 ps, which corresponds the limit of temporal resolution of the setup.

The bottom part of the insert, which was used for mounting the sample into the cryostat, is depicted in Fig. 3-3. It contains the excitation/detection lens, the sample holder and a positioning system (VI in Table 3-1), allowing for precise positioning of the sample with sub-nm resolution. Typically, for NC ensemble measurements, a lens with a focal length $f = 50$ mm was used. For high resolution measurements, the lens was exchanged by either a microscope objective (numerical aperture: $NA = 0.8$, working distance: $WD = 0.4$ mm) or an aspheric lens ($f = 6$ mm).

Index	Device	Model	Specifications/Details
I	Pulsed laser	ALPHALAS PICOPOWER-LD-405	Wavelength/Energy: 405 nm/3.06 eV Repetition rate: 1 Hz - 5 MHz Nominal pulse duration: 37 ps
IIa	Monochromator 1	YOBIN IVON SPEX, TRIAX 550	Focal length: 550 mm Gratings used: 600 g/mm Slit width: 0.2 mm
IIb	Monochromator 2	PRINCETON INSTRUMENTS SP2500i	Focal length: 500 mm Gratings used: 150 g/mm Slit width: 0.2 mm
IIIa	CCD 1	HORIBA, SpectrumONE CCD-3500	Nitrogen cooled
IIIb	CCD 2	ROPER SCIENTIFIC SPEC-10:400	Nitrogen cooled
IV	APD	MPD-1CTC	Time resolution: < 50 ps
V	TCSPC module	PICOQUANT PICOHARP300	Histogram time bins: 65536 Minimum width per bin: 4 ps
VI	Positioning system	ATTOCUBE ANP(x,y,z)101	Pecision: < 1 nm

Table 3-1: Devices belonging to the time-resolved magneto-photoluminescence setup.

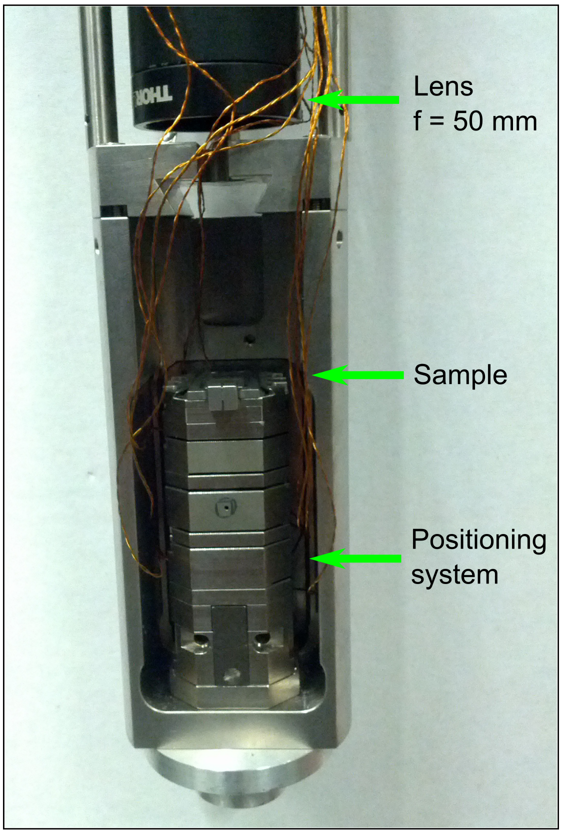

Figure 3-3: Photograph of the sample holder and the positioning system.

3.2 Fluorescence line narrowing

When an ensemble of NCs is excited non-resonantly, (the laser energy is larger than the energy of the first absorption peak) the PL spectrum has a gaussian shape and is inhomogeneously broadened, due to the shape and size dispersion within the ensemble, typically to several tenth of meV. This makes it impossible to resolve signatures of the exciton fine-structure, phonons or multiexcitons. In fluorescence line narrowing experiments the laser energy is tuned to be in resonance with only a small fraction of NCs. This leads to selective excitation of these NCs and considerably narrower lines in PL spectra. [48]

In Fig. 3-4 typical PL spectra of a CdSe NC ensemble, obtained with non-resonant and resonant excitation at a temperature $T = 4.2$ K, are shown. The black curve is a spectrum obtained by non-resonant excitation at $\lambda_{\text{laser}} = 405$ nm (3.06 eV). It has a gaussian shape and a FWHM of approximately 100 meV. If the sample is excited at a wavelength of $\lambda_{\text{laser}} = 532.177$ nm (2.33 eV, the laser line is indicated as a green line) several narrow peaks can be observed in the FLN spectrum, which is shown as a red curve. The first peak on the low energy side of the laser corresponds to the zero phonon line (ZPL). Further, in the low energy regime several phonon replicas can be observed, each shifted by multiples of the bulk LO-phonon energy of 25 meV. [48]

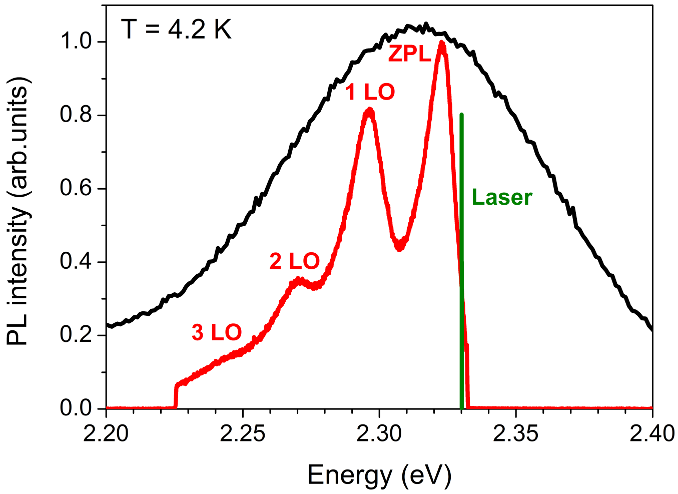

Figure 3-4: Comparison of PL spectra of bare CdSe NCs obtained by non-resonant excitation at an energy 3.06 eV (black curve) and resonant excitation at an energy 2.33 eV (red curve) at $T = 4.2$ K. The laser line for the case of resonant exciation is shown as a green line.

3.2.1 Fluorescence line narrowing setup

The setup, which was used for FLN, is depicted in Fig. 3-5. The sample was mounted in an optical cryostat and was cooled with liquid helium. The temperature was varied between 1.6 K and 40 K. For excitation, a continuous wave (CW) diode-pumped solid-state laser (I, See Table 3-2) operated at a wavelength of 532.177 nm was used. The excitation power was varied with a gray filter. In order to suppress laser stray light in the signal a cross-polarized excitation/detection scheme was used. The laser was linearly polarized by a GTP and was then focused onto the sample. In the detection path another GTP, rotated by 90° with respect to the GTP in the excitation path, removed laser stray light from the signal. A video camera was used for imaging of the sample and for laser beam adjustment. For spectral resolution the PL was sent through a triple spectrometer (II in Table 3-2) and was imaged by a nitrogen cooled CCD (III in Table 3-2). The triple spectrometer consists of three single monochromator stages (S1, S2 and S3) and it can be used in either additive or subtractive mode. The subtractive mode was used, because it allows for good stray light rejection. It is illustrated in Fig. 3-6. In this configuration the first two stages (S1 and S2) are used as a tunable bandpass filter. S1 disperses the signal and images the spectrum onto the output slit. By adjustiing the slit width the spectral range of interest can be selected. In stage S2 the resulting signal is focused onto the output slit, thereby unwanted stray light is rejected. The stage S3 is used for dispersion of the signal and it projects the spectrum onto the CCD.

3.3 Samples

The nanoparticles, which were studied in this thesis, were fabricated by Raquel Gomes and Tangi Aubert in the department Physics and Chemistry of Nanostructures of Ghent University in 9000 Ghent, Belgium. An overview is given in Table 3-3. The spherical core is made of CdSe and, in case of the core/shell type, is capped by a CdS shell of either spherical shape or rod shape (dot-in-rod). The core sizes were determined by UV-Vis

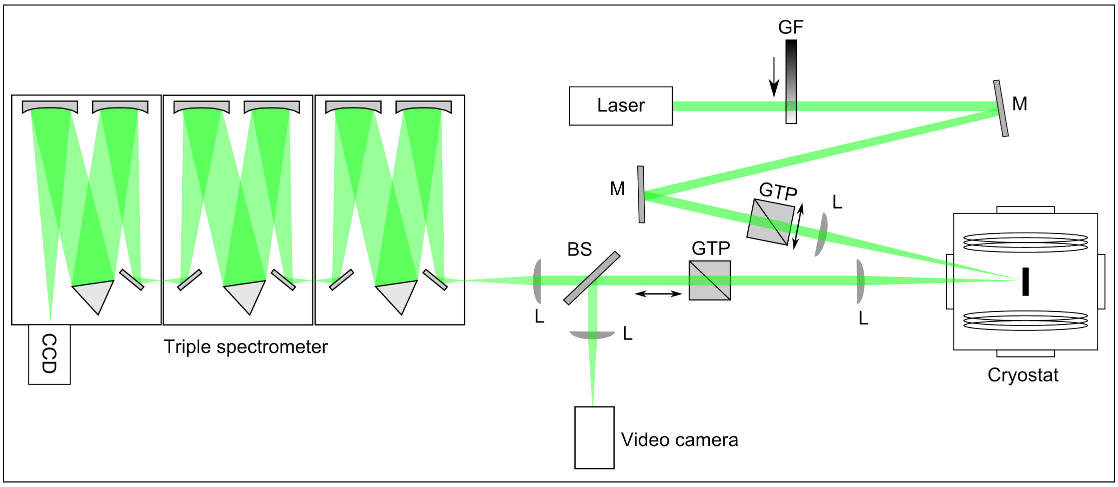

Figure 3-5: Sketch of the fluorescence line narrowing setup. Abbreviations: GF - gray filter, BS - beam splitter, M - mirror, L - lens, GTP - Glan-Thompson prism, CCD - charge-coupled device.

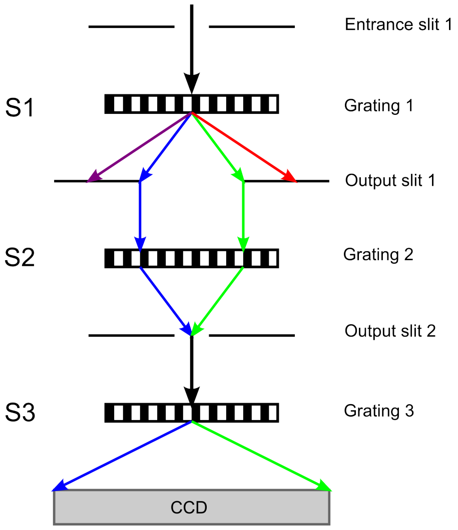

Figure 3-6: Illustration of a triple spectrometer operated in subtractive mode. The arrows indicate the light path.

spectrometry from the first absorption peak energy and by using a sizing curve published in Ref. [107]. The length, width or thickness of the shell was determined by TEM image inspection. Typical TEM images of DiRs and spherical core/shell NCs are shown in Figs. 3-7 (a) and (b). Typically, in DiR NCs the core is centered at around 1/3 of the rod length, as indicated in the sketch of the DiR geometry in Fig. 3-7. The hexagonal c-axis is parallel to the long axis of the rod. [108] To obtain the sizes listed in Table 3-3 several particles were measured in TEM images and a fit of the resulting histograms by a gaussian distribution function yielded the average particle size.

The DiRs were fabricated by the seeded growth approach, as described in Ref. [108]. In this method, ready-made bare CdSe NCs are used as a seed for the growth of the anisotropic CdS shell. In the beginning CdO is decomposed in the presence of phosphonic

Index	Device	Model	Specifications/Details
I	CW laser	LIGHTHOUSE PHOTONICS SPROUT-G	Wavelength/Energy: 532.177 nm Max. average output power: > 10 W Output power used : < 0.2 W
II	Triple spectrometer	PRINCETON INSTRUMENTS TRIVISTA 555	Operated in subtractive mode Focal length: 500 mm Gratings (S1/S2/S3): 900/900/900, in g/mm
III	CCD	PRINCETON INSTRUMENTS SPEC-10:2K/LN	Nitrogen cooled

Table 3-2: Devices belonging to the fluorescence line narrowing setup.

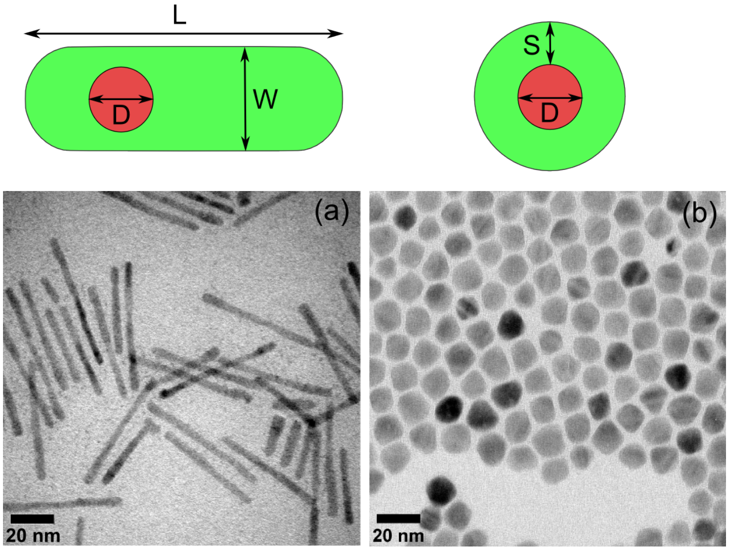

Figure 3-7: Transmission electron microscope (TEM) images of (a) DiRs (sample #4) and (b) spherical core/shell NCs (sample #R5). The NC geometry is illustrated by the sketches above.

acids and the mixture is heated up to $350 - 380°$C. A separate solution containing sulfur dissolved in trioctylphosphine as well as CdSe NCs, which have been previously prepared, is quickly injected into the heated flask. After the injection the CdS binds preferentially to the CdSe cores instead of forming seperate nulcei, since the activation energy for attaching to CdSe is lower. The growth is further controlled by the duration, in which the heating is kept running. The morphology of the NCs can be controlled by adjusting the seed diameter, the growth temperature and the amount of precursors and seeds which are injected.

The spherical core/shell NCs have been synthesized using the so-called ”flash” synthesis, as reported in Ref. [109]. Similar to the DiR synthesis, this method utilizes a seeded growth approach. Instead of using phosphonic acids, however, in this method carboxylic acid is used, which promotes isotropic growth of CdS on the CdSe seed.

For experimental investigation a droplet of 1 μL NCs, which were dissolved in toluene (the concentration was a few μM), was transferred on a 6×6 mm or 3×3 mm glass-slide and afterwards dried.

DiR NCs

#	Core diameter D (nm)	Shell length L (nm)	Shell width W (nm)	Material Core/Shell
1	2.5	28.9(1.5)	5.3(0.5)	CdSe/CdS
1a	2.5	20(1)	4.5(0.5)	CdSe/CdS
2	2.5	22(2)	3.8(0.3)	CdSe/CdS
3	2.5	22.8(1.8)	3.4(0.2)	CdSe/CdS
3a	2.5	62(2)	3.1(0.2)	CdSe/CdS
4	3.2	60(5)	4.1(2)	CdSe/CdS
4a	3.2	41(2)	4.1(0.2)	CdSe/CdS
5	3.2	32(1)	4.1(0.3)	CdSe/CdS
6	3.7	20.4(1.3)	6(0.6)	CdSe/CdS
7	3.7	26.5(2.7)	5(0.3)	CdSe/CdS

Spherical NCs

#	Core diameter D (nm)	Shell thickness S (nm)	Material Core/Shell
R1	3.1	2	CdSe/CdS
R2	2.7	0	CdSe/no
R3	2.7	0.8	CdSe/CdS
R4	2.7	3.7	CdSe/CdS
R5	2.7	5.3	CdSe/CdS

Table 3-3: Parameters of studied samples. Shell length, shell width and shell thickness were deduced from TEM images. Numbers in brackets denote standard deviations. The core size was derived from the first absorption peak energy in combination with the sizing curve reported in Ref. [107].

Chapter 4

Exciton fine structure and recombination dynamics in CdSe/CdS nanocrystals - Role of the shell shape

In this chapter the effect of the shell shape of CdSe/CdS NCs on the exciton fine structure and exciton dynamics is studied at low temperatures. As discussed in section 2.2.3 some of the fine structure states are optically forbidden in the electric-dipole approximation. Depending on the ordering of the fine structure states, especially at low temperatures, at which only the lowest fine structure states are thermally populated, the type of the exciton ground state (spin singlet or triplet) determines the optical response of the NC. The energy splitting between spin singlet and triplet states depends on the eh-exchange interaction, which is strongly enhanced in NCs compared to bulk material. The exchange strength constant η is inversely proportional to the cubic NC radius in spherical NCs. [28] The experimental results, which are presented in this chapter, indicate, that the eh-wavefunction overlap can be tuned by changing the size and shape of the CdS shell, due to a significant leakage of the electron wavefunction into the shell material. This affects the exciton fine structure as well as exciton recombination dynamics.

The chapter is structured as follows: In the upcoming section findings of preceding experimental and theoretical studies relevant to this topic are discussed. Later on, the experimental approach is described and the results are presented and interpreted. Finally, a summary of the findings is given.

Some of the experimental findings, which are discussed in this chapter, have been previously published in Ref. [110] and some have been presented in a Master's thesis, [111] which was supervised by the author.

4.1 Introduction

The growth of a shell with material having a larger band gap ($E_g \approx 2.5$ eV for CdS at helium temperature) than the core material ($E_g \approx 1.75$ eV for CdSe at helium temperature) leads to the formation of a potential well in the core region. A scheme of the band alignment for this configuration is depicted in Fig. 4-1 (a). The potential well constituted by the core affects the spatial spread of the carrier wavefunctions due to confinement. Depending on the difference in valence band and conduction band alignment between the shell and the core material, the degree of confinement can be different for the electron and the hole, leading to an effective spatial separation of the carriers. This affects the strength of their interaction.

The magnitudes of the conduction and valence band offsets are not well known, although they were subject to several theoretical [112] and experimental studies. [66,112–115] While for the valence band the consens is a positive band offset with values between $\Delta E_v \approx 0.3$ eV and 0.78 eV, [66,112–114] corresponding to a type-I band alignment, the situation for the conduction band is less clear. The suggested values for the conduction band offset vary between $\Delta E_c = -0.3$ eV and 0.32 eV. [66, 113–115] Negative offset values in the conduction band correspond to a quasi type-II band alignment, for which the electron is preferentially localized in the shell region.

Figure 4-1 (b) shows the calculated spatial probability distribution $P(r) \propto r^2|\psi_{e,h}(r)|^2$ as a function of the distance from the core center for the electron and the hole, assuming a conduction band offset of $\Delta E_c = 0.32$ eV and a valence band offset $\Delta E_v = 0.42$ eV [as shown in Fig. 4-1 (a)] for various shell thicknesses around the CdSe core. Here, $\Psi_e(r)$ and $\Psi_h(r)$ are the electron and hole envelope wavefunctions. These calculations are based on the single band effective mass approximation (EMA) approach, as described in section 2.2.2 as well as in Refs. [8, 36, 65, 66]. The effective masses of electron (e) and hole (h) were taken to be $m_c^e = 0.13m_0$, $m_s^e = 0.21m_0$, $m_c^h = 0.45m_0$ and $m_s^h = 0.68m_0$, where m_0 is the free electron mass and the indices c, s denote the core and the shell, respectively. [36, 65, 66] The calculations indicate, that the hole is predominantly confined in the core region, whereas the electron wavefunction significantly leaks into the shell, due to the smaller height of the potential barrier in the conduction band formed by the core/shell interface and because of its lower effective mass. With increasing shell thickness, the electron gets further delocalized over the shell, obvious from the spread of the electron spatial probability distribution into this region [compare the green, red and orange shaded areas in Fig. 4-1 (b)]. In contrast the hole wavefunction (grey shaded area) remains almost unaffected and as a result the eh-wavefunction overlap decreases with increasing shell thickness.

The spatial separation of the eh-pair has important consequences for the exciton recombination dynamics and for the exciton fine structure. On the one hand the radiative decay rate of the bright exciton, within the EMA, is proportional to the overlap integral $\Theta_{e-h} = |\int d^3r \Psi_e(r)\Psi_h(r)|^2$. [26, 28] An increase in electron and hole wavefunction overlap leads to an increase of the probability for radiative recombination. On the other hand, the energy splitting ΔE_{bd} between bright (singlet) and dark (triplet) exciton states depends on the short-range exchange interaction, which is related to the envelope wavefunctions by $\xi_{e-h} = \int d^3r |\Psi_e(r)|^2 |\Psi_h(r)|^2$. [7, 28] In Ref. [66] Brovelli et al. report, that changes in shell thickness lead to an proportional change in both quantities and infer a linear dependence between the bright-dark energy splitting and the overlap integral $\Delta E_{bd} = \Delta_0 \Theta_{e-h}$, where Δ_0 is the exchange interaction splitting when the e-h overlap is unity. The effect of a change in shell thickness on the PL decay strongly depends on the temperature. At high temperatures, where $k_B T \gg \Delta E_{bd}$, the exciton radiative recom-

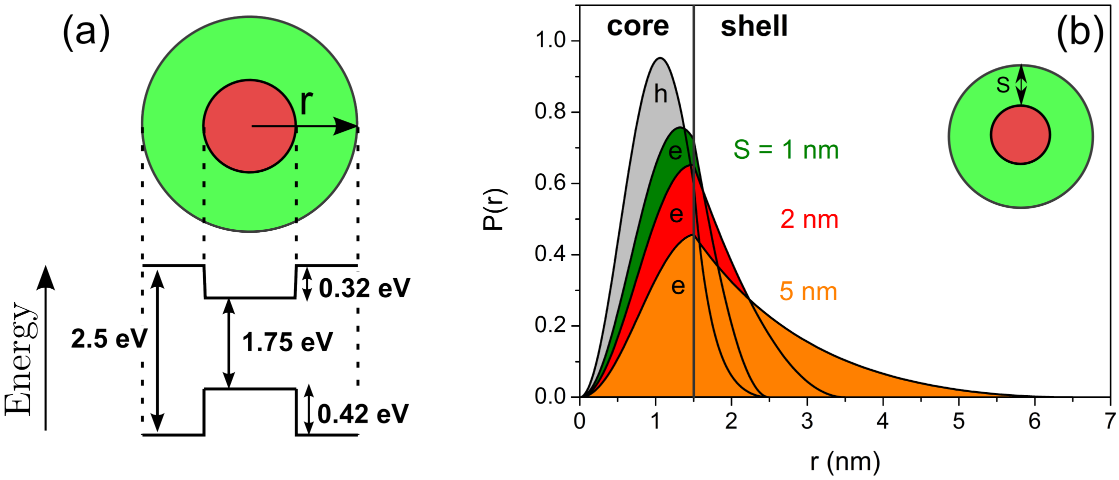

Figure 4-1: (a) Band alignment diagram of a spherical CdSe/CdS core/shell NC. (b) Spatial probability distribution of hole (h) and electron (e) for a NC with a core size of 3 nm and varying shell thickness S. The calculation is based on the EMA approach similar to Ref. [66].

bination rate is expected to decrease with increasing shell thickness, due to the reduced overlap integral Θ_{e-h}. On the contrary, at low temperatures the thermal population of the bright and the dark exciton state, which is dependent on the bright-dark splitting, becomes relevant. In this regime, an increasing shell thickness leads to a decrease of the exchange splitting and thereby to an increase of the radiative rate due to thermal population of the optical bright state.

Theoretical and experimental investigations regarding the influence of the shell on the exciton fine structure, especially on the bright-dark energy splitting, up to now have been restricted to core/shell NCs with spherical symmetry. [28, 66, 116, 117] Studies on more complex heteronanostructures, such as DiR NCs, which combine a spherical core with a rod-shaped shell, are rare. These structures are interesting, since they allow to exploit the possibilities to control carrier interactions further, and thereby the optical properties of the NC, by means of tayloring the confinement of individual carriers. In DiR an electron, which leaks into the shell faces a reduced confinement in the rod axis direction. As a result an asymmetric spread of the electron wavefunction is expected. This aspect has been adressed theoretically and in numerous experiments employing very different techniques. For example, studies utilizing time-resolved PL and transient absorption measurements report on enhanced electron delocalization into the shell, preferentially in the rod axis direction, at elevated temperatures. Due to a decreasing eh-wavefunction overlap the radiative decay rate decreased with increasing shell aspect ratio, i.e. the ratio of shell length and width, or shell volume and the effect seemed to be independent of the core size. [113, 115, 118]

However, none of the aforementioned studies explicitly considers the consequences of electron delocalization into shells with anisotropic shape for the exciton fine structure and for exciton relaxation and recombination dynamics at low temperatures. This study aims to to fill this gap and clarifies, how the shell shape affects the exciton fine structure, notably the bright-dark energy splitting, which determines exciton relaxation processes and thereby the optical properties of DiR nanostructures at low temperatures.

Apart from revealing the magnitude of the bright-dark energy splitting for various

DiR nanostructures and deriving a dependence between the splitting and the shell dimensions, the impact of the shell shape on bright and dark exciton recombination rates is discussed. The physical origin of dark exciton radiative recombination is a long standing puzzle, which is unresolved yet. In the electric dipole approximation momentum conversation requirements inhibit the radiative transition from the dark exciton ground state with angular momentum $|F| = 2$ to the vacuum state, since the absolute value of the photon angular momentum is 1. [28] While momentum conversation could be satisfied by a LO phonon assisted transistion, where an emitted phonon carries part of the angular momentum projection, FLN experiments clearly evidenced the excistence of a weakly allowed ZPL, whose intensity increases with increasing magnetic field. [28,48,119] This observation suggests the existence of an alternate mechanism. It is well established, that an external magnetic field, if oriented perpendicular to the hexagonal axis of wurtzite type NCs, can mix the optical forbidden exciton states with optical allowed states. [28, 43, 103, 120] This mixing gives oscillator strength to the previous forbidden transitions, leading to a shortening of the PL decay with increasing magnetic field and an increase of the intensity of the ZPL in FLN experiments. This aspect led to the hypothesis, that mixing of dark and bright exciton states by internal magnetic fields may give rise to the observed ZPL. Several origins have been proposed to be capable of mixing dark with optical allowed states, for example paramagnetic defects, [28] surface ligands [121] or dangling bonds. [122] However, no experiments were able to clarify the exact origin of dark exciton recombination. As will be discussed, the experimental results presented here support a surface assisted mechanism. Besides revealing a strong correlation between bright-dark energy splitting and the dark exciton radiative rate the results indicate a strong dependence of the dark exciton lifetime on the shell shape.

4.2 Experimental approach

The experimental approach for investigating the exciton fine structure was used in several studies on spherical core/shell NCs [66, 116, 117, 123, 124] and is based on the assumption, that at low temperatures, due to the low thermal energy of the excitons, the exciton fine structure can be approximated by a three level system, as depicted in Fig. 4-2 (a). It consists of the exciton ground state $|G\rangle$, the lowest excited state $|F\rangle$, which is optically forbidden (the forbidden transition is indicated by the red dashed arrow), and a higher lying optically allowed state $|A\rangle$ (the allowed transition is indicated by the red solid arrow). The states $|A\rangle$ and $|F\rangle$ are split by the bright-dark energy ΔE_{bd}. The model assumes, that there is radiative recombination from these states with rates Γ_A and Γ_F respectively. The luminescence intensity in this case can be written as $I(t) = \eta_A \Gamma_A p_A + \eta_F \Gamma_F p_F$, where $\eta_{A,F}$ are the corresponding quantum efficiencies and $p_{A,F}$ the occupation numbers of the respective levels. Furthermore, the model includes thermal coupling between the excited states. In this regard γ_0 describes the spin relaxation from $|A\rangle$ to $|F\rangle$ at $T = 0$ K and $\gamma_0 N_B = \gamma_{th}$ the coupling between these states due to phonons. Here $N_B = 1/(\exp(\Delta E_{bd}/k_B T) - 1)$ is the phonon occupation according to the Bose-Einstein statistic.

After excitation by a laser pulse, the following rate equations describe the dynamics

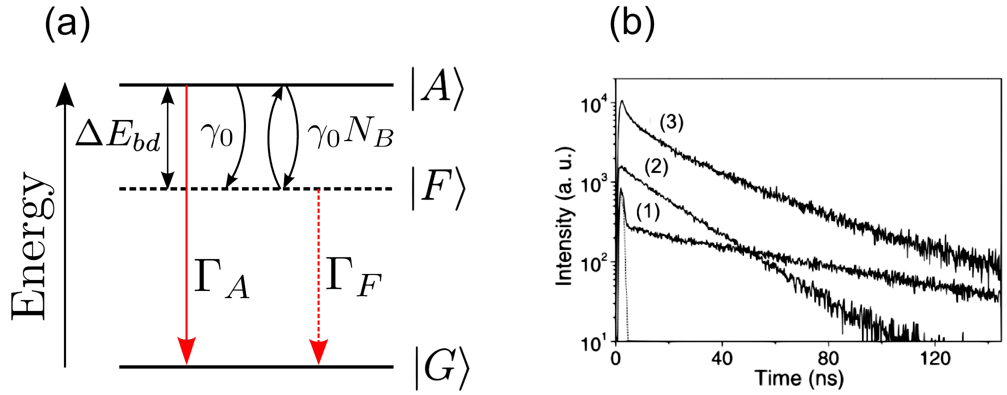

Figure 4-2: (a) Simplified model of the energy level scheme of the lowest exciton fine structure states. The red arrows denote optically allowed (red solid arrow) and optically forbidden (red dashed arrow) transitions. (b) Typical luminescence decays for (1) a single NC at low temperature, (2) a single NC at high temperature and (3) an ensemble of NCs at low temperature. Adapted from Ref. [116].

in this system:

$$\begin{aligned}\frac{dp_A}{dt} &= -p_A[\Gamma_A + \gamma_0(1+N_B)] + p_F\gamma_0 N_B \\ \frac{dp_F}{dt} &= -p_F(\Gamma_F + \gamma_0 N_B) + p_A\gamma_0(1+N_B).\end{aligned} \tag{4.1}$$

With the assumption $\gamma_0 \gg \Gamma_A \gg \Gamma_F$ the luminescence intensity as a function of time can be written as

$$I(t) = \frac{\eta_A\Gamma_A N_B + \eta_F\Gamma_F}{1+2N_B}\exp\left(-\frac{t}{\tau_{\mathrm{long}}}\right) + \eta_A\Gamma_A\left(p_A(0) - \frac{N_B}{1+2N_B}\right)\exp\left(-\frac{t}{\tau_{\mathrm{short}}}\right). \tag{4.2}$$

Here, $p_A(0)$ denotes the initial occupation of state $|A\rangle$ after the exciting laser pulse. The time evolution of the intensity has the form of a biexponential decay, where the two components have the characteristic rates

$$\begin{aligned}\tau_{\mathrm{short}}^{-1} &= \gamma_0(1+2N_B) \\ \tau_{\mathrm{long}}^{-1} &= \frac{\Gamma_A+\Gamma_F}{2} - \left(\frac{\Gamma_A-\Gamma_F}{2}\right)\tanh\left(\frac{\Delta E_{bd}}{2k_BT}\right).\end{aligned} \tag{4.3}$$

The short component corresponds to the relaxation rate from the upper to the lower state, at low temperatures it is $\tau_{\mathrm{short}}^{-1} \approx \gamma_0$. Thus, τ_{short} is a measure for how long it takes the system to achieve thermal equilibrium. At long times photons stem from radiative recombination of excitons from the lower state $|F\rangle$ and thermally excited excitons from the upper state $|A\rangle$. At high temperatures, at which the upper and the lower state are equally populated, the short component vanishes for $p_A(0) = p_F(0) = 1/2$ and the decay occurs with a rate $1/\tau_{\mathrm{long}} = (\Gamma_A + \Gamma_F)/2$. At low temperatures the rate $1/\tau_{\mathrm{long}}$ corresponds to the dark exciton radiative rate $1/\tau_{\mathrm{long}} = \Gamma_F$.

Typical luminescence decays observed for spherical CdSe/ZnS NCs are shown in Fig. 4-2 (b). The decay of a single NC [curve (1)] at low temperatures is biexponential as described by Eq.(4.2). As the temperature is increased the amplitude of the short

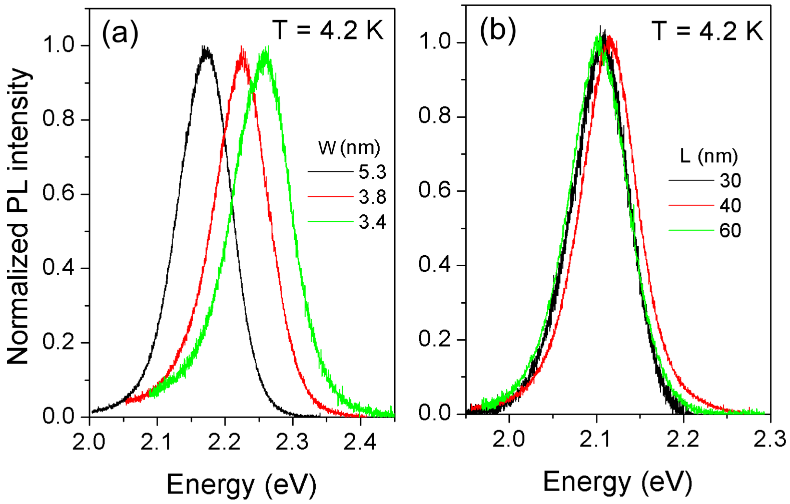

Figure 4-3: Dependence of the normalized PL spectra on (a) rod width W (samples #1,#2,#3 in Table 3-3) and (b) rod length L (samples #4,#4a,#5 in Table 3-3) for a fixed core size of $D = 2.5$ nm in (a) and $D = 3.2$ nm in (b).

component vanishes and a shortening of the long component is observed, leading to a monoexponential decay at elevated temperatures, as shown by curve (2) in Fig. 4.2 (b). An ensemble of NCs exhibits a multiexponential decay, although the signatures of the biexponential behaviour are still visible, as can be seen from curve (3) in Fig. 4.2 (b). [116]

From Eqs.(4.2) and (4.3) it is clear, that by measuring the luminescence decay over time as a function of temperature, exciton fine structure parameters, such as the bright-dark energy splitting ΔE_{bd} and the radiative recombination rates $\Gamma_{A,F}$ can be extracted from the experimental data. This technique was used to determine these quantities for DiR nanostructures and to clarify their dependence on shell shape and core size. The results are described in the following section.

In this experiment all DiR NCs listed in Table 3-3 have been studied, therefore three different core sizes with various shell geometries have been available. In order to prevent any multiexcitonic effects, the samples were excited with low average excitation power (< 0.02 W/cm^2) and with a repetition rate of either 500 kHz or 1 MHz, allowing for complete decay of the PL before reexcitation.

4.3 Experimental results and discussion

Time-integrated PL spectroscopy

A first clue about the spatial extension of the exciton wavefunction can be obtained by analyzing exciton PL spectra and their dependence on the geometry of the NC. Characteristic spectra, obtained at $T = 4.2$ K, are shown in Fig. 4-3 (a) for DiRs having a similar core size and rod length but a varying rod width (samples #1-#3), and in Fig. 4-3 (b) for DiRs with similar core size and rod width but with a varying rod length (samples #4,#4a and #5). It is obvious from these figures, that an increase in rod width from 3.4 nm to 5.3 nm leads to a shift of the PL maximum to lower energies by approximately

0.1 eV, whereas a change in rod length from 30 nm to 60 nm leaves the PL maximum position almost unchanged. These observations suggest that the exciton is confined in the plane perpendicular to the rod axis, consequently an increase in rod width leads to lower quantization energies. In contrast, no confinement seems to be present parallel to the rod axis and a change in rod length does not alter the kinetic energy of the carriers.

As a first approximation the transition energies for a core/shell system can be calculated with the single band EMA approach, [8,36,65,66] as described in section 2.2.2.

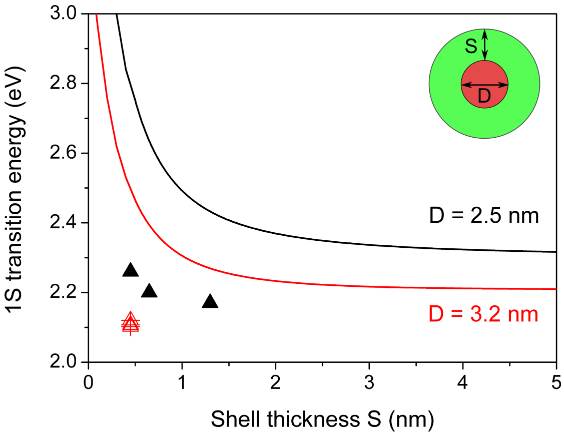

Figure 4-4: Model of the 1S transition energy for a spherical core/shell NC with core sizes $D = 2.5$ nm and $D = 3.2$ nm, calculated with the EMA approach. The black and red triangles correspond to the maximum peak energies derived from the spectra shown in Figs. 4-3 (a) and (b). The inset illustrates the geometry considered for the calculation.

The 1S transition energies can be derived from the condition, that the wavefunction vanishes at the shell boundary and for a core/shell NC they can be calculated according to Eq.(2.16). Figure 4-4 shows the calculated 1S transition energy for a spherical core/shell NC with core diameters 2.5 nm and 3.2 nm as a function of shell thickness, assuming similar values for the effective masses, conduction and valence band offsets and bandgap energies as they are given in Refs. [36,65,66]. From the calculated curves it is obvious, that the 1S transition energy depends on the core size as well as on the shell thickness. On the one hand, a change in core size by 0.7 nm leads to a decrease of roughly 0.15 eV in the transition energy. On the other hand, as the shell thickness is increased from 0.5 nm to 5 nm the transition energy is reduced by approximately 0.6 eV. This change in energy results from the varying degree of confinement for the electron and the hole with varying core size or shell thickness. While a change in core size strongly affects the confinement of both carriers, a change in shell thickness influences predominantly the confinement of the electron, due to its higher probability to leak into the shell as a result of the smaller conduction band offset and its lower effective mass, which was assumed for this calculation. This explains the comparatively large change in energy with increasing core size. From the curves it is also obvious, that the energy is sensitive to changes in shell thickness only up to a few nm. This results from the finite leakage of the electron wavefunction into the shell material. At small shell thicknesses, the electron still "feels" the boundaries of the NC, while at larger shell thicknesses the electron is not confined by the NC boundaries anymore. Naturally, the upper boundary of the sensitive regime is where the overall size of the NC is equal to the bulk exciton Bohr radius, which is $a_{ex} = 5.6$ nm in CdSe. [26] It is expected, however, that due to the additional confinement potential constituted by the core, the sensitive regime regarding the shell thickness is smaller, in accordance with the calculated curves in Fig. 4-4.

The maximum peak energies derived from the DiR spectra in Figs. 4-3 (a) and (b) are also shown in Fig. 4-4 as black and red triangles, respectively. Apparently, the data points deduced from the spectra deviate considerably from the calculated curves, although the essential trend seems to be consistent. The deviations could have the following reasons. Firstly, it is expected, that due to the lack of confinement along the rod axis, the quantum size effect for the electron is weaker compared to the spherical configuration, where the electron confinement is present in all three spatial dimensions. This reduces the confinement energy and could result in the observed redshift of the experimental data with respect to the calculated curves. Secondly, the core size of the NCs investigated in this thesis was determined by comparing the 1st absorption peak energy to a sizing curve given in Ref. [107]. This curve was received by measuring the size of several bare core NCs in TEM images. However, due to the low contrast between the NC and the carbon grid, especially the determination of the core size by TEM observation is imprecise and strongly depends on individual measurement techniques. It is therefore possible, that the core sizes of the samples investigated here are underestimated.

Finally, it has to be noted that the EMA approach can give only a qualitative understanding of transition energies and the spatial distribution of the carrier wavefunctions, since it utilizes a couple of simplifications, such as the assumption of single parabolic energy bands for the electron and the hole. It neglects the complex valence band structure, which is typically found for real semiconductor NCs, as well as effects such as valence subband-mixing or the eh-Coulomb interaction. [125] Nevertheless, the EMA calculations can help to understand the essential trends, which could be observed in the spectra shown in Figs. 4-3 (a) and (b).

The inhomogeneous broadening in ensemble PL spectra, which arises from the NC size dispersion, does not allow for identification of fine structure states involved in the radiative recombination process. Therefore, this technique is not suitable to go beyond the preceding considerations. As was discussed in the previous section time-resolved PL spectroscopy can give insights into the composition of the exciton fine structure and exciton recombination dynamics. In the following the results of time-resolved PL spectroscopy are discussed.

Time-resolved PL spectroscopy

Figure 4-5 shows the typical evolution of the PL decay (i.e. the PL intensity over time) for DiRs as the temperature is increased from $T = 2.2$ K to 60 K. At low temperatures the decay exhibits a clear biexponential shape. The short component has a lifetime of a few ns, whereas the lifetime of the long component is on the order of hundreds of ns. As the temperature is increased, the weight of the short component decreases and simultaneously the lifetime of the long component is reduced. At $T = 60$ K the decay is almost monoexponential. As discussed in section 4.2, this behavior is characteristic for exciton recombination within a system, which consists of a bright state and a dark exciton ground state with very different radiative rates [Fig. 4-2 (a)].

In Fig. 4-6 (a) the PL decays of DiRs (samples #1,#1a,#2,#3 in Table 3-3), which exhibit similar core sizes and comparable lengths of the CdS shell, are shown for $T =$

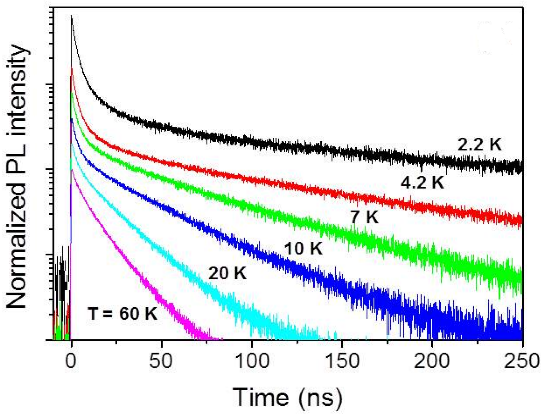

Figure 4-5: Temperature dependence of the PL decay for sample #1 (DiR, $D = 2.5$ nm, $W = 5.3$ nm, $L = 28.9$ nm). Offsets were added to succeeding curves for clarity.

4.2 K. With increasing rod width, the long component of the biexponential decay is shortened and the weight of the short component is reduced. This aspect is highlighted in the inset of Fig. 4-6 (a). The shortening of the long component indicates a change of exciton fine structure parameters, since at a given temperature according to Eq.(4.3) the long component is affected only by the dark and bright radiative rates and the bright-dark energy splitting. In contrast, as can be observed from Fig. 4-6 (b) a change in rod length does not alter the PL decay dynamics significantly (these DiRs correspond to samples #4,#4a,#5 in Table 3-3). This observation substantiates the assumption of a localization of the electron and the hole in the vicinity of the core. Therefore changes in rod length do not influence the eh-wavefunction overlap, which, as discussed in the beginning of this chapter, determines recombination dynamics and the bright-dark energy splitting, due to the eh-exchange interaction. In contrast, as is obvious from Fig. 4-6 (a), by altering the rod width, the recombination dynamics and the fine structure splitting can be modified.

In order to quantify the impact of the rod width in this regard, the temperature dependence of the PL decay is analyzed for DiRs with varying shell shapes and core sizes. As discussed in section 4.2, the bright-dark energy splitting and the bright and dark recombination rates can be determined from the evolution of the long component with temperature [Eq.(4.3)]. To this end, the long component of the PL decay at a given temperature was fitted with a monoexponential decay of the form $I(t) = I_0 \exp(-t/\tau_{\text{long}})$, where I_0 denotes the initial intensity and τ_{long} the characteristic lifetime of the long component. Figures 4-6 (c,d) summarize the evolution of $\Gamma_L = 1/\tau_{\text{long}}$ with increasing temperature for samples #1,#1a,#2,#3 in (c) and samples #4,#4a,#5 in (d). In order to determine the fine structure parameters the data points were fitted by Eq.(4.3). The resulting curves are shown as blue solid lines in Figs. 4-6 (c,d). The insets show the resulting bright-dark energy splitting ΔE_{bd} as a function of rod width in (c) and as a function of rod length in (d). As the rod width is increased from 3.4 nm to 5.3 nm, ΔE_{bd} decreases by approximately 2 meV. A change in rod lengths does not change the energy splitting significantly. The decrease of ΔE_{bd} with increasing rod width is a result of the decreasing eh-wavefunction overlap with increasing shell thickness, due to progressive electron leakage into the shell. As shown by Brovelli et al., a change in wavefunction overlap leads to a proportional change in the energy splitting ΔE_{bd}, as a result of the

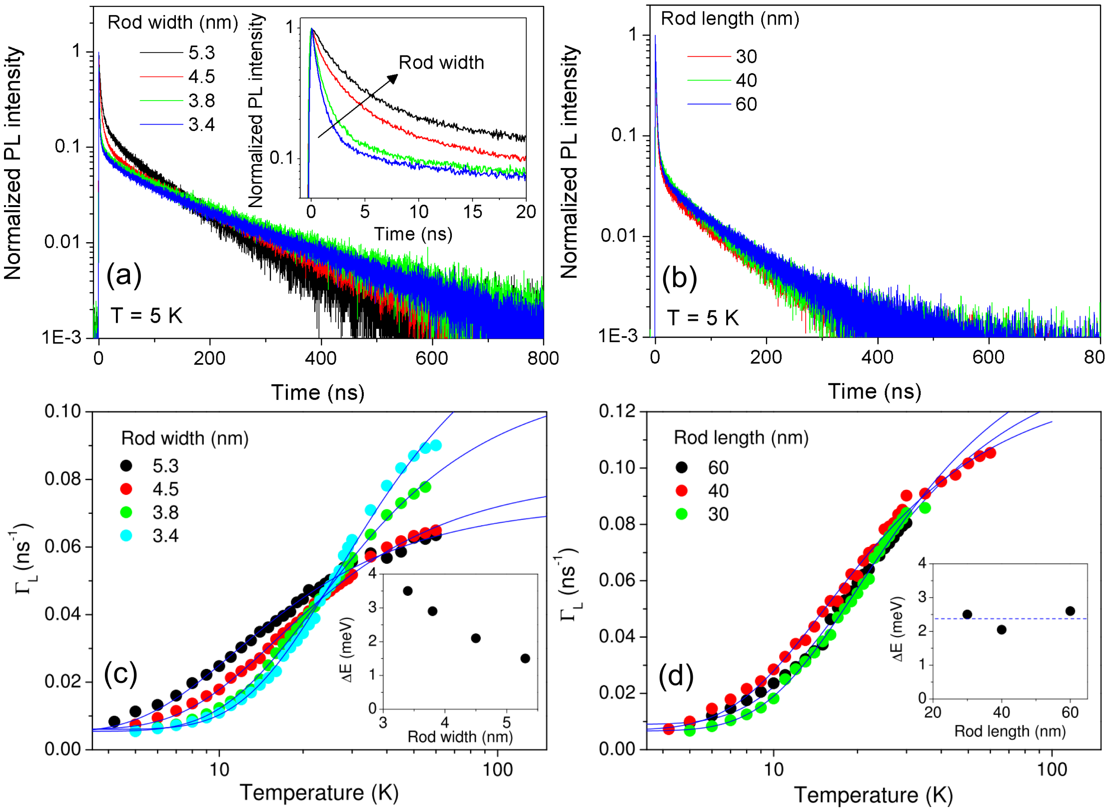

Figure 4-6: (a) PL decay for samples with similar core size (D = 2.5 nm) and different rod widths (samples #1,#1a,#2,#3 in Table 3-3). The inset shows the decay at early times. (b) PL decay for samples with similar core size (D = 3.2 nm) and different rod lengths (samples #4,#4a,#5 in Table 3-3). Evolution of the long component of the PL decay with temperature for various (c) rod widths and (d) rod lengths. Blue lines are fits according to Eq.(4.3). The insets show the bright-dark energy splitting obtained from the fits as a function of rod width in (c) and as a function of rod length in (d).

modified eh-exchange interaction. [66] Consequently, since the rod length does not influence the electron and hole wavefunctions for the extensions considered here, it does not influence the bright-dark energy splitting either.

ΔE_{bd} was determined for all DiR samples listed in Table 3-3 using the method described above. The resulting values are plotted in Fig. 4-7 (a) as a function of shell thickness. The previously observed trend of a decreasing energy splitting with increasing shell thickness is consistent for each set of samples with a specific core size and in the range of shell thicknesses of the samples investigated here (0.3 nm up to 1.5 nm) the energy splittings vary by approximately 3.5 meV. This change in ΔE_{bd} is comparably large, since in a similar experimental study on spherical CdSe/CdS NCs a change in ΔE_{bd} by 2 meV was determined for a change of shell thickness from approximately 1 nm to 6 nm [38] and for bare CdSe NCs a change of 1 meV was observed for a change of 5 nm in NC diameter. [117] However, the large energy splittings observed in this experiment are in accordance with theoretical calculations for bare CdSe NCs, which predict a higher sensitivity of ΔE_{bd} on the NC size (0.2 − 13.5 meV for a change in NC size from 10 nm to 2 nm, [28] 3 − 17 meV for a change in NC size from 7.5 nm to 1.7 nm, [68] or 4.4 − 16 meV for a change in NC size from 3.7 nm to 1.9 nm. [67])

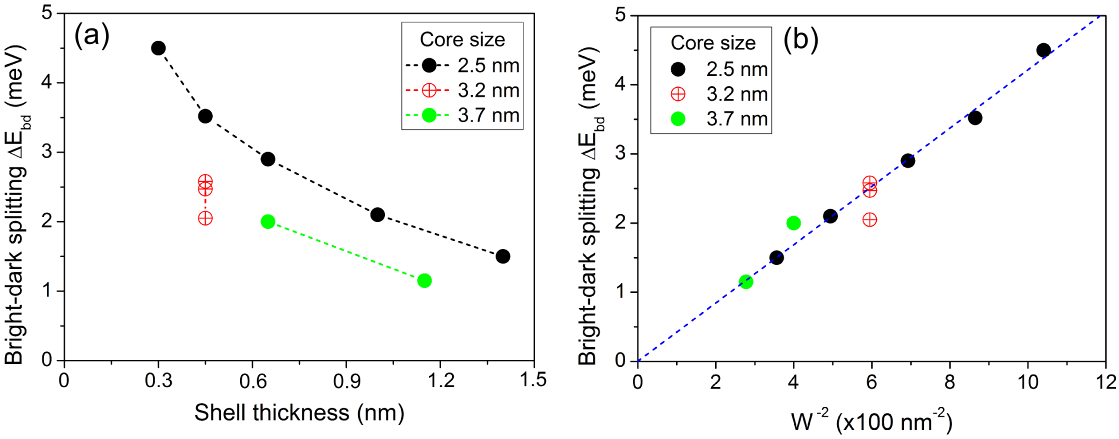

Figure 4-7: Bright-dark energy splitting as a function of (a) shell thickness and (b) inverse squared rod width W^{-2}. Dashed lines are guides to the eye.

In Fig. 4-7 (b) the determined energy splittings are plotted as a function of the inverse squared rod width W^{-2}. Apparently, there is a quadratic dependence between ΔE_{bd} and the rod width, regardless of the core size and rod length. In a bare spherical NC (i.e. without a shell) the short-range exchange interaction strength and thereby the energy splitting decreases inversely proportional to the volume of the NC, i.e. $\Delta E_{bd} \propto 1/R^3$, where R is the NC radius. [7,28] Therefore, in a nanostructure with two-dimensional confinement a square dependence on the diameter can be expected. However, in a core/shell structure the situation is more complicated due to the different confinement for the electron and the hole. The core size is expected to strongly influence the eh-wavefunction overlap, since it affects the confinement of both carriers. As shown in Ref. [36], this decides, wether electron and hole show either type-I or type-II behavior. This could also explain the tendentially lower energy splittings for larger core sizes in Fig. 4-7 (a). In contrast, the overall diameter (or shell thickness) should predominantly influence the electron, because the hole is more strongly confined to the core due to its comparably large effective mass.

It is worth noting, that many-body pseudopotential calculations of the exciton fine structure in spherical CdSe NCs yielded an inverse square dependence of the energy splitting between bright and dark excitons states on the NC size. These calculations, in contrast to the EMA approach of Efros et al., consider the presence of a long-range part of the eh-exchange interaction, which is made responsible for the discrepancy between the models regarding the singlet-triplet splitting. [68,126]

Bright and dark exciton radiative rates

Apart from the energy splitting, the fit of the temperature dependence of the long PL decay component with Eq.(4.3) yields the radiative recombination rates/times $\Gamma_{A,F}/\tau_{A,F}$ for the bright (A) and the dark (F) exciton state. In the following passage, the dependences of the radiative rates on the shell shape are discussed.

Figure 4-8 (a) shows the radiative recombination time (lifetime) of the bright exciton state as a function of the rod width W for all studied DiR samples. The times vary between approximately 3 ns and 7 ns. These lifetimes have a comparable magnitude to

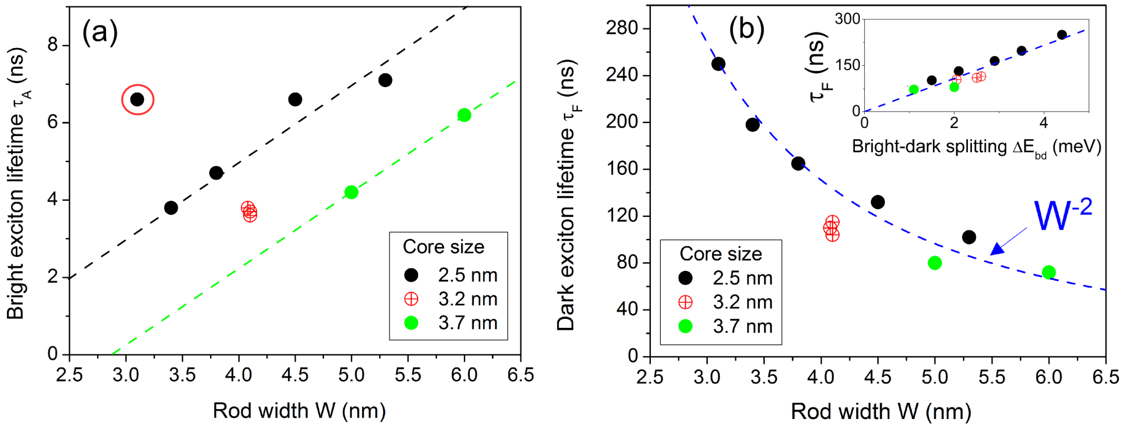

Figure 4-8: (a) Bright exciton radiative lifetime as a function of rod width W. The red circle marks a value, which strongly deviates from the trend, which is indicated by the dashed black and green lines. (b) Dark exciton radiative lifetime as a function of rod width W. The dashed blue line is is a polynomial interpolation. The inset depicts the dependence of the dark exciton radiative lifetime on the bright-dark energy splitting ΔE_{bd}. Here, the dashed blue line serves as guides to the eye.

values reported in other experimental studies ($\tau_A = 7.7$ ns for single CdSe/ZnS core/shell NCs of comparable size [116] or $\tau_A = 8$ ns for bare CdSe NC with sizes around 2 nm [116]) and theoretical predictions of 13.3 ns for the $\pm 1^L$ radiative lifetime in bare CdSe NCs with a size of 1.2 nm, obtained in the framework of the multiband EMA. [28] For a given core size, with increasing rod width (or shell thickness) the radiative recombination time increases (strong deviations from this trend are tagged with a red circle). This observation can be attributed to the decreasing eh-wavefunction overlap with increasing shell thickness. As stated earlier, in the EMA the radiative rate of the bright exciton is typically directly proportional to the square of this overlap $\Gamma_A \propto \Theta_{e-h} = |\int d^3r \Psi_e(r)\Psi_h(r)|^2$. With increasing electron leakage into the shell, the spatial overlap between electron and hole decreases. This effect was also observed in time-resolved PL experiments at higher temperatures. [38] However, at elevated temperatures the population between the fine structure states is not affected by changes in the exchange interaction energy due to the high thermal energy of the excitons. At low temperatures, there is a competitive effect regarding the PL decay because of variations in the radiative rates as a result of changes in eh-wavefunction overlap and changes in the bright-dark energy splitting due to the varying exchange interaction. This aspect has also been addressed in Ref. [38]. Nevertheless, the observed trend, i.e. an increase of the bright exciton radiative lifetime with increasing shell thickness, can be explained by the decrease of the eh-wavefunction overlap, due to progressive electron delocalization into the shell.

In Fig. 4-8 (b) the dark exciton radiative lifetime τ_F is shown as a function of rod width and apparently, τ_F exhibits a systematic dependence. As the rod width is increased from 3 nm to 6 nm, τ_F decreases from approximately 250 ns to 70 ns. Regardless of the core size the lifetime seems to depend inversely proportional on the square of the rod width, as indicated by a polynomial interpolation shown as a blue dashed line. This observation can be qualitatively explained, by considering the changes in the exciton fine structure as a consequence of the change in nanoparticle shape. The inset in Fig. 4-8 (b) shows the dark exciton lifetime as a function of the bright-dark energy splitting and it

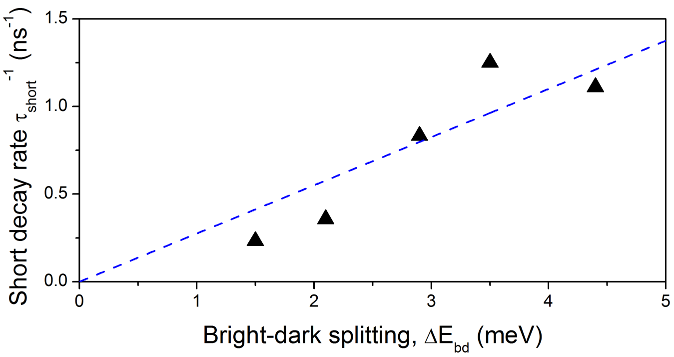

Figure 4-9: Dependence of the short decay rate on the bright-dark energy splitting. The dashed blue line serves as a guide to the eye.

clearly follows a linear dependence. As described in section 2.2.4, the exciton ground state theoretically has an infinitely long radiative lifetime, since it is optically forbidden in the electric dipole approximation. One possible recombination pathway for the dark exciton is coupling to optical allowed states by magnetic field induced mixing. The strength of this effect, is inversely proportional to the energy splitting between the bright and the dark states, [28, 117] in accordance with the experimental observation described here. However, since no external field was applied in this experiment, an internal mechanism has to be the origin for the observed dependence. In this context the role of paramagnetic defects [28] or surface dangling bonds, [122] which can give rise to internal effective magnetic fields, has often been discussed. Remarkably, the magnitudes of the dark exciton lifetimes deduced from the fits are significantly smaller, compared to values reported in experimental studies on spherical CdSe/CdS core/shell NCs of comparable size ($600-700$ ns for CdSe/CdS core/shell NCs with 3 nm core size and approximately 1 nm shell thickness in Ref. [38]). This indicates, that the shell shape gives rise to this deviation. One important difference between these structures is the surface, which is experienced by the electron and this indicates a surface-assisted mechanism to be the origin for dark exciton radiative recombination. This aspect will be addressed in more detail in chapter 6.

As mentioned in section 4.2, at low temperatures the short component of the PL decay corresponds to the bright to dark spin flip rate γ_0. However, the strong multiexponential shape of the decays at early times, obvious for example from the insets of Fig. 4-6 (a), makes a determination of τ_{short} difficult. Here it is estimated for several samples by extracting the time, where the intensity dropped to the fraction $1/e$, at $T = 4.2$ K. In Fig. 4-9 the resulting short decay rate τ_{short}^{-1} is plotted as a function of ΔE_{bd} for the samples #1, #1a, #2, #3 and #3a, all of which exhibit a core size of 2.5 nm. The rates vary between 0.23 ns^{-1} and 1.25 ns^{-1} and they seem to increase with an increasing energy splitting. This could be related to the existence of an acoustic phonon bottleneck, which was previously observed for spherical NCs in a magnetic field experiment. [85] As explained in section 2.3.1, long wavelength acoustic phonons are suppressed in NCs, because of their limited size. Therefore the transition between states with small energy splitting is hindered, leading to long spin flip times, in accordance with the experimental results shown in Fig. 4-9. For the samples considered here, the bright-dark spin flip time is found to be on the order of $1-2$ ns at $T = 4.2$ K.

4.4 Summary

By means of time-resolved PL spectroscopy it was investigated, how the bright-dark energy splitting and the radiative lifetimes of the two lowest exciton fine structure states depend on the shell shape in DiR NCs. The general trend of a decreasing energy splitting with increasing NC size or shell thickness, which was observed in previous experiments on spherical NCs, [38, 117] could be confirmed. Further, the experimental results indicate, that in NCs with partial two-dimensional confinement (as is the case in DiRs for the electron due to its leakage into the shell) the eh-exchange interaction and thereby the singlet-triplet splitting exhibit an inverse square dependence on the size of the confining potential, which for the electron is constituted by the shell.

The spectral red-shift of the PL maximum and the change in the PL decay with increasing rod diameter in combination with the lack of dependence on the rod length support recent theoretical predictions of electron localization in the vicinity of the core, although due to its lower conduction band offset and its comparably low effective mass it can significantly leak into the shell. [127]

Regarding the radiative lifetimes it was found, that the bright exciton lifetime increases with increasing rod width, because for a given core size an increase of the rod width reduces the eh-wavefunction overlap and thereby the probability for radiative recombination. In contrast the dark exciton lifetime decreased with increasing rod width. Importantly, a linear dependence between the dark exciton lifetime and the bright-dark energy splitting was found, which indicates, that the dark exciton radiative recombination occurs via the mixing of dark and bright exciton states. Thus an increase of the bright-dark splitting leads to a weaker admixture. The comparably small magnitude of the dark exciton lifetimes compared to reported values for spherical core/shell NCs with similar size, highlights the importance of the NC surface for dark exciton radiative recombination.

By determination of the short decay time, the bright-dark spin flip time was estimated. For the studied structures it was found to be on the order of $1 - 2$ ns and to decrease with increasing energy splitting. This observation was attributed to the excistence of a phonon bottleneck, which occurs in nanometersized structures and hinders relaxation between states with small energy splitting.

Chapter 5

Exciton spin dynamics and photoluminescence polarization of CdSe/CdS nanocrystals in high magnetic fields

In the preceding chapter special attention was given to the architecture of the fine structure, notably the splitting between spin singlet and triplet states, and its dependence on the shape and size of the NC. Furthermore, the dependence of the bright and dark exciton radiative rates on the shell shape has been addressed.

This chapter deals with the relaxation of the exciton spin and with the magnetic field induced circular polarization of the PL in CdSe/CdS core/shell NCs, with special attention to DiR NCs. As discussed in section 2.2.4, the application of an external magnetic field, leads to a splitting of the fine structure states with nonzero angular momentum. This gives rise to circular polarized PL from the Zeeman-split sublevels and to spin relaxation between them. In this regard, the dependence of spin relaxation and PL polarization on the architecture of the NC as well as on magnetic field and temperature is experimentally investigated. Furthermore, this chapter provides a theoretical description of the PL circular polarization in an external magnetic field. The presented model includes effects related to the shape of the NC shell, the configuration of the fine structure states and to the orientation of the NC hexagonal axis with respect to the magnetic field.

In the beginning of this chapter essential results of preliminary studies are summarized and the scientific relevance of the experiment is discussed. Following that, some experimental details and the technique for investigating exciton spin dynamics and circular polarization in external magnetic fields are described. Later on, the experimental results are discussed and interpreted. Subsequently, the theory for predicting and analyzing circular and linear polarization of NCs in magnetic field is presented and compared to the experimental results. Finally, a summary of the findings is given.

5.1 Introduction

As discussed in section 2.3.2, at low temperatures the optical response of a NC is strongly dependent on the exciton fine structure, because the small thermal energy of the excitons at low temperatures leads to a population of the energetically lowest lying states only. Thus, the optical response depends on the ordering of the fine structure states, which have a characteristic radiative recombination time and therefore strongly influence the dynamics of exciton radiative recombination. A recent experimental study evidenced, that in DiRs, despite the strongly anisotropic shell shape, the band-edge exciton fine structure level ordering is comparable to the spherical case, [102] which is depicted in Fig. 2-6 (a) in section 2.2.3. In this case the lowest exciton ground state has a total angular momentum projection of $F = \pm 2$ and the subsequent energetically higher lying state is of type $F = \pm 1$.

In section 2.2.4 it was shown, that a magnetic field parallel to the hexagonal axis of CdSe NCs lifts the degeneracy of the $F = \pm 1$ and $F = \pm 2$ exciton states, as illustrated in Fig. 5-1 (a). At zero field each of the dark and bright exciton states, which are denoted by $|F\rangle$ and $|A\rangle$, respectively and which are separated by the bright-dark energy splitting ΔE_{bd}, is twofold degenerate. In the presence of an external field it splits into a Zeeman-doublet. Typically, due to its larger exciton g factor, the $F = \pm 2$ exciton exhibits a larger splitting compared to the $F = \pm 1$ state. [28] The splitting of the exciton states in magnetic field has two important consequences, which are of interest in this study. On the one hand, the Zeeman-splitting affects exciton dynamics, since it leads to additional spin relaxation processes between the Zeeman sublevels, which occur after excitation and until thermal equilibrium is achieved. On the other hand, it leads to circularly polarized PL emission of the NC. These aspects are discussed in more detail in the following.

In zero magnetic field, after nonresonant excitation the excitons quickly relax into the lowest lying energy states and establish a thermal equilibrium. Notably, the time required for relaxation from the bright to the dark exciton state [denoted by τ_{AF} in Fig. 5-1 (a)] is important here, since it strongly influences the exciton radiative recombination, as discussed already in chapter 4. This process involves the spin flip of either the electron or the hole. It was shown in the previous chapter, that for the samples studied here the timescales of bright to dark relaxation are on the order of $1 - 2$ ns at 4.2 K. In magnetic field, however, also exciton relaxation between the Zeeman-sublevels occurs, which involves the simultaneous spin relaxation of the electron and the hole. It is therefore expected, that this process occurs on a longer timescale [the characteristic spin relaxation time is denoted by τ_s in Fig. 5-1 (a)] compared to the bright to dark relaxation. While the relaxation between the bright exciton states and also the relaxation from the bright to the dark exciton states has been experimentally investigated for spherical core only and core/shell NCs [119, 128] and also for DiRs, [110, 129–134] there are only a few studies in magnetic field, dealing with the relaxation between Zeeman-sublevels in magnetic fields. Up to now, such studies solely investigated the spin relaxation of charged excitons in magnetic field [103] or the spin relaxation of excitons in different materials, such as CdTe. [135] As mentioned in the introductory chapter, the understanding of the processes, which lead to relaxation of the exciton spin in NCs, is important, since it enables to design for instance spin-preserving environments, which are required for long-lived spin memory applications. This study provides new insights in how the spin relaxation of neutral excitons between the dark exciton states split in magnetic field is affected by the magnetic field strength, the temperature and the architecture of CdSe/CdS core/shell NCs.

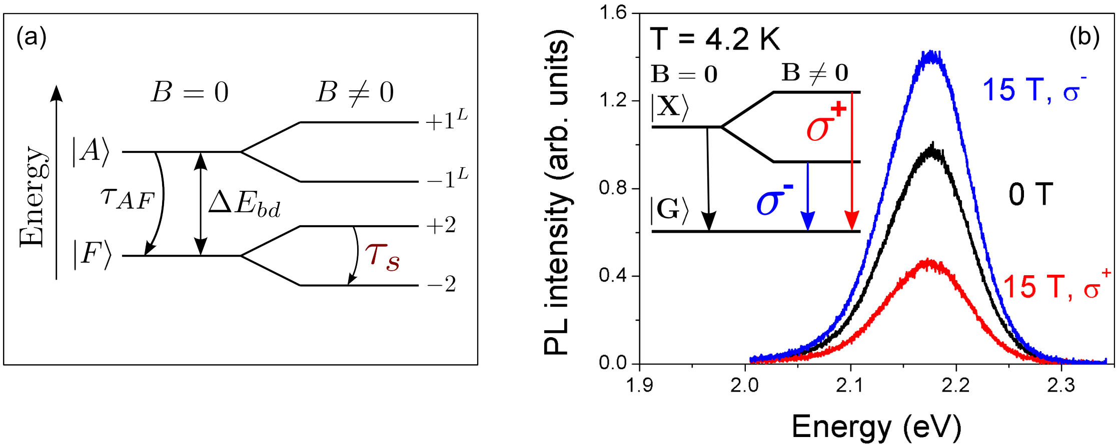

Figure 5-1: (a) Model of the lowest exciton fine structure states for zero and non-zero magnetic field. (b) Photoluminescence spectra of DiR sample #1 at $B = 0$ T and 15 T. Red and blue curves are the σ^+ and σ^- polarized components, respectively. The black curve corresponds to the unpolarized transition, as illustrated in the inset.

Due to the thermal population of the Zeeman-split sublevels, the PL from these states gets circularly polarized. In general, the degree of circular polarization P_c of the PL is defined by

$$P_c = \frac{I_{\sigma+} - I_{\sigma-}}{I_{\sigma+} + I_{\sigma-}}, \tag{5.1}$$

where $I_{\sigma+}$ and $I_{\sigma-}$ are the PL intensities of the right- and left- circular polarized components, respectively. Figure 5-1 (b) shows typical polarization-resolved PL spectra of a DiR sample at $B = 0$ T and 15 T. While at zero magnetic field the PL is completely unpolarized, it exhibits a strong DCP of 0.5 at 15 T, which arises from the transitions from the Zeeman-split sublevels of an excited state to the ground state in magnetic field, as illustrated in the inset of Fig. 5-1 (b).

The dependence of P_c on magnetic field was subject to several theoretical and experimental studies on spherical core only and core/shell NCs. [43–45,119,120] Notably it has been shown, that the circular polarization of the PL of an ensemble of spherical NCs can be very well explained by assuming, that the radiative recombination of the dark exciton occurs via coupling of the $F = \pm 2$ and the $F = \pm 1$ states. [28,43] Due to the coupling, the dark exciton recombines with the polarization properties of the $F = \pm 1$ states, although the DCP of the PL is gouverned by the thermal population of the dark exciton states. As discussed in section 2.2.4, the magnitude of the Zeeman-splitting depends on the orientation of the NC with respect to the magnetic field, because of the internal crystal structure anisotropy of wurtzite type NCs. This theoretically limits the maximum PL DCP of an ensemble of spherical NCs to 75 %. [43] However, in several high magnetic field experiments on spherical core/shell NCs DCPs much lower compared to this limit have been reported and could not be satisfactorily explained. Moreover, studies on DiRs in this regard have not been conducted up to now. On the one hand, it is especially interesting, whether the anisotropic shape of the shell leads to lower circular polarization of the PL compared to spherical NCs, due to a presumably intrinsically higher linear polarization (studies investigating the linear polarization of DiR PL at low temperatures are still missing). On the other hand, DiR ensembles are very suitable for the study of orientation effects, since it was shown, that macroscopic alignment of DiRs with a specific orientation can be achieved by appropriate sample preparation methods. [108, 136–139] Apart from exciton spin relaxation, these aspects are of central interest in this study. It includes the experimental investigation of the dependence of the DCP on the magnetic field strength, the temperature, the orientation of DiRs and the geometry of the NC shell. Furthermore, a theoretical model is presented, which can be used to predict and analyze the circular polarization of core/shell NCs in an external magnetic field. It is based on the common model of dark exciton coupling to the bright exciton $F = \pm 1$ states, but it includes novel aspects, such as an alternative coupling of the dark exciton to $F = 0$ states and the dielectric enhancement effect (see section 2.4.2). Both effects enhance the linear polarization along the hexagonal c-axis of the NC and, as will be shown, thereby lead to a reduction of the circular PL polarization in an external magnetic field.

5.2 Experimentals

Samples and experimental details

All samples, which are referred to in this chapter, are CdSe bare cores and CdSe/CdS core/shell NCs with spherical or DiR shape. The samples with corresponding geometrical parameters are listed in Table 3-3 (all of the listed samples have been studied except for samples marked by an "a" behind the index). For magneto-optical PL measurements, a solution of NCs with a concentration of few μM in toluene was deposited by drop-casting method on a glass slide, which was then mounted into the optical cryostat (the corresponding experimental setup is depicted in Fig. 3-2 in chapter 3). In experiments utilizing magnetic fields the orientation of the field with respect to the sample is crucial. In this case, the field was directed parallel to the light detection/excitation axis (i.e. a Faraday geometry was used) and perpendicular to the substrate. The sample holder was mounted on top of a stack of three nanopositioners, allowing for precise positioning in three spatial directions. By scanning over an area of the sample and by simultaneously exciting the sample and detecting the PL intensity an image of the sample could be obtained. This technique is called Laser Scanning Microscopy and it yields information on the distribution of the NCs on the substrate, if scattered/reflected light is suppressed. The circular polarization of the PL was analyzed by a combination of a quarter wave plate and a Glan-Thomson-prism. When the quarter wave plate is correctly set, it converts circular polarized light in linear polarized light and vice versa. Right-handed circular polarized light and left-handed polarized light result in linear polarized waves, with their polarization directions oriented perpendicular to each other. Therefore, with the Glan-Thomson-prism the respective component could be selected and analyzed. In the experiment described here the time-resolved DCP (TRDCP) was analyzed by measuring the polarization-resolved and spectrally-integrated intensities $I_{\sigma+}$ and $I_{\sigma-}$ as a function of time and calculating

$$P_c(t) = \frac{I_{\sigma+}(t) - I_{\sigma-}(t)}{I_{\sigma+}(t) + I_{\sigma-}(t)}. \tag{5.2}$$

Experimental investigation of the equilibrium DCP and exciton spin dynamics

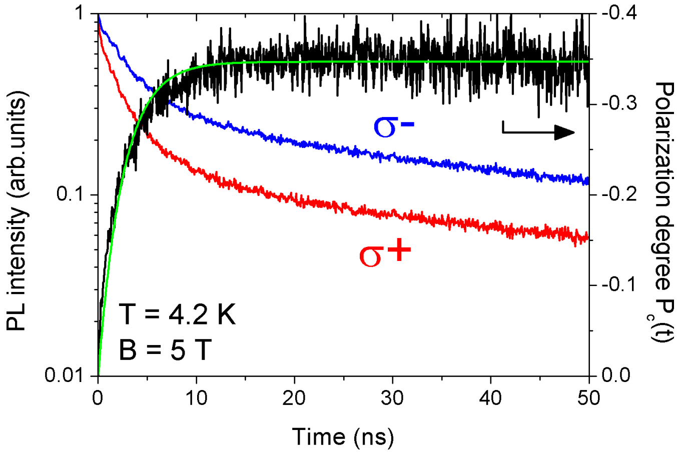

Figure 5-2: A typical polarization-resolved PL decay and the resulting TRDCP for sample #1, recorded at $T = 4.2$ K and $B = 5$ T. The green curve is a fit according to Eq.(5.3).

Exciton spin dynamics and the equilibrium DCP can be investigated by analyzing the TRDCP $P_c(t)$, as defined by Eq.(5.2). The experimental procedure for determining $P_c(t)$ is shown in Fig. 5-2. After pulsed excitation (the laser energy is 3.06 eV), the σ^+ and σ^- polarized components are traced over time. The time resolved DCP, which is shown as a black curve, is calculated according to Eq. (5.2). Just after excitation the PL is unpolarized, because the nonresonant photoexcited excitons are equally distributed between the Zeeman-split sublevels. In the following the excitons relax into the energetically lower spin state until they achieve thermal equilibrium, which is evident from the plateau of the DCP in Fig. 5-2. The characteristic time of the spin flip process involved can be quantified by determination of the risetime of the TRDCP. In the experiment the dependence of the equilibrium PL polarization and the spin relaxation time (or rate) on magnetic field, temperature and shape of the NCs was investigated. To this end, the time-resolved DCP curves were fitted with the equation

$$P_c(t) = P_c^{eq}[1 - \exp(-t/\tau_s)], \tag{5.3}$$

where P_c^{eq} denotes the DCP in thermal equilibrium and τ_s the spin relaxation time. A typical fit is plotted as a green curve in Fig. 5-2.

5.3 Experimental results and discussion

In this section, the experimental results are discussed and interpreted. In the beginning the effect of orientation of individual NCs with wurtzite crystal structure on the circular polarization of the ensemble PL in magnetic field is discussed and experimental evidence of this effect is presented. Afterwards, the experimental results on exciton spin dynamics and the equilibrium DCP are shown and discussed.

Effect of NC orientation on DCP

In NCs with a wurtzite crystal structure, due to the internal crystal anisotropy the exciton spin is constrained to lie along the hexagonal c-axis of the crystal. [43] As a result, the magnitude of the Zeeman splitting depends on the angle Θ between the crystal c-axis and the direction of the magnetic field: $\Delta E = g_{ex}\mu_B \mathbf{B}\cdot\mathbf{c} = g_{ex}\mu_B B\cos\Theta$, where g_{ex} is the exciton g factor and μ_B the Bohr-magneton. The intensities $I_{\sigma\pm}$ in Eq. (5.1) become angle dependent too. The probability for detecting circular polarized light at an angle Θ with respect to the magnetic field axis is proportional to $(1 \pm \cos\Theta)^2$. [43] Thus, for an ensemble of NCs $P_c(B)$ is derived by integrating Eq. (5.1) over all possible angles

$$P_c(B) = \frac{\int_0^1 [I_{\sigma+}(x) - I_{\sigma-}(x)] f_{\mathrm{or}}(x)dx}{\int_0^1 [I_{\sigma+}(x) + I_{\sigma-}(x)] f_{\mathrm{or}}(x)dx}. \tag{5.4}$$

Here, $x = \cos\Theta$ and $f_{\mathrm{or}}(x)$ is a weighting function describing the orientation properties of the ensemble.

Assuming a thermal distribution in equilibrium between the Zeeman-split sublevels, the DCP calculates as

$$P_c^{\mathrm{eq}}(B) = \frac{\int_0^1 2x\tanh(\Delta E/2k_BT) f_{\mathrm{or}}(x)dx}{\int_0^1 (1+x^2) f_{\mathrm{or}}(x)dx}, \tag{5.5}$$

where k_B is the Boltzmann constant. For an ensemble of randomly oriented NCs the angles between the crystal c-axes and the magnetic field direction are uniformly distributed over all angles between 0° and 90°, i.e. $f_{\mathrm{or}}(x) = 1$. In this case, the integration over all x leads to a theoretical limit for the DCP of 0.75 (i.e. 75 %). However, for NCs with an anisotropic shape, such as nanorods or DiRs the situation can be different. It is well known, that in DiRs the c-axis of the core is typically parallel to the long axis of the rod [31] and several methods have turned out to be suitable to prepare nanorod or DiR ensembles with macroscopic alignment and orientation properties. [108, 136–139] According to Eq.(5.5), it should be possible to probe the orientation of such ensembles with respect to the magnetic field axis by measuring $P_c^{\mathrm{eq}}(B)$. If $f_{\mathrm{or}}(x) = \delta(x)$, corresponding to the case when the angle between magnetic field and the emitting DiRs is 90°, the PL polarization at any given field $P_c^{\mathrm{eq}}(B)$ is expected to vanish. On the contrary, if the angle is 0°, i.e. $f_{\mathrm{or}}(x) = \delta(x-1)$, the resulting $P_c^{\mathrm{eq}}(B)$ is maximal and depends only on the ratio $\Delta E/2k_BT$. Thus, for fully spin polarized excitons the DCP is $P_c^{\mathrm{eq}}(B) = 1$.

The effect of DiR orientation on $P_c^{\mathrm{eq}}(B)$ was studied by measuring the magnetic field induced DCP of DiR samples prepared by the drop-casting method at different positions. When a solution of highly concentrated NCs is drop-casted on a substrate, its distribution on the substrate is subject to the so-called “coffee stain effect”. [140–142] Due to this effect the particles in a drying liquid accumulate in the outermost part of the droplet, leading to the formation of coffee stain rings, in which the particles are densely packed. A photograph of a typical coffee stain ring is shown in Fig. 5-3 (a). The dynamics of evaporation, which lead to this effect are illustrated in Fig. 5-3 (b). The evaporation of the liquid (evaporated liquid is depicted as a red shaded area) gradually changes the height of the droplet. At the perimeter, however, the contact line is pinned to the surface, preventing the droplet from shrinking. The loss of liquid at this position has to be compensated for, thus a capillary flow of liquid from the inner part of the droplet

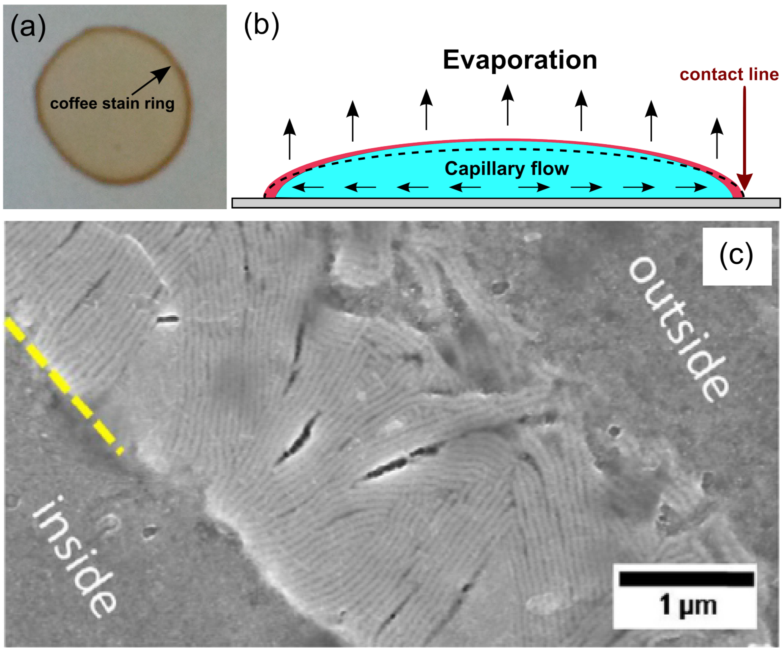

Figure 5-3: (a) A photograph of a dried coffee droplet. (b) Illustration of the evaporation dynamics leading to the coffee stain ring. (c) Scanning electron microscope image of a coffee stain ring section of colloidal nanorods. This image is taken from Ref. [140].

to the outer part is generated. Thereby particles are transferred to the outermost part of the drying droplet. As shown in Fig. 5-3 (c), for colloidal nanorods prepared by this method, nanorods can be macroscopically aligned in the coffee stain rings. They tend to lie parallel to each other and parallel to the substrate, whereas in the regions outside these rings the nanorods exhibit no specific ordering and their orientation is random. [140]

Figure 5-4 (a) shows a laser scanning microscope image of a coffee stain ring section for sample #5. The spatial resolution is 10 μm. The intensity is coded in a logarithmic grey scale, white corresponds to high intensities. The observed high intensity in the ring indicates densely packed DiRs in this area. In the inner part of the ring (grey area) the DiR density is significantly smaller. It is very small, while still measurable, outside the ring (black area). In order to deduce information about the rod orientation, the time-integrated DCP was measured, while scanning over the ring at $B = 5$ T and at a temperature $T = 4.2$ K [see Fig. 5-4 (b)]. As can be seen from Eq.(2.41) the time-integrated DCP is equal to the equilibrium DCP for the case when the spin relaxation time is small compared to the radiative recombination time. As will be shown later on, for the samples investigated here, this is always the case. The green data points correspond to the overall intensity measured at each position, the open circles represent the time-integrated DCP calculated from Eq.(5.1). It is obvious that the DCP drops almost to zero in the middle of the ring stripe and it increases during the transition into the surrounding areas. The observed DCP decrease is due to rod alignment parallel to the surface and therefore the angle between the magnetic field and the majority of the rods in this region is 90°, resulting in a vanishing Zeeman splitting. Outside of the region of the ring stripe the DiR orientation is random, therefore the non-zero Zeeman-splitting gives rise to circular polarized PL.

The technique described above is suitable to yield information about nanorod orien-

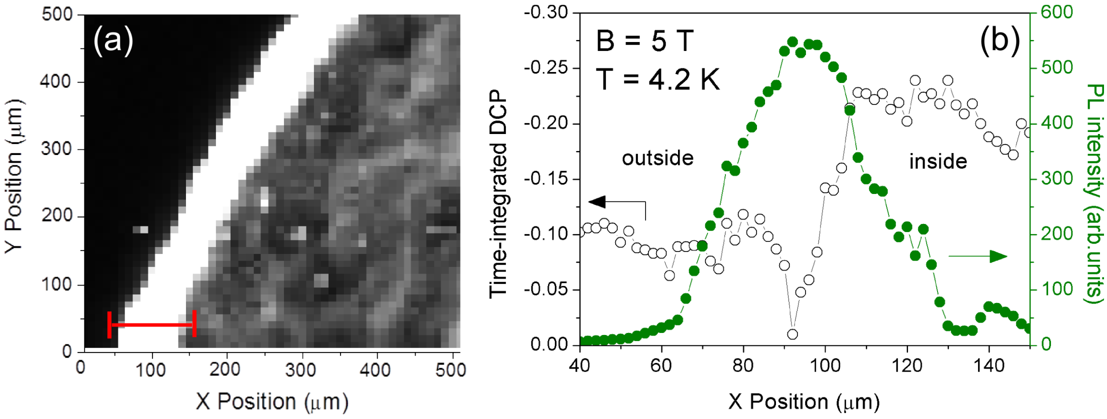

Figure 5-4: (a) Confocal laser scanning microscope image of a coffee stain ring section of sample #5. The red line indicates the region, which was chosen for a linear scan shown in (b). Here, the overall intensity is depicted as green, solid circles and the DCP as open circles.

tation only with respect to the magnetic field axis, which is in this case oriented perpendicular to the sample substrate. However, it could be used for checking the quality of devices based on colloidal nanorod arrays, for which a large-scale nanorod alignment is required. Although this method cannot compete with electron microscopy techniques in terms of resolution, it clearly has some advantages. While for TEM imaging special carbon grids, which are transparent to the electron beams, have to be used, the method described here is applicable to a wide range of substrates, such as glass or wafer materials. Furthermore, while with TEM, the investigatable area is typically limited to a few microns, the optical technique can be applied on ranges up to the centimeter scale. The resolution of this method is limited by diffraction to several hundred of nanometers, depending on the laser wavelength and the numerical aperture of the optical excitation and detection system.

Analysis of the time-resolved DCP

In order to investigate the mechanism of spin relaxation and the dependence of NC shape on the equilibrium DCP, the TRDCP was measured as a function of magnetic field and temperature for NCs of different size and shape. In Fig. 5-5 typical TRDCP curves of DiRs are shown, which were measured as a function of magnetic field at $T = 4.2$ K in (a) and as a function of temperature at $B = 5$ T in (b). The red curves are fits of the experimental data with Eq.(5.3). From these curves the following qualitative observations can be made: On the one hand, with increasing magnetic field the spin relaxation rate increases, obvious from the faster increase of the TRDCP at high magnetic fields. At the same time, the equilibrium DCP increases, which results from the increase of the Zeeman-splitting and consequently less thermal population of the upper Zeeman-sublevel at a given temperature. On the other hand, an increase of the temperature leads to a decrease of the equilibrium DCP, due to the increasing thermal energy of the excitons, which leads to progressive population of the upper lying Zeeman-sublevel. The relaxation rate, however, also increases with increasing temperature. This observation indicates a phonon mediated process, as will be discussed in more detail later on.

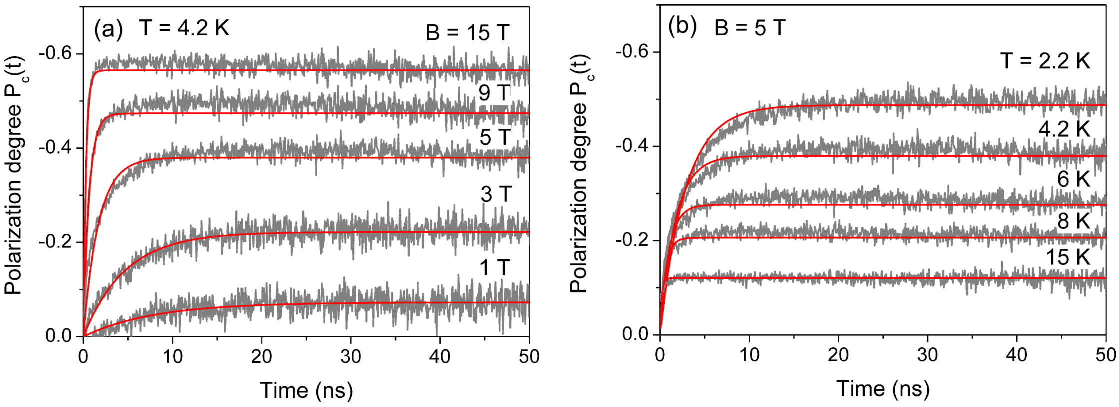

Figure 5-5: (a) Magnetic field dependence and (b) temperature dependence of the TRDCP for sample #1. The red curves are fits according to Eq.(5.3).

As described in section 5.2, the fit of the TRDCP curves with Eq.(5.3) yields the spin relaxation time τ_s (or rate $1/\tau_s$) and the equilibrium DCP P_c^{eq}. In the following sections, the dependence of $1/\tau_s$ and P_c^{eq} on magnetic field, temperature and NC architecture are investigated in more detail.

Exciton spin dynamics

Figures 5-6 (a) and (b) show the spin relaxation rate $1/\tau_s$ for sample #1, obtained from the fit of the TRDCP curves with Eq.(5.3), as a function of magnetic field and temperature. As can be observed from Fig. 5-6 (a), the spin relaxation rate is strongly dependent on the magnetic field strength. At $T = 4.2$ K the spin relaxation rate increases from $1/\tau_s \approx 0.1\ \mathrm{ns}^{-1}$ to $3.3\ \mathrm{ns}^{-1}$ (this corresponds to a shortening of the relaxation time from $\tau_s \approx 10$ ns to 0.3 ns), as the magnetic field is increased from $B = 0$ T to 15 T. The observed long spin relaxation time at low fields confirms the expectation, that spin relaxation between the dark exciton states occurs on much longer time scale, compared to the bright-dark spin flip, which was found to occur on the order of $1-2$ ns (see preceding chapter). As one can observe from the inset of Fig. 5-6 (a), at low magnetic fields the spin relaxation rate follows a cubic magnetic field dependence and it starts to deviate from this trend at $B \approx 8$ T. At high fields the rate seems to depend linearly on the magnetic field. The temperature dependence of the spin relaxation rate is a linear function, as can be seen in Fig. 5-6 (b). Here, the temperature is increased from $T = 2.2$ K up to 12 K and the spin relaxation rate increases by about one order of magnitude. The linear dependence on temperature points towards a phonon mediated process. For confined phonon energies much smaller than the thermal energy, the Bose-Einstein distribution for the phonon occupation can be approximated by a linear temperature dependence: $N_{\omega_q} = 1/(e^{\hbar\omega_q/k_BT} - 1) \approx k_BT/\hbar\omega_q$, where ω_q is the frequency of a phonon with wavenumber q.

In Fig. 5-7 (a) the magnetic field dependence of the spin relaxation rate is shown for all studied DiR samples as well as the spherical samples #R1 and #R3. All of them show qualitatively the same trend, i.e. at low fields the spin relaxation rate follows a cubic dependence, as highlighted for selected samples in Fig. 5-7 (b), while at higher fields a linear magnetic field dependence is present. However, the spin relaxation rate seems to be strongly dependent on the core size and independent of the shell shape. The latter

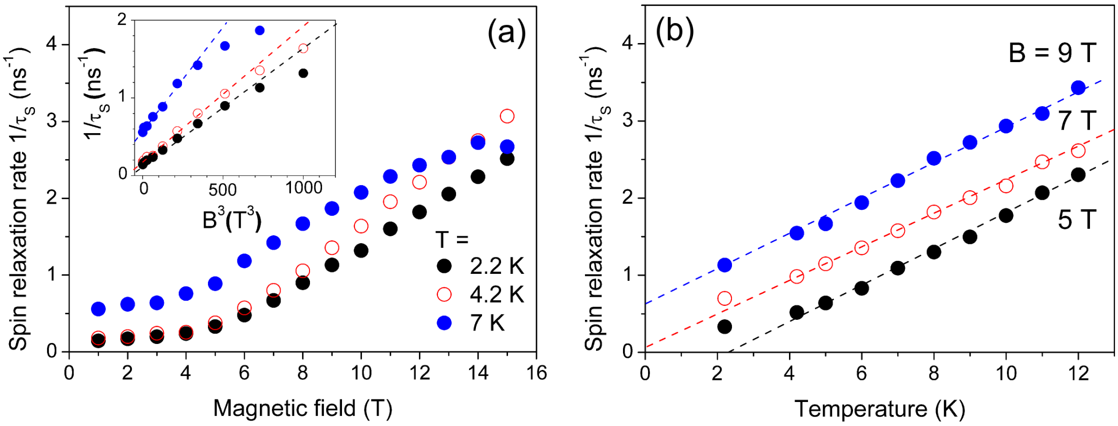

Figure 5-6: (a) Magnetic field dependence and (b) temperature dependence of the exciton spin relaxation rate $1/\tau_s$ for sample #1. Dashed lines are guides to the eye.

aspect is most obvious from the green and blue data points in Fig. 5-7 (a), which belong to the spherical NC #R1 and the DiRs with a core size of 3.2 nm. Although their shell shapes are very different, the measured spin relaxation rates are almost equal.

The sensitivity of the spin relaxation rate on temperature, as could be observed from Fig. 5-6 (b), indicates an acoustic phonon mediated process. Due to the increasing number of available phonons with increasing temperature spin relaxation becomes more efficient. However, in contrast to bulk material, the phonon density of states in NCs is modified by confinement, as has been studied in several experiments. [82–84] This leads to the already mentioned acoustic phonon bottleneck, [85] meaning that low-energy, long-wavelength acoustic phonons are suppressed in nanometer-sized structures due to their limited size. Because of the similar elastic properties of CdSe and CdS it is expected, that the phonon confinement is different in DiR compared to spherical NCs. Namely, the lower confinement along the rod axis presumably gives rise to longitudinal modes in addition to the torsional and spheroidal eigenmodes observed in spherical structures. [84] This raises the question, whether the phonon modes, which couple to excitons, are considerably different in DiRs compared to spherical NCs. In this regard from the data presented in Fig. 5-7 (a) it can be inferred, that the shell shape does not significantly affect the number of phonon modes, which interact with the exciton, given that acoustic phonons play a crucial role regarding the efficiency of the spin relaxation mechanism. This conclusion is in agreement with the results of a FLN experiment on DiR in high magnetic fields. [102] Therein the authors found, that the acoustic phonon modes of DiRs involved in exciton recombination in the presence of a magnetic field are similar to those of confined modes in an isolated spherical NC.

The magnetic field dependence of the spin relaxation rate is most likely related to the acoustic phonon bottleneck. For all studied samples the evolution of τ_s with B can be divided into two regimes. In the low field regime the relaxation rate follows a cubic dependence, whereas at higher fields the dependence becomes linear. From a different perspective one can argue, that at higher fields the slope of the spin relaxation rate dependence is increased compared to lower fields. The onset of this increase occurs at $B = 8 - 10$ T. Assuming an average angle between the magnetic field and the crystal c-axis of 45° and taking $g_{ex} = 2.7$ for the dark exciton g factor, [120] the corresponding Zeeman splitting calculates as $\Delta E \approx 1$ meV. This energy matches roughly the vibrational

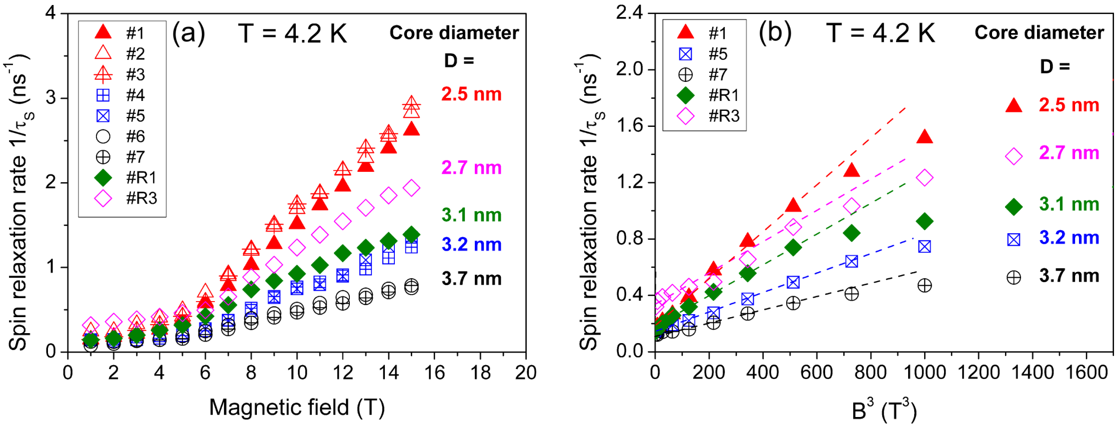

Figure 5-7: (a) Magnetic field dependence of the spin relaxation rate $1/\tau_s$ for the DiR samples #1-#7 and spherical core/shell samples #R1 and #R3 at $T = 4.2$ K. (b) Magnetic field dependence of the spin relaxation rate $1/\tau_s$ for selected samples at low magnetic fields. Dashed lines are guides to the eye.

energy of the $l = 2$ spheroidal mode of a CdSe sphere with a diameter of 5 nm estimated according to Lamb's theory. [84] The observed change in the magnetic field dependence could result from the onset of these spheroidal vibrations at magnetic fields around $8 - 10$ T. Although the core diameter of the samples studied here is considerably smaller than 5 nm, due to the very similar elastic properties of CdSe and CdS, the overall size of the shell might be relevant in this regard. [103] According to the Lamb-theory, the energy of the spheroidal modes scales as $E \propto 1/D$, where D is the sphere diameter. Therefore it can be expected, that for larger NCs the onset of the linear magnetic field dependence should occur at lower fields. However, such a trend cannot be verified from the experimental results. This can originate from the size dispersion inherent to NC ensembles, which can "blur" the transition from one regime into the other. Nevertheless, the interpretation above is in accordance with the findings of a recent magneto-optical experiment on trions in CdSe/CdS core/shell NCs, where spin relaxation was found to be completely inhibited for small Zeeman-splittings, as a result of the acoustic phonon confinement. [85]

The red data points in Fig. 5-7 (a), which belong to DiR samples with a core diameter 2.5 nm, indicate, that the shell thickness could have a small effect on the spin relaxation rate. One can observe, that with increasing shell thickness the spin relaxation rate decreases slightly at a given magnetic field. In order to investigate this effect more systematically, a set of spherical NCs #R2-#R5, which have similar core sizes but different shell thicknesses, was studied. Sample #R2 consists of bare CdSe cores. The corresponding magnetic field dependences of the spin relaxation rates are shown in Fig. 5-8 (b). The most striking observation is, that the rate of exciton spin relaxation in the bare core sample #R2 is approximately one order of magnitude higher (the spin relaxation time is as short as $\tau_s \approx 300$ ps already at low magnetic fields) compared to core/shell samples ($\tau_s \approx 3$ ns at low fields). The addition of a CdS shell leads to a vast drop of the spin relaxation rate, but further increase of the shell thickness from 0.8 nm up to 5.3 nm reduces the rate only slightly. This weak dependence on shell thickness was also observed in a magnetic field experiment on spherical core/shell ensembles reported in Ref. [103]. Here, only slight changes in the spin relaxation rate for shell thicknesses below 5 nm were observed, whereas for even thicker shells the decrease got more pro-

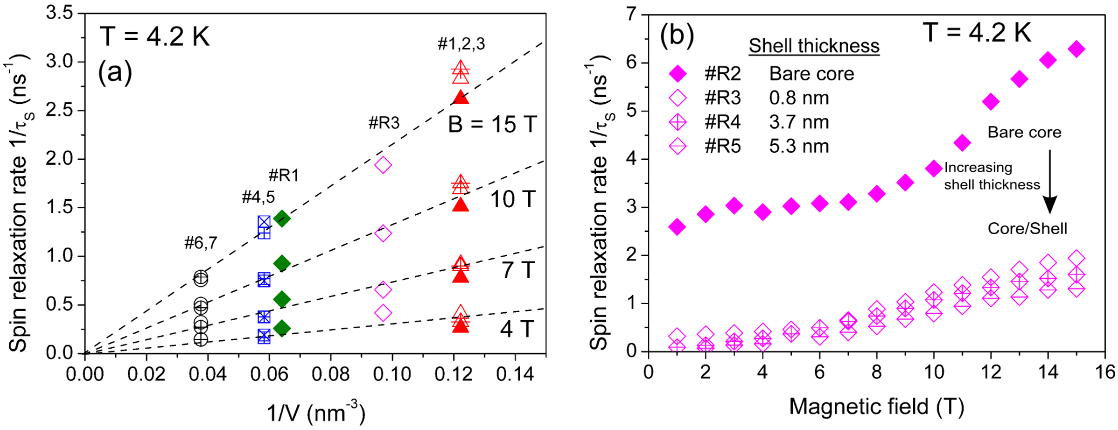

Figure 5-8: (a) Dependence of the spin relaxation rate $1/\tau_s$ on core volume V at different magnetic fields for the samples also shown in Fig. 5-7 (a). Dashed lines are guides to the eye. (b) Magnetic field dependence of the spin relaxation rate $1/\tau_s$ for spherical NCs #R2-#R5 with different shell thicknesses and similar core size.

nounced. This was attributed to the onset of NC charging at shell thicknesses around 5 nm, leading to very different spin dynamics of negatively charged excitons (trions) compared to neutral excitons, as they are studied here.

Figure 5-8 (a) shows the spin relaxation rate as a function of core volume for the samples previously shown in Fig. 5-7 (a). Interestingly, the relaxation rate seems to be inversely proportional to the CdSe core volume. This observation, along with the surprisingly fast spin relaxation for bare cores and the weak dependence of τ_s on the shell thickness, substantiates the importance of the NC surface and the CdSe/CdS interface in core/shell structures regarding the spin relaxation mechanism. The results indicate, that the spin relaxation rate depends on the strength of interaction of the exciton with the surface or the interface. As the volume of the core increases, the surface to volume ratio of the core decreases and the interaction of excitons with the bare core surface or the core/shell interface is progressively reduced.

As was shown in chapter 4, due to the high valence band offset between CdS and CdSe the hole is confined to the core, whereas the electron wavefunction, due to a smaller conduction band offset, can leak into the shell to a certain degree. On the one hand this could explain the weak dependence of the spin relaxation rate on the shell thickness, since the overall surface in core/shell NCs is experienced only by the electron. On the other hand, this aspect and the strong core size dependence of τ_s indicate, that the hole might be the more relevant particle regarding the exciton spin relaxation process.

Additionally, it was demonstrated in chapter 4, that a change of the core volume or the shell thickness of the NC results in a modification of the eh-exchange interaction due to the modified carrier wavefunction overlap. Thereby the exciton fine structure, notably the bright-dark energy splitting, is affected. This influences the mixing of bright and dark exciton states by the perpendicular component of the external magnetic field. Nevertheless, considering the wide range of dark-bright energy splittings, which for the DiR samples investigated here vary approximately between 2 and 5 meV and considering the small change of the spin relaxation rate with shell thickness, it is likely that the impact of changes in the exciton fine structure due to the varying eh-exchange interaction on the spin dynamics is small.

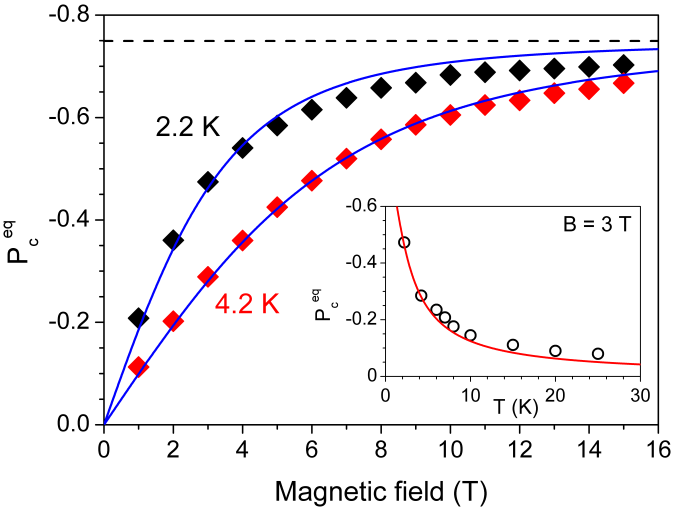

Figure 5-9: Magnetic field dependence of P_c^{eq} for sample #R1 at $T = 2.2$ K and 4.2 K. The black dashed line indicates the theoretical limit of $P_c^{\mathrm{eq}} = -0.75$ for an ensemble of randomly oriented NCs. The blue solid lines are fits of Eq.(5.5) to the experimental values, assuming $f_{\mathrm{or}}(x) = 1$. The inset shows the temperature dependence of P_c^{eq} at $B = 3$ T. The red line is calculated taking the exciton g factor determined from the fit of the magnetic field dependence.

The apparent relevance of the core/shell interface for spin relaxation is interesting, since its influence on optical properties of NCs is yet poorly understood but undoubtedly important. For example, it was shown in Ref. [143], that a "smooth transition" from the core to the shell material favours non-blinking emission of NCs.

The interface or surface of semiconductor nanostructures is the focus of the theoretical studies of Knipp and Reinecke as well as related work. Therein, the interaction between charge carriers and acoustic phonons is investigated. [144–147] The authors propose electron-phonon coupling via the so-called "ripple mechanism", for which the coupling results from the spatial dependence of the electron effective mass and its potential energy. The coupling occurs due to the motion of the interface between the nanostructure and the surrounding medium or between different regions in a heteronanostructure. Notably, the authors predict this effect to be dominant over the common deformation potential coupling for small NCs, as they are studied here. Moreover, they expect the phonon scattering rate to be strongly dependent on the nanostructure size with higher scattering rates for smaller NCs. As was discussed for epitaxial grown III-V quantum dots, the ripple mechanism also strongly affects the electron [148] and hole [149] spin relaxation in magnetic field. However, the coupling between excitons and phonons in colloidal NCs is still poorly understood, although it obviously plays an important role for energy and spin relaxation as well as the recombination of excitons. The aforementioned studies stress the relevance of the interface between the nanostructure and its surrounding medium regarding exciton-phonon coupling as well as spin relaxation. The experimental results discussed here point in the same direction.

Equilibrium circular polarization

In this section it is discussed how the equilibrium DCP P_c^{eq}, which is derived from the fit of the TRDCP curves with Eq.(5.3), depends on magnetic field, temperature and

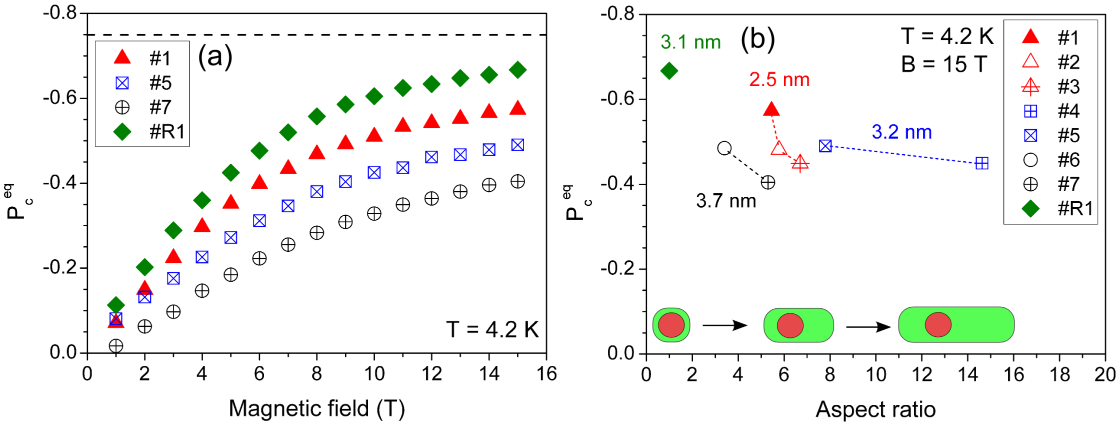

Figure 5-10: (a) Magnetic field dependences of P_c^{eq} for samples of different core size at $T = 4.2$ K. The black dashed line indicates the theoretical limit of $P_c^{\mathrm{eq}} = -0.75$ for an ensemble of randomly oriented NCs. (b) P_c^{eq} for the DiR samples #1-#7 and the spherical core/shell sample #R1 at $T = 4.2$ K and $B = 15$ T as a function of aspect ratio. The inset schematically illustrates the corresponding change of NC shape. The dashed lines are guides to the eye.

NC shape. In Fig. 5-9 the magnetic field dependence of P_c^{eq} is shown for the spherical core/shell sample #R1 at $T = 2.2$ K and 4.2 K. At low magnetic fields P_c^{eq} exhibits a steep increase, whereas at high magnetic fields it saturates. The blue solid lines are fits of the experimental data with Eq. (5.5), assuming a randomly orientated NC ensemble, i.e. $f_{\mathrm{or}}(x) = 1$. In this case, the theoretical limit for P_c^{eq} is expected to be -0.75, which is indicated as a black dashed line. The fit yields an exciton g factor of $g_{ex} = 2.5$, which is close to reported experimental values for the dark exciton g factor of $g_{ex} = 2.8$ in a FLN experiment [102] and $g_{ex} = 2.7$ in a single-NC PL experiment, [120] although values of $g_{ex} = 2.4 - 2.6$ have been also reported for the bright exciton. [100] At a given magnetic field P_c^{eq} decreases with increasing temperature, as can be observed from the inset of Fig. 5-9. An increase of the temperature from 2.2 K up to 25 K leads to a drop of $|P_c^{\mathrm{eq}}|$ from approximately 0.5 down to 0.1. This is a result of the thermal population of the upper lying Zeeman-sublevel, corresponding to a reduced exciton spin polarization. The experimental data can be well fitted with Eq.(5.5) using $g_{ex} = 2.5$, as can be seen from the plotted red line.

In Fig. 5-10 (a) P_c^{eq} is plotted as a function of B for DiR samples #1, #5 and #7 along with the spherical core/shell sample #R1 at $T = 4.2$ K. Apparently, the evolution of P_c^{eq} with B is quite different for samples of different shape and different core size and a lower polarization degree is always found for DiRs compared to the spherical NC. The plotted dependences differ in their slope at low magnetic fields and also seem to have very different saturation levels, although saturation is not fully reached within the magnetic field range of the experiment. A varying slope at low magnetic fields could result from differences in the exciton g factor, which is mainly determined by the variation of the electron g factor. In the studied structures holes are strongly localized in the core and the hole g factor in general can be estimated using the expression developed for a potential of spherical symmetry as $g_h = -1.09$, see Refs. [28, 150]. It is independent of the core size and is therefore expected to be the same for all samples. In contrast, the electron g factor is subject to an interplay of two effects. On the one hand, the increase of the CdS shell leads to a decrease of the electron quantum confinement energy and thus to a decrease of the electron g factor, because of its energy dependence. [151] On the other hand, the leakage of the electron wave function into the CdS shell leads to a contribution from the CdS g factor. For a CdSe NC of core diameter $D = 3$ nm, the electron g factor is expected to be approximately $g_e = 1.5$. [75] In CdS it is expected to be close to 2, and thus the electron leakage into the shell leads to an increase of the electron g factor. [75] These two effects may partly compensate each other.

Nevertheless, differences in g factor would not affect the saturation level of P_c^{eq} at high magnetic fields. Although the saturation is not reached within the magnetic field range of the experiment, the data shown in Fig. 5-10 (a) indicates saturation of P_c^{eq} at different levels. In Fig. 5-10 (b) $P_c^{\mathrm{eq}}(B = 15\text{ T})$ is shown for all DiR samples as well as sample #R1 as a function of the aspect ratio (the ratio of length to width of the NC shell given in Table 3-3). The values of $P_c^{\mathrm{eq}}(B = 15\text{ T})$ vary between -0.66 for the spherical sample #R1 and -0.4 for DiR sample #7. For a given core size, it is found, that P_c^{eq} is always lower for the NC with higher aspect ratio. This observation indicates, that the differences in P_c^{eq} could be related to the geometry of the NC shell. As discussed in Ref. [152], the circular polarization of the PL in magnetic field can be reduced by an optical anisotropy, resulting from the linear polarization of individual emitters. Typical values for the PL linear polarization along the anisotropic c-axis of individual DiRs were reported to be close to 75% at room temperature. [31, 153, 154] Values measured at low temperatures are still missing. The high linear polarization degree of the PL observed for single DiR NCs at room temperatures may result partly from the exciton fine structure and partly from the dielectric enhancement effect (see section 2.4.2), [47, 155] both of which are dependent on the NC geometry. The following section provides a detailed discussion of these effects. It is analyzed how the exciton fine structure and the dielectric enhancement effect influence the circular and linear polarization of the PL in magnetic field for NCs with various shapes at low temperatures.

5.4 Theoretical considerations

The mathematical derivation of the theoretical model presented in the following was accomplished by A.V. Rodina.

Derivation of the model

It is assumed, that the lowest exciton state is the dark exciton with momentum projection $|F| = 2$ on the hexagonal c-axis (which is also the rod axis in DiR NCs). Figure 5-11 (a) shows a sketch of the exciton energy levels in zero and nonzero magnetic field. Only the ground state $F = \pm 2$ and the bright exciton states $F = \pm 1^{L,U}$ and $F = 0^U$ are shown. The energy splitting, which is typically found between 1^L and 1^U states, [28] is neglected here for the sake of clarity. Further it is assumed, that the dark exciton $|F| = 2$ can recombine only via coupling with the bright exciton states. Notably, wether the coupling occurs with the $F = \pm 1^{L,U}$ or the $F = 0^U$ state has important consequences for the orientation of the transition dipole moments. Coupling with the $|F| = 1^{L,U}$ states leads to recombination, which is polarized transverse to the c-axis. [156] The respective recombination rate is denoted by Γ_{21}^0 at zero and Γ_{21} at nonzero magnetic field. Importantly, the coupling with $|F| = 1$ states can be enhanced by magnetic fields oriented perpendicular to the c-axis. [28, 43] For this reason, Γ_{21} depends on the angle

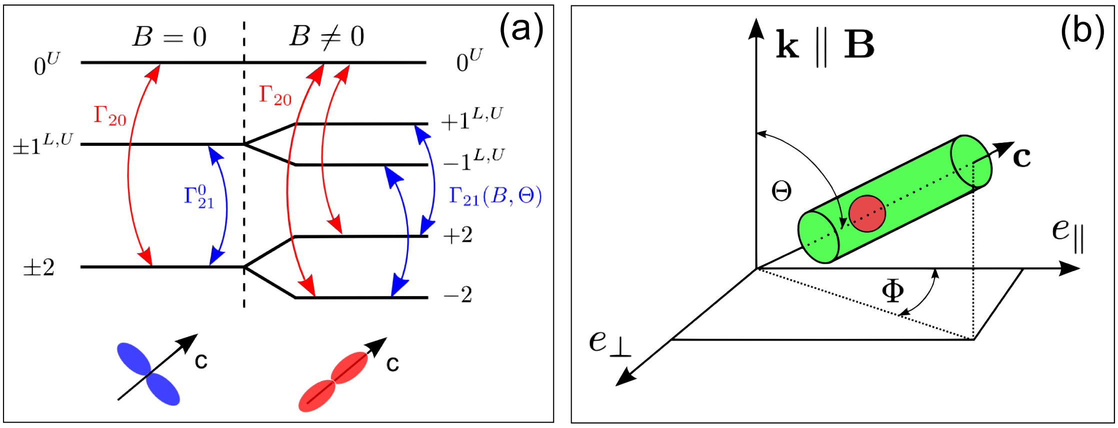

Figure 5-11: (a) Schematic of the band edge exciton energy levels in zero and non-zero magnetic fields. Only the dark exciton ground state with $F = \pm 2$ and the bright exciton states $F = \pm 1^{L,U}$ and $F = 0^U$ are shown. The red and blue arrows show the coupling pathways, which may enable dark exciton radiative recombination. The sketches in the bottom illustrate the respective orientation of the transition dipole for the different coupling pathways with respect to the crystal c-axis. (b) Schematic of the experimental geometry for measuring circular and linear polarization of the PL from a DiR or spherical NC with anisotropy c-axis. Note, that in the ensemble the angles Θ and Φ, which determine the direction of $\mathbf{c}$ with respect to the light vector $\mathbf{k}$ and the linear polarizer axis $\mathbf{e}_\parallel$, are uniformly distributed.

Θ between the magnetic field direction and the c-axis. In contrast, coupling of the dark exciton $|F| = 2$ with the bright $F = 0^U$ state leads to recombination polarized parallel to the c-axis and the respective recombination rate, which is denoted by Γ_{20}, is independent of the magnetic field. The experimental geometry assumed in the following is illustrated in Fig. 5-11 (b).

It should be noted that the usual assumption, which leads to Eq. (5.5) describing the magnetic field dependence of P_c^{eq}, is, that the dark exciton recombines due to coupling with the $|F| = 1^{L,U}$ bright states [28, 43] characterized by Γ_{21} and thus has the same polarization properties as the $|F| = 1$ exciton. In this case, the dipole momentum acquired by the dark exciton is oriented transverse to the c-axis, as illustrated in the left bottom scheme in Fig. 5-11 (a). The new aspect here is the assumption, that the dark exciton can recombine with the properties of the $F = 0$ bright exciton as well. This coupling between the $|F| = 2$ dark exciton and the $F = 0$ state described by Γ_{20} could be mediated by $l = 2, m = \pm 2$ acoustic phonons. [73, 157] It could be also caused by a shape anisotropy in the plane perpendicular to the c-axis, which mixes the valence band states [98] but more importantly leads to an anisotropy of the electron wavefunction and thus to an anisotropy of the Coulomb interaction of the exciton.

In DiRs the recombination polarized along the c-axis can be additionally enhanced by the dielectric enhancement effect, which was described in section 2.4.2. The enhancement factor R_e is described by Eq.(2.43). Essentially, the rod shaped shell of DiRs acts as a linear polarizer, which affects the absorption as well as the emission of light. A frequency dependence of R_e is neglected here and the effect is assumed to be similar for excitation and emission.

The dielectric enhancement effect can lead to the selective excitation of DiR NCs oriented perpendicular to the magnetic field (the light propagation direction). According to Ref. [46], the probability for a NC to be excited by linear polarized light is

$1 + (R_e - 1)(\mathbf{e} \cdot \mathbf{c})^2$, where $\mathbf{e}$ is the light polarization vector. For the geometry shown in Fig. 5-11 (b) and light polarized along the $e_{\|}$ direction one can write $(\mathbf{e} \cdot \mathbf{c})^2 = \sin^2\Theta\cos^2\Phi$. By averaging over all polarizations in the plane $(e_{\|}, e_{\perp})$ the probability for excitation of a NC, oriented at an angle Θ with respect to the light propagation direction, by unpolarized light follows as

$$f_{\text{exc}}(x) = 1 + 0.5(R_e - 1)(1 - x^2)\,, \tag{5.6}$$

where $x = \cos\Theta$. Taking into account the selective excitation effect, the general expression Eq. (5.4), which describes the DCP for an ensemble of DiR NCs, transforms into

$$P_c(B) = \frac{\int_0^1 [I_{\sigma+}(x) - I_{\sigma-}(x)] f_{\text{or}}(x) f_{\text{exc}}(x) dx}{\int_0^1 [I_{\sigma+}(x) - I_{\sigma-}(x)] f_{\text{or}}(x) f_{\text{exc}}(x) dx}. \tag{5.7}$$

In the following only the case of randomly oriented NCs, i.e. $f_{\text{or}}(x) \equiv 1$, is considered. When the selective excitation effect is taken into account and the Γ_{20} rate is neglected, Eq.(5.5) for the magnetic field dependence of the DCP remains unchanged with the function $f_{\text{or}}(x)$ replaced by $f_{\text{exc}}(x)$.

When the activation of the dark exciton by a magnetic field applied perpendicular to the c-axis, which leads to a magnetic field and angle dependence of the rate $\Gamma_{21}(B, x)$, is taken into account, Eq. (5.5) transforms into

$$P_c^{\text{eq}}(B) = \frac{\int_0^1 \gamma(B,x) 2x \tanh(\Delta E/2k_B T) f_{\text{exc}}(x) dx}{\int_0^1 \gamma(B,x)(1 + x^2) f_{\text{exc}}(x) dx}\,, \tag{5.8}$$

where the factor $\gamma(B, x) = \Gamma_{21}(B, x)/\Gamma_{21}^0$ is a measure of the strength of the magnetic-field-induced mixing.

In general, the angular and magnetic field dependence of $\Gamma_{21}(B, x)$ can vary, depending on the relation between $g_{ex}\mu_B B^{\text{sat}}$ and the bright-dark exciton splitting ΔE_{bd}. B^{sat} is the magnetic field where the DCP is saturated. In the case $g_{ex}\mu_B B^{\text{sat}} \ll \Delta E_{bd}$ one can write $\Gamma_{21}(x) = \Gamma_{21}^0[1 + p(1 - x^2)]$, where the parameter p describes the dependence on B and $p \propto B^2$ in this case. In the opposite case $g_{ex}\mu_B B^{\text{sat}} \gg \Delta E_{bd}$ the parameter p becomes a constant being independent of the magnetic field and $\Gamma_{21}(x) = \Gamma_{21}^0[1+p(1-x)]$. [28,158] In the following only the first case is considered, which means that the Zeeman-splitting is assumed to be small compared to the bright-dark energy splitting.

Next, the coupling of the $|F| = 2$ states to the state $F = 0^U$ is also included. The transitions polarized along the c-axis contribute equally to $I_{\sigma+}(x)$ and $I_{\sigma-}(x)$ with the probability $\Gamma_{20} R_e \sin^2\Theta$. With account of these transitions the following expression for an ensemble of randomly oriented DiR NCs is obtained:

$$P_c^{\text{eq}}(B) = \frac{\int_0^1 \gamma(B,x) 2x \tanh(\Delta E/2k_B T) f_{\text{exc}}(x) dx}{\int_0^1 \left[\gamma(B,x)(1 + x^2) + r(1 - x^2)\right] f_{\text{exc}}(x) dx}\,, \tag{5.9}$$

where $r = R_e\Gamma_{20}/\Gamma_{21}^0$. Obviously, on the one hand the coupling to the $F = 0^U$ state lowers P_c^{eq} at a given magnetic field. On the other hand it leads to a higher degree of linear polarization for the individual NC, as will be discussed below.

The degree of linear polarization, which can be found for an individual NC, is $\rho_l = (I_{\|} - I_{\perp})/(I_{\|} + I_{\perp})$. Here $I_{\|}(I_{\perp})$ is the intensity of light polarized along the $e_{\|}(e_{\perp})$

direction. It can be shown that

$$\rho_l(x,\Phi) = \frac{(1-x^2)(R_e\Gamma_{20} - \Gamma_{21})\cos(2\Phi)}{(1+x^2)\Gamma_{21} + (1-x^2)R_e\Gamma_{20}}\,. \tag{5.10}$$

One can see, that after averaging over all angles of a randomly oriented ensemble of DiR NCs, the overall linear polarization $P_l = \int_0^1 dx \int_0^{2\pi} \rho_l(x,\Phi) d\Phi$ is zero. Still it can be nonzero for the individual DiR NC, with maximum contribution for rods oriented with $\Phi = 0°$ and $\Theta = 90°$ (i.e. $x = 0$). In the following only the maximum linear polarization $\rho_l^{\max}$, corresponding to this particular geometry, is considered. For zero magnetic field it is

$$\rho_{l,0}^{\max} = \frac{r-1}{r+1}\,. \tag{5.11}$$

For the case $r < 1$, which corresponds to a higher coupling rate to the ± 1 states Γ_{21}^0 in comparison to the dielectrically enhanced rate $R_e\Gamma_{20}$, $\rho_{l,0}^{\max}$ has negative values. This corresponds to the situation, in which the light is preferentially polarized perpendicular to the c-axis. In magnetic fields the situation is more complex, because of the enhancement of the coupling to the $F = \pm 1$ states. At high fields, at which the circular polarization degree is saturated ($B = B^{\mathrm{sat}}$), the maximum linear polarization can be written as

$$\rho_l^{\max}(B^{\mathrm{sat}}) = \frac{r - (1+p^{\mathrm{sat}})}{r + (1+p^{\mathrm{sat}})}\,. \tag{5.12}$$

Here, $(1+p^{\mathrm{sat}}) = \gamma(B^{\mathrm{sat}}, x=0) = \Gamma_{21}(B^{\mathrm{sat}}, x=0)/\Gamma_{21}^0$. It is a measure for the increase of Γ_{21} at $B = B^{\mathrm{sat}}$ for NCs oriented perpendicular to the magnetic field.

So far, the equations for the circular polarization of the DiR ensemble and the linear polarization of individual DiRs in magnetic field are derived. In the following section the correlation between the linear polarization of individual DiRs and the ensemble DCP is analyzed in more detail and the theory is compared to the experimental results.

Discussion

In the following, it is analyzed, how the saturation level of P_c^{eq} (i.e. P_c^{sat}) is affected by the different mechanisms, which were introduced in the previous section. To this end, the discussion is seperated into two parts. Firstly, the effect of selective excitation and the newly introduced coupling to the $F = 0^U$ state are analyzed without account of magnetic field activation of dark exciton radiative recombination, i.e. $p = p^{\mathrm{sat}} = 0$. Later on, the additional effect of $p \neq 0$ is discussed.

In Fig. 5-12 (a) the magnetic field dependences of P_c^{eq} is shown for the DiR samples #1,#2,#3 and the spherical core/shell sample #R1 at $T = 4.2$ K. Apparently, the dependences differ from each other and P_c^{eq} seems to saturate at different values. The dashed and dotted lines are calculations done with Eq.(5.9). The parameters used are $g_{ex} = 2.7$, $R_e = 3.2, 3.3, 3.4, 1$ and $\Gamma_{20}/\Gamma_{21}^0 = 0.03, 0.13, 0.19, 0.02$ for samples #1,#2,#3 and #R1 respectively. It is assumed, that the ratio between the coupling of the dark exciton to the $F = 0$ state and the coupling to the $F = \pm 1$ states are different for the various NCs. The enhancement factor values R_e were calculated according to Eq.(2.43), where the dielectric constants where taken to be $\kappa_m = 2$ and $\kappa_s = 6$ for the surrounding medium and the NC, respectively. The values of the dielectric constants are similar to

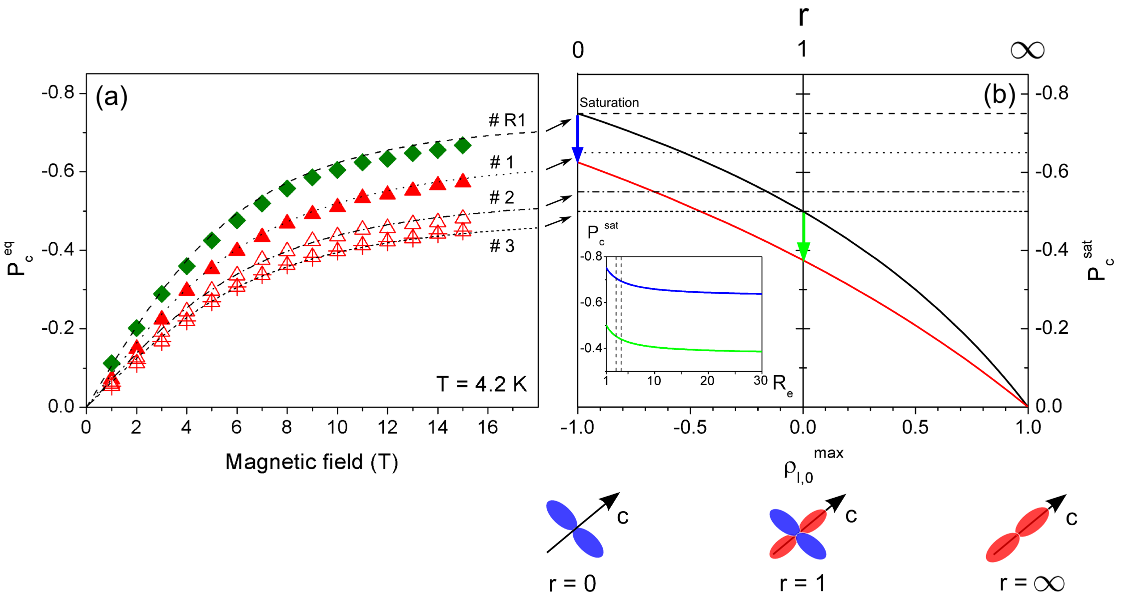

Figure 5-12: (a) Magnetic field dependences of P_c^{eq} for the DiR samples #1, #2, #3 and the spherical core/shell sample #R1 at $T = 4.2$ K. The dashed and dotted lines are calculated according to Eq.(5.9). (b) Saturated values of the circular polarization in high magnetic fields P_c^{sat} for an ensemble of arbitrary oriented NCs vs. maximal linear polarization of individual NCs in zero magnetic field $\rho_{l,0}^{\text{max}}$. Orientation of the transition dipoles with respect to the NC c-axis is illustrated in the sketches below. The black curve is calculated without considering the effect of selective excitation (i.e. $R_e = 1$) and the red curve is calculated taking $R_e = 1000$, which corresponds to an extremely strong effect of selective excitation. The inset shows P_c^{sat} as a function of R_e for $\rho_{l,0}^{\text{max}} = -1$ (blue curve) and $\rho_{l,0}^{\text{max}} = 0$ (green curve). The dashed lines in the inset mark the range of calculated enhancement factors for the investigated samples according to Eq.(2.43). The dashed and dotted lines in the main plot of the right panel are the saturation values derived from the corresponding calculated curves in the left panel. All of these calculations were done neglecting the effect of magnetic field activation of the dark exciton radiative recombination.

those, assumed in Ref. [47]. Apparently, the evolution of the experimentally determined P_c^{eq} can be well reproduced by the model derived in the previous section.

The correlation between the linear polarization of an individual emitter and the resulting ensemble polarization is highlighted in Fig. 5-12 (b). It shows a plot of the saturated ensemble polarization P_c^{sat} (with randomly oriented DiRs) as a function of the maximal linear polarization of individual DiRs at zero magnetic field $\rho_{l,0}^{\text{max}}$. At this point, the magnetic field activation of the dark exciton is still neglected (i.e. $p^{\text{sat}} = 0$). Horizontal lines correspond to the saturated values of P_c^{eq}, which were derived from the corresponding calculated curves in the left panel (the black arrows indicate the saturation). The red and black curves are the theoretically predicted dependences of P_c^{sat} on $\rho_{l,0}^{\text{max}}$ with and without considering the effect of selective excitation, respectively. Obviously, the selective excitation effect leads to an additional decrease of the saturated polarization value. The dependence of P_c^{sat} on R_e due to selective excitation is shown in the inset for $\rho_{l,0}^{\text{max}} = -1$ and $\rho_{l,0}^{\text{max}} = 0$ (see the corresponding blue and green arrows). The dashed lines indicate the range of enhancement factors calculated for the DiRs investigated here. Clearly, with increase of the DiR aspect ratio resulting in a larger dielectric enhancement factor, the DCP is progressively reduced. Notably, however, even in the case of an extremely strong dielectric enhancement effect, the saturation value is not

DiR NCs

#	Aspect ratio L/W	P_c^{sat}	g_{ex}	R_e	r
1	5.5	-0.65	2.7	3.2	0.03
2	5.8	-0.55	2.7	3.3	0.13
3	6.7	-0.49	2.7	3.4	0.19
4	14.6	-0.63	1.4	3.8	0.05
5	7.3	-0.60	2.0	3.5	0.08
6	3.4	-0.57	1.4	2.8	0.16
7	5.3	-0.63	1.5	3.2	0.06

Spherical NCs

#	Aspect ratio L/W	P_c^{sat}	g_{ex}	R_e	r
R1	1	-0.74	2.7	1	0.02
R2	1	-0.67	1.2	1	0.25
R3	1	-0.74	2.4	1	0.02
R4	1	-0.67	2.8	1	0.25
R5	1	-0.60	0.9	1	0.5

Table 5-1: Parameters of the studied CdSe/CdS DiR and spherical samples. P_c^{sat} - saturation level of the DCP, estimated by fitting Eq. (5.9) to the experimental data. g_{ex} - exciton g factor, R_e - enhancement factor, and $r = R_e\Gamma_{20}/\Gamma_{21}^0$ - parameter defined in Eq.(5.9).

lowered by more than approximately 12%. In contrast, as can be observed from the red and black curves, the increase of the r value [i.e. the ratio of the coupling rates, see upper scale in Fig. 5-12 (b)] and the resulting maximal linear polarization of individual DiRs at zero magnetic field leads to a decrease of the saturation value of the circular polarization in the ensemble, which can vary between -0.75 and 0. Within this approximation from the intersection of the dashed and dotted lines (the theoretically derived saturation values) with the black curve, the maximal linear polarization of the individual rod at zero field is predicted to be negative for all DiRs considered here ($\rho_{l,0}^{max} < 0$), which means the light emitted from these DiRs is linearly polarized predominantly transverse to the c-axis at low temperatures, see sketches below Fig. 5-12 (b).

Table 5-1 summarizes theoretically estimated parameters, obtained by fitting Eq.(5.9) to the experimental data, as well as calculated enhancement factors for all studied DiR and spherical samples. One can see, that the model can account for strongly varying saturated DCPs P_c^{sat} at high magnetic fields, if the coupling of the dark exciton to the $F = 0^U$ state is taken into account (i.e. $r \neq 0$). Notably, however, the exciton g factors derived by the fitting vary considerably for the samples investigated here. This could be related to variations of the electron g factor, resulting from the leakage of the electron wavefunction into the shell, as discussed in section 5.3, although no systematic trend can be observed for the samples listed in Table 5-1 in this regard. The elucidation of the origin of these differences requires additional experimental studies.

Next, the influence of the activation of the dark exciton by the magnetic field on the polarization properties of the DiR NCs is discussed in more detail. Firstly, the effect on the linear polarization of individual rods is considered. In Fig. 5-13 (a) the maximal

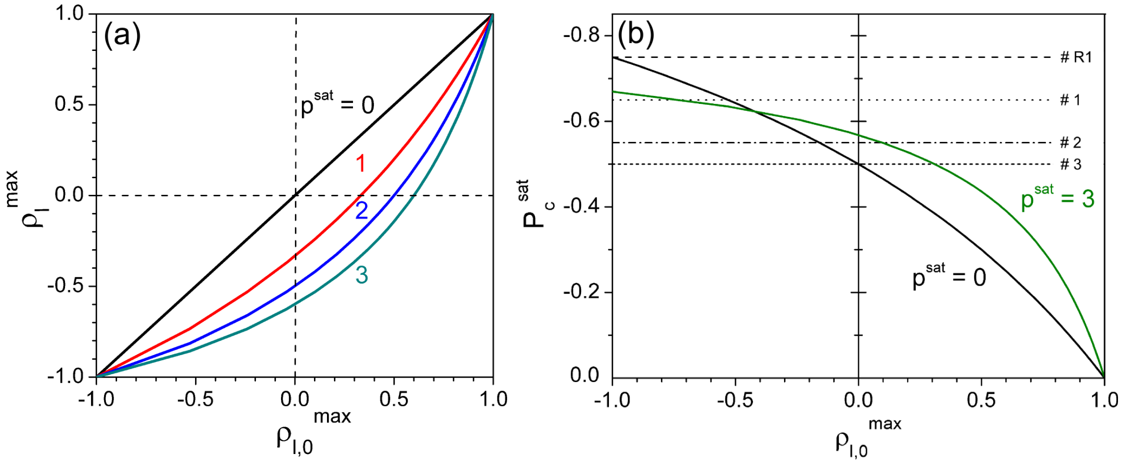

Figure 5-13: (a) Maximal values of individual NC linear polarization in high magnetic field $\rho_l^{\max}$ vs. maximal values of the linear polarization in zero magnetic field $\rho_{l,0}^{\max}$ for $p^{\mathrm{sat}} = 0, 1, 2, 3$. (b) Saturated values of the circular polarization degree in high magnetic fields P_c^{sat} for an ensemble of arbitrary oriented NCs vs. maximal linear polarization values of individual NCs in zero magnetic field $\rho_{l,0}^{\max}$, taking into account the effect of magnetic field activation of dark exciton recombination ($p^{\mathrm{sat}} = 0$ for the black curve and $p^{\mathrm{sat}} = 3$ for the green curve). Calculations are done without considering the effect of selective excitation ($R_e = 1$).

linear polarization of individual rods at $B = B^{\mathrm{sat}}$ is plotted against the maximal linear polarization at zero magnetic field for different values of p^{sat}. For reminding the reader, the parameter p was assumed to be dependent on the magnetic field. Since the linear polarization here is considered either at $B = 0$ or $B = B^{\mathrm{sat}}$, $p(B^{\mathrm{sat}}) \equiv p^{\mathrm{sat}} = \gamma(B^{\mathrm{sat}}, 0) - 1$ is used as a modeling parameter. It is defined by the coupling of the $F = \pm 2$ states to the $F = \pm 1$ states at high and zero magnetic fields and for a NC, whose hexagonal axis is oriented perpendicular to the magnetic field. The magnetic field enhances the coupling to $F = \pm 1$ states, therefore, the amount of transitions polarized transverse to the c-axis increases with increasing magnetic field. This effect can be observed from the curves shown in Fig. 5-13 (a). If $p^{\mathrm{sat}} = 0$ the maximal linear polarization is independent of the magnetic field, i.e. $\rho_l^{\max} = \rho_{l,0}^{\max}$. However, with increasing p^{sat} the linear polarization in high magnetic fields shifts progressively to negative values, which means the transitions polarized transverse to the c-axis are enhanced. This can lead to the case, where the PL is polarized parallel to the c-axis at zero magnetic field, whereas it is polarized transverse to it at high fields.

The parameter p^{sat} is unknown for the samples investigated in this study but could be determined by measuring the linear polarization of an individual DiR at zero and at very high magnetic fields. Its order of magnitude can be estimated by considering the shortening of the PL decay, which is typically observed in high magnetic field experiments. In Ref. [120], which reports on magneto-optical PL measurements on single spherical CdSe/ZnS core/shell NCs, the authors observe a shortening of the PL decay from approximately 180 ns to 50 ns for a NC oriented at $\Theta = 75°$ with respect to the magnetic field. This corresponds to a ratio of 3.6 for the recombination rates and therefore p^{sat} is equal to 2.6 in this case. An even lower decay time can be expected for larger Θ, thus the upper limit of p^{sat} is expected to be around 3. This approximation holds only, if one assumes, that there is no contribution from the $F = 0^U$ states in the PL, which can reasonably be assumed for NCs, where the saturation value of the DCP in a randomly oriented ensemble approaches -0.75 at high magnetic fields.

In the following it is analyzed, how the increased transverse linear polarization due to magnetic field activation of dark exciton radiative recombination affects the circular polarization of the ensemble PL. In Fig. 5-13 (b) the saturation value of the ensemble circular polarization at $B = B^{\mathrm{sat}}$ is plotted as a function of the individual NC linear polarization at $B = 0$ for $p^{\mathrm{sat}} = 0$ (black curve) and $p^{\mathrm{sat}} = 3$ (green curve). The selective excitation effect is not considered here (i.e. $R_e = 1$). The horizontal lines are similar to those in Fig. 5-12 (b) and correspond to the predicted saturation levels for the samples shown in Fig. 5-12 (a). They are plotted here for better comparability. It is worth noting, that when the effect of the angular dependence of the dark exciton recombination rate is taken into account, the predicted level of P_c^{sat}, derived from fitting the magnetic field dependences $P_c^{\mathrm{eq}}(B)$, will be lower for each sample. One can see that in the region of small values of r the effect of the dark exciton activation by the magnetic field leads to a decrease of P_c^{sat} averaged over the ensemble. This is because the magnetic field activation depends on the angle and the resulting transitions become stronger for the NCs oriented perpendicular to the c-axis, for which the Zeeman splitting is smaller. For larger r, however, the general increase of the Γ_{21} transition becomes more important than its angular dependence and therefore P_c^{sat} increases. As a result, from the intersection of the dashed and dotted lines with the green curve for $p^{\mathrm{sat}} = 3$, one can predict the maximal linear polarization of the individual rod at zero magnetic field to be positive for the DiRs #2 ($\rho_{l,0}^{\mathrm{max}} = 0.10$) and #3 ($\rho_{l,0}^{\mathrm{max}} = 0.32$). This means, that the light emitted from these DiRs is expected to be linearly polarized predominantly along the c-axis at low temperatures and zero magnetic field. However, as can be seen from Fig. 5-13 (a), the maximal linear polarization of the individual rod at the magnetic field $B = B^{\mathrm{sat}}$ is negative, namely $\rho_l^{\mathrm{max}} = -0.53$ and -0.38 for the samples #2 and #3, respectively.

As shown above, the theoretical model, which introduces the coupling of the dark exciton to the bright exciton state $F = 0^U$ in addition to the well known coupling to the $F = \pm 1$ states, can explain the significantly lower DCP, which is observed for DiRs in magnetic field experiments, compared to spherical NCs. The observed dependence on aspect ratio highlights the role of the dielectric enhancement effect, which favors emission polarized parallel to the c-axis in DiRs. The reason for the additional increase of the ratio $\Gamma_{20}/\Gamma_{21}^0$ with the increase of the DiR aspect ratio can be explained by an increase of the shape anisotropy in the plane perpendicular to the rod axis or by an increase of the Coulomb interaction anisotropy. However, the large number of free parameters in the theoretical model make it difficult to go beyond qualitative interpretations of the experimental data shown here. Further experimental studies are needed, which elucidate the relevance of each parameter and its dependence on the NC size and shape.

5.5 Summary

In summary, in this chapter a comprehensive study of PL polarization and exciton spin dynamics in CdSe/CdS core/shell NCs in external magnetic fields was presented. It was demonstrated, that it is possible to probe the orientation of NCs with anisotropic shell shape with respect to the magnetic field axis, by means of measuring the PL DCP induced by the magnetic field. This technique could be useful for testing the quality of nanorod based arrays for instance.

Regarding exciton spin dynamics it was found, that the spin relaxation of dark excitons is strongly related to the surface of CdSe in bare NCs or the interface between CdSe and CdS in core/shell systems. This was evidenced by a large decrease of the spin relaxation rate after adding a CdS shell. The importance of the interface in core/shell systems was highlighted by a strong core size dependence of the spin relaxation rate, which decreases for increasing core volume. In contrast, the overall NC surface seems to play only a minor role in this regard, as can be concluded from the weak dependence of the spin relaxation rate on shell thickness. The temperature and magnetic field dependences of the spin relaxation rate highlight the importance of confined acoustic phonons in the relaxation and recombination process of dark excitons. In this regard, DiR NCs show a very similar behavior compared to spherical core/shell systems and the spin relaxation rate at low magnetic fields seems to be suppressed by an acoustic phonon bottleneck.

Furthermore, the circular PL polarization of DiRs in magnetic fields was studied. Despite a notably low equilibrium DCP for randomly oriented DiRs compared to spherical core/shell NCs the results indicated a dependence of the saturated DCP on the aspect ratio of the NC. A theoretical model for analyzing and predicting the circular and linear polarization properties of DiR emission in magnetic field was described and compared to the experimental data. This model includes the dielectric enhancement effect as well as dark exciton recombination via coupling to bright exciton states with radiative transitions polarized parallel or perpendicular to the hexagonal c-axis and it was shown, that it can explain the strongly varying (almost saturated) DCPs typically observed even for spherical NCs in high magnetic field experiments.

Chapter 6

Fluorescence line narrowing in CdSe nanocrystals - Mechanisms of dark exciton radiative recombination

The understanding of the origin and the consequences of the exciton fine structure is important, since it determines the dynamics of excitons and thus the optical properties of NCs, as was demonstrated in the preceding chapters. Notably, the possibilities to affect exciton spin and recombination dynamics by altering the shape and size of the core or the shell have been elucidated.

Regarding exciton dynamics the most serious aspect about the fine structure is the nature of the exction ground state, since at low temperatures almost all radiative recombination occurs from this state. As was discussed in chapter 2, in spherical CdSe NCs this state is optically forbidden in the electric dipole approximation. [28] Although the dark exciton was discovered already almost twenty years ago, the mechanisms, which enable its radiative recombination are still not fully understood. In this chapter several mechanisms, which lead to dark exciton radiative recombination are discussed. Further, experimental results are shown, which support a recent theory, [157] that predicts dark exciton radiative recombination due to the interaction between excitons and dangling bonds at the NC surface.

The chapter starts with an introduction, which gives an overview over possible radiative recombination pathways and presents the basic idea of dangling bond assisted radiative recombination. Following that, the theory describing the dangling bond assisted recombination is briefly outlined. Afterwards the experimental results are shown and discussed. Finally, the results are summarized.

6.1 Introduction

As discussed in chapter 2, in CdSe NCs the initially eightfold degenerate exciton ground state $1S_{3/2}1S_e$ (in the spherical approximation) is split by the crystal field and the eh-exchange interaction into five energy levels, with total angular momentum projections $F = \pm 2$, $F = \pm 1$ and $F = 0$. A calculation of the exciton fine structure according to the theory of Efros et al. [28] as a function of NC size is depicted in Fig. 6-1 (a) for the case of a spherical NC. The exciton ground state is of the type $F = \pm 2$ and is therefore optically inactive in the electric dipole approximation. Separated by the bright-dark energy splitting ΔE_{bd}, which typically amounts to a couple of meV (see chapter 4), there is an optically allowed state $F = \pm 1^L$. As was shown in chapter 4, the dark exciton can be thermally activated by increasing the temperature, depending on the magnitude of ΔE_{bd}. Thereby the bright exciton state gets progressively populated. At low temperatures, however, thermal activation is suppressed and recombination stems solely from the dark exciton ground state. Since the angular momentum has to be conserved, radiative recombination from the dark exciton state is possible only, if it is assisted by acoustic or optical phonons, which take up a part of the angular momentum, or by magnetic field induced mixing of dark and bright states by fields perpendicular to the hexagonal c-axis, as discussed in section 2.2.4.

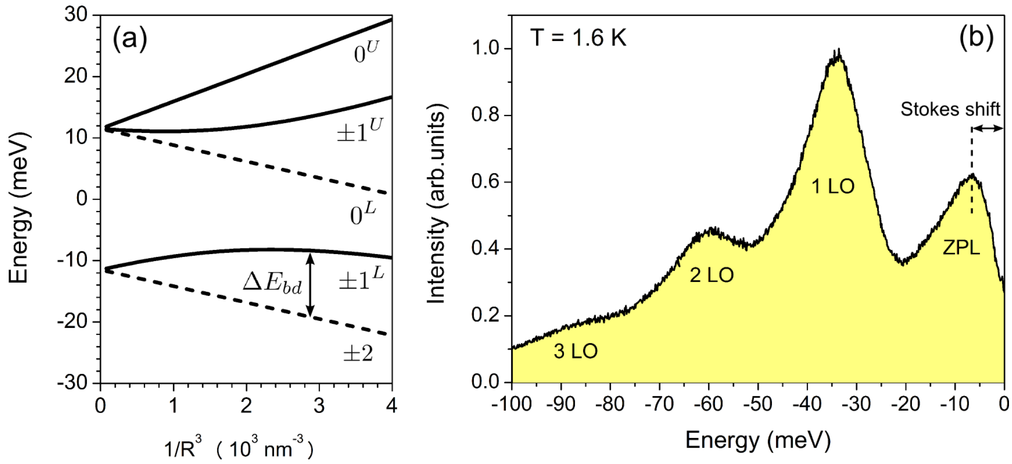

Figure 6-1: (a) Exciton fine structure for a spherical NC calculated according to the theory of Efros et al. [28]. The dashed lines denote optically inactive states. (b) FLN spectrum of CdSe NCs with core radius $R = 1.35$ nm at $T = 1.6$ K. The x-axis shows the red shift (in energy) of the PL with respect to the laser excitation energy.

Clear signatures of the different pathways of dark exciton radiative recombination can be observed in FLN experiments, where only a small fraction of NCs is resonantly excited and therefore inhomogeneous broadening is reduced. A typical spectrum is shown in Fig. 6-1 (b) for an ensemble of spherical NCs with radius $R = 1.35$ nm at a temperature $T = 1.6$ K. The x-scale shows the red shift of the PL with respect to the laser excitation energy (corresponding to 0 meV in the figure). The laser is in resonance with the $\pm 1^L$ bright states of the excited sub-ensemble. The first peak, located at $E = -7$ meV, is the so-called zero-phonon line (ZPL) and the Stokes shift of 7 meV corresponds to the bright-dark energy splitting ΔE_{bd}. The ZPL can contain Stokes and Anti-Stokes lines of acoustic phonons concealed due to inhomogeneous broadening, which cannot be fully avoided in practice. However, in single NC PL experiments such acoustic phonon replicas have been observed. [119,159] Notably it has been shown, that an external magnetic field increases the relative intensity of the ZPL. [29] This is due to the admixture of dark and bright exciton states by the magnetic field component perpendicular to the hexagonal axis and this effect is considered a clear prove for dark exciton recombination without the assistance of phonons. The FLN spectrum in Fig. 6-1 (b) exhibits additional peaks, which are further redshifted with respect to the laser line and which correspond to LO phonon assisted transitions. In the spectrum shown three peaks can be identified, corresponding

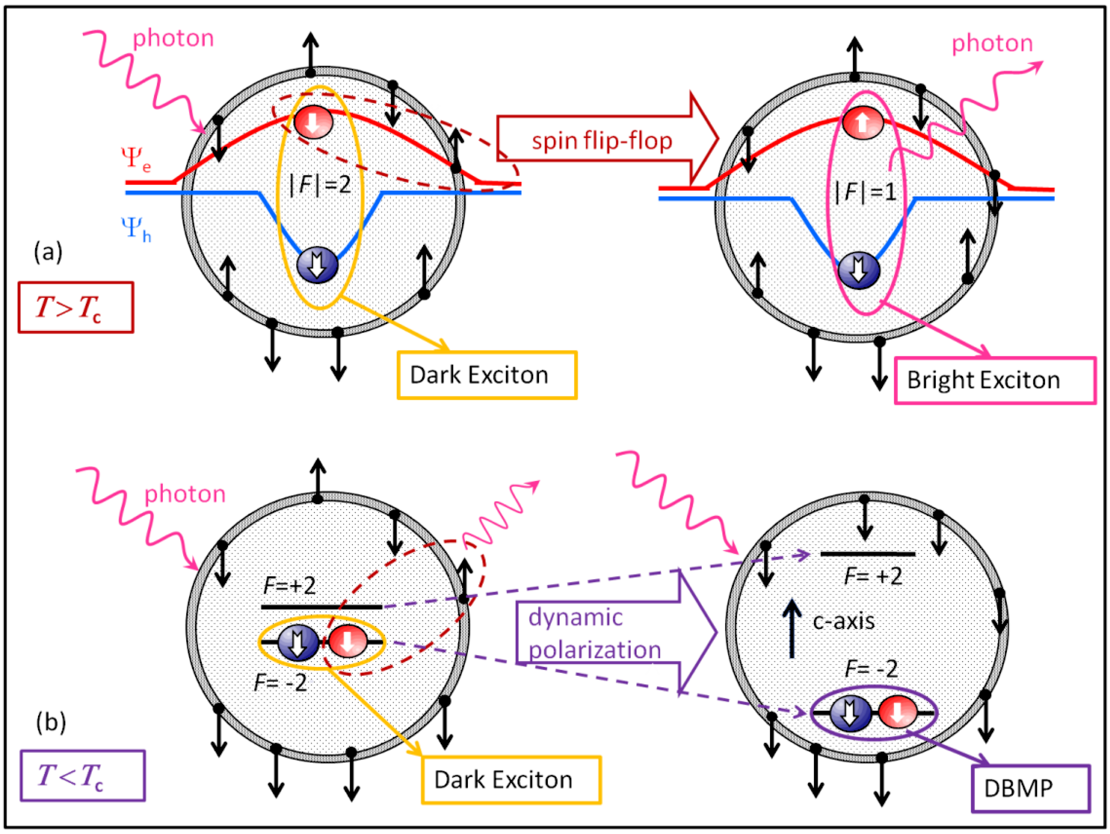

Figure 6-2: (a) Sketch illustrating the spin flip-flop assisted recombination of the dark exciton. (b) Illustration of the formation of a dangling bond magnetic polaron (DBMP). The image is taken from Ref. [157].

to the 1 LO, 2 LO and 3 LO phonon lines. The relative energy between the ZPL and the 1 LO phonon line is 27 meV, which is close to values of the LO phonon energy $E_{LO} = 25$ meV reported in the literature. [48]

The relatively high intensity of the 1 LO line clearly shows, that optical phonon assisted transitions play an important role for dark exciton radiative recombination. It has been shown, however, that with increasing temperature the relative intensity of the ZPL with respect to the 1 LO line increases considerably and that it dominates already at temperatures above approximately 5 K. At the same time the raise of temperature led to a clear blue-shift of the 1 LO phonon line as well as the ZPL, i.e. a decreasing Stokes shift with increasing temperature has been observed. [48] The origin of this blue shift as well as the strong increase of the ZPL intensity with temperature could not be identified until recently.

In their theoretical model, [157] A. V. Rodina and Al. L. Efros consider the activation of dark exciton recombination by surface dangling bonds, which are unsatisfied valences at the surface atoms and which interact with the exciton via the exchange interaction. This interaction induces an electron- and dangling bond- spin flip-flop process, converting the dark exciton state into a virtual bright one, which can radiatively recombine. This idea is illustrated in Fig. 6-2 (a). An incident photon creates an e-h pair, which after relaxation ends up with parallel spins, corresponding to a dark exciton. At temperatures above a critical point T_c the dangling bond spins are oriented arbitrarily and can lead to an admixture of the bright and dark exciton states. Due to its lower effective mass, the electron wavefunction ψ_e is more delocalized compared to the hole wavefunction ψ_h, therefore interaction with dangling bond spins occurs predominantly for the electron. Due to the admixture with the bright exciton state, the initial dark exciton subsequently recombines radiatively. As illustrated in Fig. 6-2 (b), at temperatures below the critical temperature T_c, the spin flip-flop assisted radiative recombination and repetitive excitation can lead to the formation of a state, which is termed a dangling bond magnetic polaron (DBMP), with dangling bond spins aligned along the hexagonal c-axis. This leads to an increased Zeeman-splitting between the dark exciton $F = \pm 2$ states and to a suppression of dangling bond assisted radiative recombination of the dark exciton at very low temperatures. This DBMP is assumed to be partly responsible for the enhanced sensitivity of the ZPL intensity on temperature and the concomitant shift of the ZPL to higher energies, since at higher temperatures the polarization of dangling bond spins is lost and spin flip-flop processes are possible. The blue shift then occurs as a consequence of the loss of the polaron binding energy.

In a previous FLN experiment, the temperature dependent Stokes shift and the increase of the relative intensity of the ZPL with increasing temperature have been observed. [48] This study provides further experimental evidence, which supports the picture of dangling bond assisted dark exciton radiative recombination and the formation of DBMPs. In the following, the essential theoretical considerations of dangling bond assisted radiative recombination, as they are reported in Ref. [157], are briefly reviewed.

6.2 Theoretical considerations

As discussed in the preceding section, dark exciton recombination is assumed to occur by coupling to optical and acoustic phonons as well as by the interaction of the exciton with surface dangling bonds. Thus the total radiative rate of the dark exciton can be written as

$$\frac{1}{\tau_{\mathrm{r}}} = \Gamma_{\mathrm{r}} = \Gamma_{\mathrm{ph}}^{\mathrm{o}} + \Gamma_{\mathrm{ph}}^{\mathrm{a}} + \Gamma_{\mathrm{db}}, \tag{6.1}$$

where Γ_{ph}^{i} with $i = \mathrm{o,a}$ denote the rates for recombination accompanied by emission or absorption of optical and acoustic phonons, respectively and Γ_{db} the rate for dangling bond assisted recombination.

In the framework of second order perturbation theory the process of dark exciton recombination is considered to occur in form of a virtual transition from the $|F| = 2$ to a bright state and subsequent radiative recombination. The former transition could be realized by a spin flip of the electron, which can be described by the matrix element $V_e = |\langle 1/2|\,\hat{V}_e\,|{-1/2}\rangle| = |\langle -1/2|\,\hat{V}_e\,|1/2\rangle|$ or by mixing of hole wavefunctions with matrix elements $V_{h,1} = |\langle\psi_{\pm 3/2}|\,\hat{V}_h\,|\psi_{\pm 1/2}\rangle|$ and $V_{h,2} = |\langle\psi_{\pm 3/2}|\,\hat{V}_h\,|\psi_{\mp 1/2}\rangle|$. As shown in Ref. [28] non-vanishing $V_{h,1}$ and V_e lead to a coupling between the $|F| = 2$ and $|F| = 1$ states, whereas $V_{h,2}$ couples the $|F| = 2$ to a $|F| = 0$ state. In the first case the resulting PL is circularly polarized in the plane perpendicular to the c-axis, while in the second case the PL is linearly polarized along c. Interactions with phonons as well as with dangling bond spins lead to non-vanishing matrix elements and thereby to radiative recombination. In the following only the dangling bond interaction will be discussed in detail.

The electron interacts with the dangling bond spins via the exchange interaction, which can be written as

$$\hat{H}_{\mathrm{ss}} = \sum_j \hat{H}_{\mathrm{ss}}{}^j = -\alpha \sum_j \boldsymbol{\sigma}^e \cdot \boldsymbol{\sigma}^j, \tag{6.2}$$

where $\boldsymbol{\sigma}^e$ and $\boldsymbol{\sigma}^j$ are the electron and dangling bond spin operators, respectively. The coefficient α in case of a spherical NC, where the 1S electron interacts similarly with all dangling bonds, can be written as $\alpha = \tilde{\alpha} a_0^3 \xi^2(a)$, with the exchange strength constant $\tilde{\alpha}$, the lattice constant a_0 and the square of the electron wavefunction at the NC surface $\xi(a)^2$. In small NCs, for which the eh-exchange interaction is comparably large, the electron spin is aligned with the hexagonal axis and due to the spin-spin interaction the dangling bonds get aligned as well. If the hexagonal axis is taken to point in the z-direction, the exchange-Hamiltonian Eq.(6.2) can be written as

$$\hat{H}_{\mathrm{ss}} = \hat{H}^j_{\mathrm{zz}} + \hat{H}^j_{\text{flip-flop}} = -\alpha \sigma^e_z \sigma^j_z - \frac{\alpha}{2}[\sigma^e_+ \sigma^j_- + \sigma^e_- \sigma^j_+], \tag{6.3}$$

where $\sigma^{e,j}_{\pm} = \sigma^{e,j}_x \pm i\sigma^{e,j}_y$.

The first term in Eq.(6.3) leads to a contribution of the dangling bonds to the exciton energy. In case of a spontaneous polarization of the dangling bond spins, this gives rise to a Zeeman-splitting of the dark exciton state. It can be shown, that this is equal to

$$\Delta E_{\mathrm{ex}} = 2\alpha N_{\mathrm{db}} \rho_{\mathrm{db}}, \tag{6.4}$$

where N_{db} is the number of dangling bonds and $\rho_{\mathrm{db}} = (N^-_{\mathrm{db}} - N^+_{\mathrm{db}})/N_{\mathrm{db}}$ describes the dangling bond spin polarization with respect to the hexagonal axis.

The second term in Eq.(6.3) leads to an admixture of the bright exciton states $|F| = 1$ to the dark exciton states and radiative decay, accompanied by a simultaneous spin flip of an electron and a dangling bond spin in opposite direction. It can be written as $\hat{V}^{\pm}_e = \hat{A}^{\mp} \sigma^e_{\pm} = -\alpha/2 \sum_j \sigma^j_{\mp} \sigma^e_{\pm}$. In the framework of second order perturbation theory the resulting radiative decay rate is calculated as

$$\Gamma^{\pm 2}_{\text{flip-flop}} = \frac{\langle |\, \hat{A}^{\mp} \,|^2 \rangle}{3\eta^2} \frac{1}{\tau_0} = 2\left(\frac{\alpha}{\eta}\right)^2 \frac{1}{6\tau_0} N^{\mp}_{\mathrm{db}} = 2\gamma_{\mathrm{ex}} N^{\mp}_{\mathrm{db}}. \tag{6.5}$$

Here, the operator $\langle |\, \hat{A}^{\mp} \,|^2 \rangle = \alpha^2 N^{\pm}_{\mathrm{db}}$, with $N^{\pm}_{\mathrm{db}} = N_{\mathrm{db}}(1 \mp \rho_{\mathrm{db}})/2$, is averaged over the dangling bond spin polarization and τ_0 is the radiative lifetime of the $F = 0^U$ state [see Eq.(2.27)].

If the dangling bond spins are polarized, the rates for the $F = -2$ and $F = +2$ dark exciton differ from each other and the dangling bonds give rise to an exciton polarization given by $\rho_{\mathrm{ex}} = (N_{\mathrm{ex,-2}} - N_{\mathrm{ex,+2}})/N_{\mathrm{ex}}$, where N_{ex} is the average number of excitons. Assuming a thermal distribution between the dark exciton sublevels, which are split by the dangling bonds according to Eq.(6.4), and that the spin relaxation time is much shorter than the exciton lifetime the overall radiative decay rate due to dangling bonds can be written as

$$\frac{1}{\tau_{\mathrm{db}}} = \Gamma_{\mathrm{db}} = \gamma_{\mathrm{ex}} N_{\mathrm{db}}[1 - \rho_{\mathrm{db}} \rho_{\mathrm{ex}}], \tag{6.6}$$

where $\rho_{\mathrm{ex}} = \tanh(\Delta E_{\mathrm{ex}}/2k_B T)$ is the exciton spin polarization. From Eq.(6.6) it is clear, that if $\rho_{\mathrm{db}}\rho_{\mathrm{eq}} \rightarrow 1$, i.e. if the dangling bonds and excitons are polarized, the radiative recombination is suppressed. If $\rho_{\mathrm{db}} = \rho_{\mathrm{eq}} = 0$ the radiative rate is proportional to the number of dangling bonds.

If a spontaneous polarization of dangling bond spins gives rise to a Zeeman-splitting ΔE_{ex} between the dark exciton states, at low temperatures an exciton polarization occurs in the case, when the spin relaxation is much faster compared to the exciton recombination. This leads to dangling bond flip-flops with favorable spin orientation and thereby to a dangling bond polarization, which in turn increases the Zeeman-splitting: A chain reaction occurs, which leads to a polarization of both, the excitons and dangling bonds. This polarized state is termed dangling bond magnetic polaron (DBMP). The formation of the DBMP at low temperatures leads to suppression of dangling bond assisted radiative recombination of the dark exciton, because the effective magnetic field originating from the dangling bond spins is always parallel to the hexagonal axis.

The time evolution of dangling bond spin polarization can be derived from the rate equations

$$\frac{dN_{\mathrm{db}}^{\pm}}{dt} = -N_{\mathrm{db}}^{\pm}[2\gamma_{\mathrm{ex}}N_{\mathrm{ex},\mp2} + \gamma_{\mathrm{db}}^{\pm}] + N_{\mathrm{db}}^{\mp}[2\gamma_{\mathrm{ex}}N_{\mathrm{ex},\pm2} + \gamma_{\mathrm{db}}^{\mp}]. \tag{6.7}$$

Here, $2\gamma_{\mathrm{ex}}N_{\mathrm{ex},\pm2} = \gamma_{\mathrm{ex}}N_{\mathrm{ex}}(1 \mp \rho_{\mathrm{ex}})$ describes dangling bond spin flips during radiative recombination of the dark exciton. $\gamma_{\mathrm{db}}^{\pm}$ is the dangling bond spin relaxation rate independent of the dark exciton radiative recombination. Thus, the dangling bond spin pumping gets more efficient for a high average number of excitons in the NC. The exciton polarization induces a Zeeman-splitting of the dangling bond states with opposite spin orientation, which amounts to $\Delta E_{\mathrm{db}} = 2\alpha\rho_{\mathrm{ex}}$. Therefore one also has to consider thermal equilibration of the dangling bond spin system. With the condition $\gamma_{\mathrm{db}}^{-} = \gamma_{\mathrm{db}}^{+}\exp\left(-\Delta E_{\mathrm{db}}/k_BT\right)$, the time evolution of the dangling bond spin polarization can be written as

$$\frac{\rho_{\mathrm{db}}}{dt} = -2\gamma_{\mathrm{ex}}N_{\mathrm{ex}}[\rho_{\mathrm{db}} - \rho_{\mathrm{ex}}] - \gamma_{\mathrm{db}}[\rho_{\mathrm{db}} - N_{\mathrm{ex}}\overline{\rho}_{\mathrm{db}}]. \tag{6.8}$$

Here $\gamma_{\mathrm{db}} = \gamma_{\mathrm{db}}^{+} + \gamma_{\mathrm{db}}^{-}$ and $\overline{\rho}_{\mathrm{db}} = (\gamma_{\mathrm{db}}^{+} - \gamma_{\mathrm{db}}^{-})/\gamma_{\mathrm{db}} = \tanh\left(\alpha\rho_{\mathrm{ex}}/k_BT\right) \approx \alpha\rho/k_BT$ is the spin polarization of dangling bonds in thermal equilibrium and in the presence of an exciton. If no excitons are present it is expected, that the dangling bond polarization vanishes during the equilibration of the system.

The steady state solution of Eq.(6.8) is

$$\rho_{\mathrm{db}} = \frac{2\rho_{\mathrm{ex}}\gamma_{\mathrm{ex}}N_{\mathrm{ex}} + \gamma_{\mathrm{db}} + N_{\mathrm{ex}}\overline{\rho}_{\mathrm{db}}}{2\gamma_{\mathrm{ex}}N_{\mathrm{ex}} + \gamma_{\mathrm{db}}}. \tag{6.9}$$

At high exciation intensity, when the number of excitons is large and $\gamma_{\mathrm{db}} \ll \gamma_{\mathrm{ex}}N_{\mathrm{ex}}$, $\rho_{\mathrm{db}} = \rho_{\mathrm{ex}}$ can be assumed. In this case it follows, that the exciton thermal-equilibrium polarization can be rewritten to

$$\rho_{\mathrm{ex}} = \tanh\left(\frac{\alpha\rho_{\mathrm{ex}}N_{\mathrm{db}}}{k_BT}\right). \tag{6.10}$$

This state is the DBMB and it can occur for high excitation intensities and is favorable in small NCs, for which αN_{db} is large.

It is expected, that the formation of the DBMP at low temperatures and high average exciton populations, on the one hand leads to the suppression of dangling bond assisted dark exciton radiative recombination. Therefore at very low temperatures predominantly phonon assisted recombination occurs and the relative intensity of the ZPL is expected to be small. On the other hand the polaron binding energy induces an additional Stokes shift, which should result in a blueshift of the ZPL with increasing temperature. According to the relation

$$N_{\mathrm{ex}} = \frac{I_{\mathrm{ex}}\sigma_{\mathrm{cr}}(\omega_{\mathrm{ex}})}{\hbar\omega_{\mathrm{ex}}}\tau, \tag{6.11}$$

where ω_{ex} is the excitation frequency, $\sigma_{\mathrm{cr}}(\omega_{\mathrm{ex}})$ the absorption crosssection at this frequency and τ the exciton lifetime, the average number of excitons can be influenced via the excitation intensity. [163] Thus, it is expected, that with increasing excitation powers the ZPL shifts to lower energies and that its relative intensity decreases. These aspects have been addressed in a FLN experiment and the results are presented in the following section.

6.3 Experimental results and discussion

The NCs used in this study are bare CdSe NCs with a diameter of 2.7 nm (sample #R2 in Table 3-3).

The upper panel in Fig. 6-3 (a) shows a FLN spectrum for these NCs and its evolution with increasing temperature, obtained for an average excitation power $P = 10$ μW. The intensity is normalized to the peak intensity of the 1 LO phonon line. The laser energy in the figure corresponds to 0 meV. Due to the cross-polarized excitation/detection scheme, as described in section 3.2.1, the laser is not visible in the spectrum. Two general observations can be made: On the one hand, with increasing temperature the relative intensity of the ZPL increases with respect to the 1 LO phonon line. While at 1.6 K the 1 LO phonon line is larger than the ZPL, at 10 K the ZPL contains most of the detected photons. On the other hand, with increasing temperature both lines, the ZPL and the 1 LO line, shift to higher energies, i.e. they shift closer to the laser energy, as indicated by the dashed lines and arrows.

In the upper panel in Fig. 6-3 (b) the FLN spectrum is shown for various excitation powers, obtained at $T = 1.6$ K. An increase of the excitation power by approximately two orders of magnitude, from 5 μW to 3 mW changes the relative intensity of the ZPL only slightly. Importantly, the increase of power leads to a clear redshift of the ZPL and the 1 LO phonon line, i.e. the lines shift away from the laser energy.

The lower panels in Figs. 6-3 (a) and (b) show the evolution of the relative intensities and the spectral positions of the ZPL and 1 LO line with increasing temperature and power in more detail. As is obvious from the left panel, the intensity and spectral positon of the ZPL and the 1 LO line is very sensitive on changes of the temperature especially at very low temperatures below approximately 5 K. Within the measured temperature range, the ZPL and the 1 LO line shift by 2.7 meV and 7.9 meV, respectively. Below 3 K the peak intensity of the 1 LO line is larger compared to the ZPL, at 3 K the peak intensities are equal, i.e. $I_{ZPL}/I_{1LO} = 1$. The ratio increases up to a value of approximately 1.6 and stays almost constant above $T = 20$ K. Referring to the lower panel of Fig. 6-3 (b), an increase of power from 5 μW up to 2 mW leads to a redshift of the

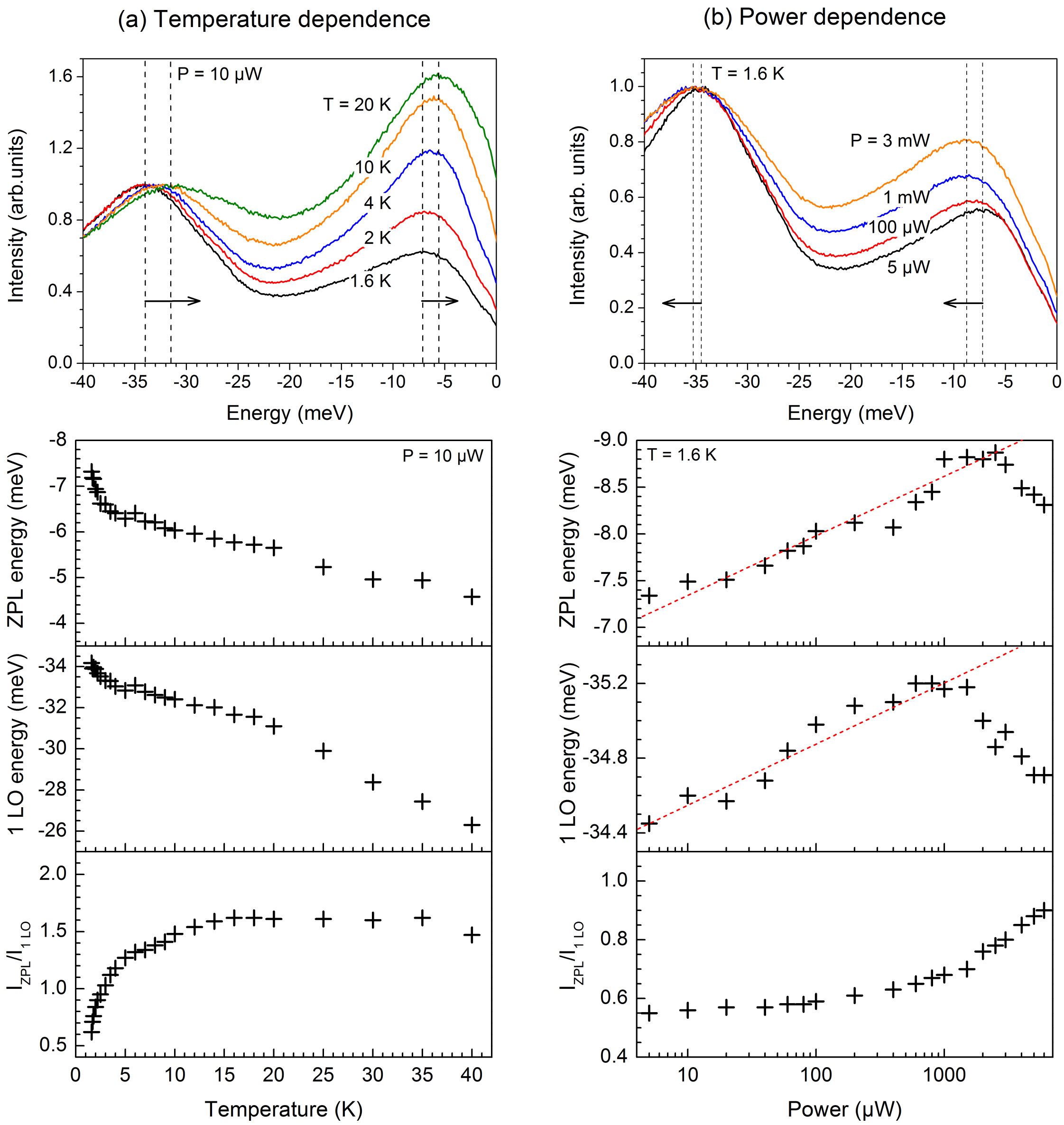

Figure 6-3: Upper panel: (a) Temperature dependence at $P = 10\ \mu$W and (b) power dependence at $T = 1.6$ K of the FLN spectrum of CdSe NCs with a diameter of 2.7 nm. The arrows and dashed lines indicate the shifts of the peaks with increasing temperature (a) and power (b). Lower panel: Corresponding dependences of the ZPL energy, the 1 LO energy and the ratio of $I_{\mathrm{ZPL}}/I_{\mathrm{1LO}}$ with increasing temperature (a) or power (b). The red dashed lines are guides to the eye.

ZPL and the 1 LO line by 1.5 meV and 0.5 meV, respectively. The trend is highlighted by the red dashed lines. In this power range the relative intensity of ZPL and 1 LO line stays almost constant. Above 2 mW the ratio starts to increase significantly and the shift of the ZPL and 1 LO lines goes in the opposite direction, i.e. the lines shift back to higher energies.

The described observations can be understood with the theoretical model of dangling bond assisted dark exciton radiative recombination, which was outlined in the previous section. At low temperatures $T < T_c$ the model predicts the formation of the DBMP, due to the cumulative polarization of dangling bond and exciton spins. This should result in a decrease of spin flip-flop assisted dark exciton radiative recombination and thus to a decrease of the relative intensity of the ZPL at low temperatures, in accordance with the experimental results plotted in the lower panel of Fig. 6-3 (a). In the described model, the redshift of both ZPL and 1 LO line with decreasing temperature results from the Zeeman-splitting of the dark exciton state, induced by aligned dangling bonds. The energies of the Zeeman-sublevels can be written as $E_F^{\pm 2} = E_F \pm \Delta E_{ex}/2$, where E_F is the energy of the dark exciton states in the absence of the DBMP, i.e. at temperatures $T > T_c$. The thermal population of the Zeeman-sublevels and different rates $\Gamma^{\pm 2}_{\text{flip-flop}}$, as they are described by Eq.(6.5), lead to the observed redshift with decreasing temperature. The formation of the DBMP strongly depends on the average number of excitons in the NC and is therefore expected to be enhanced at high excitation powers. Thus, with increasing power a redshift of the ZPL and the 1 LO line is expected, which is in accordance with the power dependences of the 1 LO line and ZPL energies depicted in the lower panel of Fig. 6-3 (b). The blueshift of the lines, which occurs at excitation powers $P > 2$ mW and which is accompanied by a strong increase of the intensity ratio I_{ZPL}/I_{1LO}, most likely is a result of laser induced heating of the sample. As can be seen from the spectra shown in Fig. 6-3 (a) and (b), changes in temperature and power lead to shifts of the spectral lines in opposite directions and thus these effects may partly compensate each other. While the temperature dependence can be reliably performed with a constant excitation intensity, the increase of power in the experiment always results in progressive heating of the sample by the laser light. The experiment was performed in liquid helium to allow for the most efficient cooling of the sample, however, the effect of laser induced heating cannot be fully avoided in practice. This can also explain, why for power levels below 2 mW changes in the ratio I_{ZPL}/I_{1LO} cannot be observed [see lowest picture in Fig. 6-3 (b)]. Theoretically it is expected, that the progressive polarization of dangling bond and exciton spins leads to a suppression of dangling bond assisted radiative recombination and thus to a decrease of the relative intensity of the ZPL. Most likely, the increasing amount of heat, deposited by the laser, compensates for this decrease. Nevertheless, the observed redshift of the spectral lines with increasing power point towards the progressive formation of the DBMP, due to the dynamical polarization of exciton and dangling bond spins.

It is expected, that the polarization of the dangling bond spins resulting from the exciton-dangling bond interaction vanishes over time, when the sample is not illuminated. The system acquires a thermal equilibrium, thus the shift of the spectral lines with power is expected to be reversible. This aspect was experimentally addressed in a time-dependent pump-probe study. In the first part, the sample was continuously excited using an excitation power of 1 mW at a temperature $T = 1.53$ K. At specific times a spectrum was acquired and the ZPL spectral position was determined. The result is depicted in Fig. 6-4 (a). The figure shows the absolute energy shift over time (the line shifted to lower energies, away from the laser line). Obviously, when the illumination of the sample is started, the spectral position of the ZPL changes over time. After approximately 400 s it reaches its final position, which is shifted by 0.9 meV with respect to the initial position, and stays constant until the illumination is stopped after 900 s. The red line corresponds to a fit of the datapoints with a monoexponential increase function $A(t) = A_0[1 - \exp(-t/\tau)]$, where $A(t)$ denotes the absolute energy-shift as a function of time, A_0 the maximal energy shift and τ the characteristic risetime. It is determined to be $\tau = 104 \pm 28$ s, although, due to the small number of available data points, the

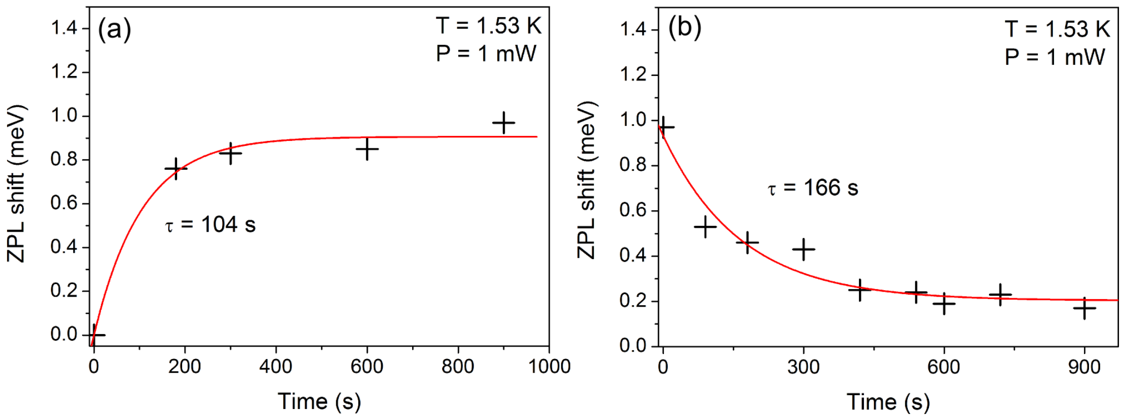

Figure 6-4: Time evolution of the relative ZPL energy shift. (a) shows the evolution after the start of continuous excitation at $t = 0$. (b) shows the evolution after the excitation laser is blocked at $t = 0$. Only for acquisition of the spectrum the sample was exposed to the laser light. The red lines are fits of the experimental data, using a monoexponential increase (a) or decrease (b), respectively. The characteristic times τ are given in the plot.

uncertainty in this time is rather large. Figure 6-4 (b) shows the evolution of the spectral position of the ZPL after termination of the continuous illumination. Here, only during the acquisition of the spectrum the sample was exposed to light for 100 ms in each case. Apparently, the shift, which was previously induced by the constant illumination of the sample, gradually disappears over time. The characteristic time τ for this process was determined by fitting the experimental datapoints with a monoexponential decrease $A(t) = A_0 \exp(-t/\tau)$. The fit yields $\tau = 166 \pm 38$ s. Apparently, within the measured time interval the induced spectral shift does not fully disappear. This could result from the relatively high excitation power, which was used for probing the spectral position of the ZPL $P = 1$ mW. It is expected, that, although the acquistion time for each spectrum of 100 ms is comparably short, the repetitive illumination by the laser counteracts the relaxation of the system.

Interestingly, the characteristic time for the relaxation of the energy shift is surprisingly long, i.e. $\tau = 166$ s. This time, in the framework of the described theory, should correspond to the dangling bond spin relaxation time $1/\gamma_{db}$, which is independent of the exciton-dangling bond interaction (see Eq.(6.7)). However, such long times point towards the involvement of the nuclear spin system of atoms located at the surface, as it is only weakly coupled to the lattice and thus spin relaxation occurs on long timescales. [160, 161] However, to elucidate the exact origin of the long relaxation time will be subject to further dedicated experimental and theoretical studies.

6.4 Summary

In this chapter, several mechanisms, which enable dark exciton radiative recombination have been discussed. Notably, a recent theory, [157] which proposes dark exciton recombination by exciton-dangling bond interaction, has been outlined. The essential theoretical predictions for FLN experiments resulting from this model, namely an increase of the relative intensity of the ZPL compared to the 1 LO phonon line with increasing temperature, a blue shift of the ZPL as well as the 1 LO phonon line with increasing temperature and a redshift of these spectral lines with increasing power, could be experimentally evidenced by means of FLN spectroscopy of bare CdSe NCs. The spectral redshift of the ZPL and the 1 LO line with increasing power was found to be time-dependent and reversible, supporting the picture of dangling bond spin equilibration in the absence of excitons.

Chapter 7

Summary and outlook

This thesis provides new insights in excitonic processes in colloidal semiconductor NCs, which were experimentally addressed by means of time-resolved PL spectroscopy and fluorescence line narrowing. Here, the focus is laid on the investigation of the exciton fine structure and exciton dynamics, which determine the optical properties of NCs at low temperatures and which strongly depend on the NC material and its architecture, i.e. its size and its shape.

Heteronanostructured particles are of prominent interest, since they provide a great versatility regarding the manipulation of optical properties in terms of wavefunction engineering. This aspect was intensively explored in chapter 4. It was investigated, how the size and shape of the shell in NCs with core/shell anatomy can be used to affect exciton recombination dynamics and to control the eh-exchange interaction and thereby affect the fine-structure splitting between spin singlet and triplet states. To this end, the PL decay was measured as a function of temperature for NCs with a spherical core surrounded by a rod-shaped shell with various geometrical extensions. The data were analyzed and interpreted in terms of a three level system and the fine-structure splitting as well as bright and dark exciton radiative recombination rates were extracted. It was found, that the fine-structure splitting strongly depends on the diameter of the shell, whereas the rod length does not matter in this regard. This was attributed to the significant but limited leakage of the electron wavefunction into the shell and the resulting decrease of the eh-exchange interaction. The dark exciton radiative lifetime was found to decrease with increasing shell diameter. This was attributed to the corresponding change in the fine-structure splitting, giving rise to a reduced mixing between optical allowed and forbidden states. An increase of the bright exciton radiative rate was observed for increasing shell diameter and was ascribed to the decreasing wavefunction overlap between electron and hole.

From a technological point of view, these findings are valuable for designing and optimizing optical devices, such as LEDs, based on core/shell heteronanostructures. As discussed in Ref. [1] one of the main obstacles in this regard is the improvement of the external quantum efficiency EQE of NC based LEDs, which is EQE $\propto \chi \cdot \eta_{PL}$, where χ is the fraction of excitons inside the NC with spin allowed optical transitions and η_{PL} is the PL quantum yield associated with these transitions. As was shown in chapter 4, the use of core/shell NCs provides manifold possibilities to affect these parameters by means of the energy splitting between optical allowed and forbidden states and their respective radiative lifetimes, which determine the competition between radiative and nonradiative recombination of excitons.

In chapter 5 the experimental investigation of exciton spin dynamics and PL polarization in core/shell NCs in external magnetic fields was presented. Core/shell NCs with spherical and rod shaped shells of varying size were investigated at low temperatures in an external magnetic field. The time-resolved degree of circular polarization was measured as a function of temperature, magnetic field and NC shape. From the curves the spin relaxation rate and the equilibrium polarization degree of the PL were extracted.

Due to the strong confinement of carriers in NCs, the exciton spin is effectively protected from environmental perturbations and therefore NCs are appealing candidates for spin-memory applications, where a long time spin coherence is required. Especially the dark exciton, due to its comparatively long radiative lifetime can play a key role in this regard, since it allows the read-out of an optically imprinted spin orientation on microsecond timescale, as discussed in Ref. [162]. The experimental investigations presented in chapter 5 elucidate the impact of the geometrical parameters of core/shell NCs on exciton spin relaxation, i.e. the loss of spin coherence. In this regard it was shown, that especially the core size strongly affects the relaxation rates between the Zeeman-split dark exciton states. More precisely, the relaxation rate was found to be inversely proportional to the volume of the core and for the shell thickness only a weak dependence was observed. For NCs without a shell, the relaxation rate was found to be increased by an order of magnitude. These observations led to the conclusion, that the surface of the NC as well as the core/shell interface play a central role in the process of spin relaxation and that, also in this regard, wavefunction engineering can be useful for controlling the interaction of the exciton wavefunction with the surface or interface. The magnetic field dependence of the spin relaxation rate indicates the existence of an acoustic phonon bottleneck in these structures, which hinders relaxation between Zeeman-levels at small splittings and therefore contributes to a long spin lifetime.

In magnetic field experiments the dependence of the circular polarization on the field strength in an ensemble of spherical NCs could successfully be described by a theoretical model, which considers radiative recombination of the dark exciton ground state via the optical bright states with angular momentum projection $F = \pm 1$, and predicts the circular polarization degree of the PL of an ensemble of randomly oriented NCs to saturate at 75% in high magnetic fields. [43] The experimental results presented in chapter 5, however, indicated, that the DCP varies strongly with particle shape and also for (presumably) spherical NCs saturation values significantly lower compared to the theoretical limit have been previously observed. [44,45] For explanation of these effects the common theoretical model was extended by taking into account additional coupling to $F = 0$ fine structure states as well as a dielectric enhancement effect, which is present in NCs with anisotropic shape. Both effects lead to enhanced linear polarization of the PL and, as shown in chapter 5, thereby intrinsically reduce the circular PL polarization. The presented model is useful for analyzing the PL polarization of NCs in external magnetic fields can help to understand the size and shape dependence of processes related to the exciton fine structure.

The understanding of the mechanisms of dark exciton radiative recombination is one of the central goals in research on colloidal NCs, since, as mentioned earlier, it determines the optical response of a NC and thus its suitability for application in opto-electronic devices. The mechanism of magnetic field induced mixing of bright and dark exciton states, which enables dark exciton radiative recombination, was found already twenty years ago. [28,29] Still, the origin of a ZPL in FLN spectra in the absence of an external magnetic field and its dependence on temperature remains unclarified. The experimental findings presented in chapter 6 support a recent theoretical study, which proposes dark exciton radiative recombination as a result of the interaction of excitons with surface dangling bonds. In this model, dark exciton radiative recombination is enabled by spin flip-flop processes of electron and dangling bond spins, which convert the initial dark exciton into a virtual bright one, which can radiatively recombine. Further, at low temperatures and high excitation intensities this model predicts the formation of a state, in which exciton spins as well as dangling bond spins are polarized. This state is termed a dangling bond magnetic polaron and it is assumed that it inhibits the radiative recombination of the dark exciton. The essential predictions for FLN experiments following from this theory, which include shifts of the spectral lines with temperature and power as well as varying intensities of the spectral lines could be evidenced by means of FLN spectroscopy on bare CdSe NCs.

The theoretical discussions and experimental findings presented in this thesis highlight the manifold possibilities to affect and control excitonic processes in colloidal NCs, especially the recombination and relaxation dynamics of excitons, by means of designing NCs with a specific size, shape and core/shell architecture. Considering the high expertise in synthesis methods nowadays, which allows production of NCs of almost arbitrary size and shape and the combination of a variety of materials, the opportunities for using NCs in commercial opto-electronic applications are obvious. Still, the mechanisms, which affect exciton recombination and relaxation, are not fully understood. Especially the role of the core/shell interface or the NC surface regarding these processes remains unclear, although its importance regarding spin relaxation and exciton radiative recombination was clearly evidenced by the experimental findings presented in this thesis. Thus, further experimental studies elucidating the interaction of excitons with the NC surface or core/shell interface are needed.

Finally, due to the intrinsic toxicity of CdSe, alternatives to cadmium-based semiconductor NCs are generally desirable. [164] In this regard, III-V semiconductors such as InP have turned out to be a promising alternative, since they can have comparable optical properties regarding the spectral window, which can be achieved by tuning the optical bandgap via the NC size. [165] The fabrication of high quality InP based NCs unfortunately is more challenging in comparison to II-VI materials and early attempts resulted in extremely low quantum yields. However, recently progress has been made in this regard, [165–169] allowing for synthesis of indium-based core/shell NCs with quantum yields as high as 70%. [168,169] This promising development makes it necessary to extend the research and transfer the knowlegde of CdSe based NCs to other material systems, in order to ensure the development and production of environmental friendly NC based devices.

Abbreviations and symbols

List of abbreviations

Abbreviation	**Meaning**
arb. units/a. u.	Arbitrary units
CB	Conduction band
CCD	Charge-coupled device
CW	Continuous wave
DBMP	Dangling bond magnetic polaron
DCP	Degree of circular polarization
DLP	Degree of linear polarization
DiR	Dot-in-rod
DOS	Density of states
e-h	Electron-hole
EMA	Effective mass approximation
FLN	Fluorescence line narrowing
FWHM	Full width at half maximum
lh	Light hole
LA	Longitudinal-acoustic
LED	Light-emitting diode
LO	Longitudinal-optical
NC	Nanocrystal
so	Split-off
TEM	Transmission electron microscope
TCSPC	Time-correlated single photon counting
TRDCP	Time-resolved degree of circular polarization

VB	Valence band
ZPL	Zero phonon line

List of symbols

Symbol	**Meaning**
a, R	Radius of a NC or the core in case of a core/shell NC
a_0, c_0	Lattice constants
a_{ex}	Bulk exciton Bohr radius
A_{21}	Einstein coefficient for a transition between states 2 and 1
b	Semi-major axis of an ellipsoid
$\mathbf{B}$, B	Magnetic field
c	Speed of light in vacuum ($2.9979 \cdot 10^{-10}$ m/s)
c-axis	Axis of high symmetry of the hexagonal crystal lattice
d	Semi-minor axis of an ellipsoid
D	Core diameter
$\mathbf{e}$	Light polarization vector
E	Energy
ΔE, ΔE_{ex}	Zeeman splitting between fine structure states
ΔE_{bd}	Bright-dark splitting
ΔE_{db}	Dangling bond Zeeman splitting
ΔE_c, ΔE_v	Conduction and valence band energy offsets
E_g	Band gap energy
E_0	Electric field of light
E_{loc}	Local electric field
f	Focal length
f_{ex}	Selective excitation factor
$f_{LF}^{\vert\vert}$, $f_{LF}^{\perp}$	Local field factor parallel and perpendicular to the light field
f_{or}	Orientation factor

F	Exciton total angular momentum projection
g_e	Electron g factor
g_{ex}	Exciton g factor
g_h	Hole g factor
$\hbar$	Planck constant ($\hbar = h/2\pi = 1.05471 \cdot 10^{-34}$ Js)
$\hat{H}$	Hamilton operator
$I_{\sigma+}$, $I_{\sigma-}$	Intensities of right and left circular polarized light
I_{ex}	Excitation intensity
$\mathbf{J}$	Hole total angular momentum operator
j_l	Bessel function
$\mathbf{k}$, k	Wavevector and wavenumber
k_B	Boltzmann constant ($1.38065 \cdot 10^{-23}$ J/K)
l	Angular quantum number
L	Shell length of DiR NCs
m	Magnetic quantum number
m_0	Free electron mass ($9.1024 \cdot 10^{-31}$ kg)
m_{eff}	Effective mass
$m_{c/s}^{e/h}$	Effective mass of electron/hole in the core/shell
$\mathbf{M}$	Magnetization vector
M	Hole total angular momentum projection
n	Band index
n_l	Neumann function
n_r	Refractive index
N_B	Phonon occupation number
N^+, N^-	Occupation of exciton Zeeman split sublevels
N_{db}	Number of dangling bonds
N_{ex}	Number of excitons
$N_{\mathrm{ex},\pm 2}$	Occupation of Zeeman split dark exciton states ($F = +2$ and $F = -2$, respectively)
$N_{\mathrm{db}}^{\pm 2}$	Occupation of Zeeman split dangling bond states (Upper (+) and lower (−), respectively)
$\mathbf{p}$	Momentum operator

p_A	Population of the bright state
p_F	Population of the dark state
p_c	DCP of a single NC
p_c^{eq}	Equilibrium DCP of a single NC
P	Polarization, Power
P_c	Ensemble DCP
P_c^{eq}	Ensemble equilibrium DCP
P_c^{int}	Time-integrated ensemble DCP
P_l	Ensemble DLP
$\mathbf{r}$	Position operator
q	Phonon wavenumber
R_e	Dielectric enhancement factor
S	Shell thickness of a core/shell NC
$\mathbf{T}$	Lattice translation vector
T	Temperature
T_c	Critical temperature
T_1	Spin relaxation time
T_2	Spin dephasing time
V	Core volume, Potential
W	Width of a DiR
Y_{lm}	Spherical harmonics
α	Exchange strength constant for the electron-dangling bond interaction
$\alpha^{\|\|,\perp}$	Depolarization coefficients parallel and perpendicular with respect to the c-axis
β	Ratio of light and heavy hole effective masses
δ	Delta function
Δ	Total splitting between light and heavy hole bands in NCs
Δ_{cf}	Crystal field splitting in bulk material
Δ_{int}	Crystal field splitting in NCs
Δ_{sh}	Splitting due to shape anisotropy

Δ_{so}	Spin orbit splitting
ϵ_0	Vacuum permittivity ($8.85419 \cdot 10^{-12}$ F/m)
ϵ_{exch}	Exchange strength constant in CdSe
γ	Electron gyromagnetic ratio
Γ	Point of high symmetry in the first Brillouin zone
$\Gamma^{\pm 2}_{\text{flip-flop}}$	Dangling bond assisted radiative decay of the dark exciton ($F = +2$ or $F = -2$)
Γ_{20}	Coupling rate between $F = \pm 2$ and $F = 0$ states
Γ_{21}	Coupling rate between $F = \pm 2$ and $F = \pm 1$ states at $B \neq 0$ T
Γ^0_{21}	Coupling rate between $F = \pm 2$ and $F = \pm 1$ states at $B = 0$ T
Γ_A	Bright exciton radiative recombination rate
Γ_F	Dark exciton radiative recombination rate
Γ_{db}	Dangling bond assisted radiative recombination rate
$\Gamma^{\text{a}}_{\text{ph}}$	Acoustic phonon assisted radiative recombination rate
$\Gamma^{\text{o}}_{\text{ph}}$	Optical phonon assisted radiative recombination rate
Γ_r	Radiative decay rate
Γ_{nr}	Nonradiative decay rate
Γ^+, Γ^-	Spin flip rates between Zeeman sublevels
γ_0	Bright-dark spin flip rate at $T = 0$ K
γ_{db}	Dangling bond spin flip rate
η	Exchange strength constant for CdSe NCs
$\eta_{A,F}$	Quantum efficiencies of the bright and dark exciton state
κ_m	Dielectric constant of a medium
κ_s	Dielectric constant of a semiconductor
λ	Wavelength
μ	Ellipticity of a NC
μ_B	Bohr magneton ($5.78838 \cdot 10^{-5}$ eV/T)
Θ	Angle between the c-axis and the magnetic field
Θ_{e-h}	Electron-hole envelope wavefunction overlap
ρ_0	Exciton spin polarization in thermal equilibrium

ρ_{ex}	Exciton spin polarization
ρ_l	DLP of a single NC
$\rho_{l,0}^{\max}$	Maximum DLP of a single NC at $B = 0$ T
$\rho_l^{\max}$	Maximum DLP of a single NC at $B \neq 0$ T
ρ_{db}	Dangling bond spin polarization
$\overline{\rho}_{\mathrm{db}}$	Dangling bond spin polarization in thermal equilibrium
$\boldsymbol{\sigma}$	Spin operator
$\sigma+$, $\sigma-$	Circular polarization of light (right- and left-hand)
σ_{cr}	Absorption crosssection
τ_A	Bright exciton lifetime
τ_{AF}	Bright-dark spin flip time
τ_F	Dark exciton lifetime
τ_{db}	Dangling bond assisted radiative recombination time
τ_{nr}	Nonradiative decay time
τ_r	Radiative decay time
τ_s	Spin relaxation time
τ_0	Radiative lifetime of the $F = 0^U$ state
τ_{long}	Long decay time
τ_{short}	Short decay time
ω	Angular frequency
ω_{ex}	Excitation frequency
ψ, ϕ, ξ	Wavefunctions
∇	Nabla operator

List of Figures

List of Tables

Bibliography

[1] Y. Shirasaki, G. J. Supran, M. G. Bawendi, V. Bulović, Nat. Phot. **7**, 13 (2013).

[2] S. Pimputkar, J. S. Speck, S. P. Denbaars, S. Nakamura, Nat. Phot. **3**, 2-4 (2009).

[3] G. Konstantatos, I. Howard, A. Fischer, S. Hoogland, J. Clifford, E. Klem, L. Levina, E. Sargent, Nature **442**, 180 (2006).

[4] R. Rossetti, S. Nakahara, L. E. Brus, J. Chem. Phys. **79**, 1086 (1983).

[5] A. I. Ekimov, A. A. Onushchenko, Pis'ma Zh. Eksp. Teor. Fiz. **40**, 337 (1984).

[6] A. I. Ekimov, Al. L. Efros, A. A. Onushchenko, Solid State Commun. **88**, 947 (1985).

[7] T. Takagahara, Phys. Rev. B **47**, 4569 (1993).

[8] J. W. Haus, H. S. Zhou, I. Honma, H. Komiyama, Phys. Rev. B **47**, 1359 (1993).

[9] J. M. Caruge, J. E. Halpert, V. Wood, V. Bulović, M. G. Bawendi, Nat. Phot. **2**, 247 (2008).

[10] A. L. Rogach, N. Gaponik, J. M. Lupton, C. Bertoni, D. E. Gallardo, S. Dunn, N. L. Pira, M. Paderi, P. Repetto, S. G. Romanov, C. O'Dwyer, C. M. Sotomayor Torres, A. Eychmüller, Angew. Chem. Int. Ed. **47**, 6538 (2008).

[11] S. Coe-Sullivan, Nat. Phot. **3**, 315 (2009).

[12] K. Sanderson, Nature **459**, 760 (2009).

[13] V. Wood, V. Bulović, Nano reviews **1**, 1 (2010).

[14] H. Sargent, Nat. Phot. **6**, 133 (2012).

[15] K. Bourzac, Nature **493**, 283 (2013).

[16] R. M. Stevenson, R. J. Young, P. Atkinson, K. Cooper, D. A. Ritchie, A. J. Shields, Nature **439**, 179 (2006).

[17] D. Loss, D. P. DiVincenzo, Phys. Rev. A **57**, 120 (1998).

[18] S. A. Wolf, D. D. Awschalom, R. A. Buhrman, J. M. Daughton, S. von Molnár, M. L. Roukes, A. Y. Chtchelkanova, D. M. Treger, Science **294**, 1488 (2001).

[19] M. Kroutvar, Y. Ducommun, D. Heiss, M. Bichler, Nature **432**, 81 (2004).

[20] I. Zutic, J. Fabian, S. Das Sarma, Rev. Mod. Phys. **76**, 323 (2004).

[21] C. Chappert, A. Fert, F. N. Van Dau, Nat. Mater. **6**, 813 (2007).

[22] C. Kloeffel, D. Loss, Annu. Rev. Condens. Matter Phys. **4**, 51 (2013).

[23] T. Davis, Proc. Natl. Acad. Sci. USA **102**, 1277 (2005).

[24] D. V. Talapin, J. S. Lee, M. V. Kovalenko, E. V. Shevchenko, Chem. Rev. **110**, 389 (2010).

[25] Al. L. Efros in *Semiconductor Nanocrystals*, L. Tsybeskov, Al. L. Efros, D. J. Lockwood, (eds.), chap. 2 (Kluwer Academic/Plenum Publishers, New York, 2003).

[26] A. I. Ekimov, F. Hache, D. Ricard, C. Flytzanis, J. Opt. Soc. Am. **10**, 100 (1993).

[27] D. J. Norris, Al. L. Efros, M. Rosen, M. Bawendi, Phys. Rev. B **53**, 16347 (1996).

[28] Al. L. Efros, M. Rosen, M. Kuno, M. Nirmal, D. J. Norris, M. Bawendi, Phys. Rev. B **54**, 4843 (1996).

[29] M. Nirmal, D. J. Norris, M. Kuno, M. Bawendi, Phys. Rev. Lett. **75**, 3728 (1995).

[30] C. B. Murray, D. J. Norris, M. G. Bawendi, J. Am. Chem. Soc. **115**, 8706 (1993).

[31] D. V. Talapin, R. Koeppe, S. Go, A. Kornowski, J. M. Lupton, A. L. Rogach, O. Benson, J. Feldmann, H. Weller, Nano Lett. **3**, 1677 (2003).

[32] J. Hu, L. S. Li, W. Yang, L. Manna, L. Wang, A. P. Alivisatos, Science **292**, 2060 (2001).

[33] L. Spanhel, M. Haase, H. Weller, A. Henglein, J. Am. Chem. Soc. **109**, 5649 (1987).

[34] D. Dorfs, A. Eychmüller, Zeitschrift für Physikalische Chemie **220**, 1539 (2006).

[35] P. Reiss, M. Protiere, L. Li, Small **5**, 154 (2009).

[36] A. Piryatinski, S. A. Ivanov, S. Tretiak, V. I. Klimov, Nano Lett. **7**, 108 (2007).

[37] Y. Chen, J. Vela, R. D. Schaller, J. A. Hollingsworth, V. I. Klimov, Nano Lett. **9**, 3482 (2009).

[38] S. Brovelli, R. D. Schaller, S. A. Crooker, F. García-Santamaría, Y. Chen, R. Viswanatha, J. A. Hollingsworth, H. Htoon, V. I. Klimov, Nat. Commun. **2**, 280 (2011).

[39] J. M. Elzerman, R. Hanson, L. H. Willems van Beveren, B. Witkamp, L. M. K. Vandersypen, L. P. Kouwenhoven, Nature **430**, 431 (2004).

[40] D. Heiss, M. Kroutvar, J. J. Finley, G. Abstreiter, Solid State Commun. **135**, 591 (2005).

[41] J. Berezovsky, O. Gywat, F. Meier, D. Battaglia, X. Peng, D. D. Awschalom, Nat. Phys. **2**, 831 (2006).

[42] R. Beaulac, L. Schneider, P. I. Archer, G. Bacher, D. R. Gamelin, Science **325**, 973 (2009).

[43] E. Johnston-Halperin, D. Awschalom, S. Crooker, Al .L. Efros, M. Rosen, X. Peng, A. Alivisatos, Phys. Rev. B **63**, 205309 (2001).

[44] M. Furis, J. A. Hollingsworth, V. I. Klimov, S. A. Crooker, J. Phys. Chem. B **109**, 15332 (2005).

[45] F. Wijnen, J. Blokland, P. Chin, P. Christianen, J. Maan, Phys. Rev. B **78**, 235318 (2008).

[46] D. Kovalev, B. Averboukh, M. Ben-Chorin, F. Koch, Al. L. Efros, M. Rosen, Phys. Rev. Lett. **77**, 2089 (1996).

[47] A. Shabaev, Al. L. Efros, Nano Lett. **4**, 1821 (2004).

[48] M. Nirmal, C.B. Murray, M.G. Bawendi, Phys. Rev. B **50**, 2293 (1994).

[49] B. A. Ridley, B. Nivi, J. M. Jacobson, Science **286**, 746 (1999).

[50] B. O. Dabbousi, F. V. Mikulec, J. R. Heine, H. Mattoussi, R. Ober, K. F. Jensen, M. G. Bawendi, J. Phys. Chem. B **9463**, 9463 (1997).

[51] P. Reiss, J. Bleuse, A. Pron, Nano Lett. **2**, 781 (2002).

[52] X. Peng, L. Manna, W. Yang, J. Wickham, E. Scher, A. Kadavanich, A. P. Alivisatos, Nature **404**, 59 (2000).

[53] A. Kobayashi, F. Sankey, S. M. Volz, J. D. Dow, Phys. Rev. B **28**, 935 (1983).

[54] S. Adachi, *Handbook on Physical Properties of Semiconductors* (Springer US, 2004).

[55] N. W. Ashcroft, D. N. Mermin, *Solid State Physics* (Holt, Rinehart and Winston, New York, 1976).

[56] J. J. Hopfield, J. Phys. Chem. Solids **15**, 97 (1960).

[57] L. C. Lew Yan Voon, M. Willatzen, M. Cardona, N. E. Christensen, Phys. Rev. B **53**, 10703 (1996).

[58] C. F. Klingshirn, *Semiconductor Optics* (Springer, Berlin Heidelberg, 1995).

[59] R. Winkler, *Spin-Orbit Coupling Effects in Two-Dimensional Electron and Hole Systems* (Springer, Berlin, 2003).

[60] G. F. Koster, J. O. Dimmock, R. C. Wheeler, H. Statz, *Properties of the thirty-two point groups* (MIT Press, Cambridge, 1969), 3. edn.

[61] D. C. Reynolds, C. W. Litton, T. C. Collins, Phys. Status Solidi B **9**, 645 (1965).

[62] S. Gasiorowicz, *Quantenmechanik* (Oldenbourg Wissenschaftsverlag GmbH, Oldenbourg, 2002), 8. edn.

[63] M. G. Burt, J. Phys. - Condens. Mat. **4**, 6651 (1992).

[64] M. G. Burt, Appl. Phys. Lett. **65**, 717 (1994).

[65] F. Garcia-Santamaria, Y. Chen, J. Vela, R. D. Schaller, J. A. Hollingsworth, V. I. Klimov, Nano Lett. **9**, 3482 (2009).

[66] S. Brovelli, R. D. Schaller, S. A. Crooker, F. García-Santamaría, Y. Chen, R. Viswanatha, J. A. Hollingsworth, H. Htoon, V. I. Klimov, Nat. Commun. **2**, 280 (2011).

[67] K. Leung, S. Pokrant, K. B. Whaley, Phys. Rev. B **57** (1998).

[68] A. Franceschetti, H. Fu, L. Wang, A. Zunger, Phys. Rev. B **60**, 1819 (1999).

[69] Al. L. Efros, Phys. Rev. B **46**, 7448 (1992).

[70] Al. L. Efros, Phys. Rev. B **47**, 5 (1993).

[71] M. I. Dyakonov, *Spin Physics in Semiconductors* (Springer-Verlag, Berlin Heidelberg, 2008).

[72] V. Kiselev, B. S. Razbirin, I. N. Uraltsev, Phys. Status Solidi B **72**, 161 (1975).

[73] M. Chamarro, C. Gourdon, P. Lavallard, O. Lublinskaya, A. I. Ekimov, Phys. Rev. B **53**, 1336 (1996).

[74] F. Liu, *Magneto-optical properties of II-VI semiconductor colloidal nanostructures*, Ph.D. thesis, Technische Universität Dortmund (2013).

[75] J. Gupta, D. Awschalom, Al. L. Efros, A. Rodina, Phys. Rev. B **66**, 125307 (2002).

[76] A. J. Nozik, Annu. Rev. Phys. Chem. **52**, 193 (2001).

[77] M. Fox, *Optical properties of solids* (Oxford University Press, Oxford, 2010), 2 edn.

[78] V. I. Klimov in *Semiconductor and Metal Nanocrystals*, V. I. Klimov, (ed.), chap. 5 (Taylor & Francis, 2003).

[79] U. Bockelmann, Phys. Rev. B **42**, 8947 (1990).

[80] H. Benisty, C. M. Sotomayor-Torres, C. Weisbuch, Phys. Rev. B **44**, 8 (1991).

[81] T. Inoshita, H. Sakaki, Phys. Rev. B **46**, 7260 (1992).

[82] U. Woggon, F. Gindele, O. Wind, C. Klingshirn, Phys. Rev. B **54**, 1506 (1996).

[83] L. Saviot, E. Duval, A. Kudriavtsev, J. Non-Cryst. Solids **197**, 238 (1996).

[84] D. Oron, A. Aharoni, C. de Mello Donegá, J. van Rijssel, A. Meijerink, U. Banin, Phys. Rev. Lett. **102**, 177402 (2009).

[85] M. J. Fernée, C. Sinito, Y. Louyer, C. Potzner, T. L. Nguyen, P. Mulvaney, P. Tamarat, B. Lounis, Nat. Commun. **3**, 1287 (2012).

[86] Al. L. Efros, V. A. Kharchenko, M. Rosen, Solid State Commun. **93**, 281 (1995).

[87] V. I. Klimov, D. W. McBranch, Phys. Rev. Lett. **80**, 16 (1998).

[88] V. I. Klimov, A. A. Mikhailovsky, D. W. McBranch, C. A. Leatherdale, M G. Bawendi, Phys. Rev. B **61**, 349 (2000).

[89] V. A. Kharchenko, M. Rosen, Journal of Luminescence **70**, 158 (1996).

[90] M. Fox, *Quantum optics* (Oxford University Press, Oxford, 2006).

[91] J. Fabian, S. Das Sarma, J. Vac. Sci. Technol. **17**, 1708 (1999).

[92] M. Z. Maialle, Phys. Rev. B **61**, 877 (2000).

[93] R. I. Dzhioev, B. P. Zakharchenya, E. L. Ivchenko, V. L. Korenev, JETP Letters **65**, 804 (1997).

[94] I. A. Merkulov, Al. L. Efros, M. Rosen, Phys. Rev. B **65**, 205309 (2002).

[95] E. Tsitsishvili, R. Baltz, H. Kalt, Phys. Rev. B **67**, 205330 (2003).

[96] M. Z. Maialle, E. A. de Andrada e Silva, L. J. Sham, Phys. Rev. B **47**, 776 (1993).

[97] S. V. Goupalov, E. L. Ivchenko, Journal of Crystal Growth **184-185**, 393 (1998).

[98] S. V. Goupalov, Phys. Rev. B **74**, 113305 (2006).

[99] M. Furis, H. Htoon, M. Petruska, V. I. Klimov, T. Barrick, S. A. Crooker, Phys. Rev. B **73**, 241313 (2006).

[100] H. Htoon, S. A. Crooker, M. Furis, S. Jeong, Al. L. Efros, V. I. Klimov, Phys. Rev. Lett. **102**, 017402 (2009).

[101] S. V. Goupalov, Phys. Rev. B **79**, 233301 (2009).

[102] A. G. del Águila, B. Jha, F. Pietra, E. Groeneveld, C. de Mello Donegá, J. C. Maan, P. C. M. Christianen, ACS Nano **8**, 5921 (2014).

[103] F. Liu, L. Biadala, A. V. Rodina, D. R. Yakovlev, D. Dunker, C. Javaux, J. P. Hermier, Al. L. Efros, B. Dubertret, M. Bayer, Phys. Rev. B **88**, 035302 (2013).

[104] Z. Hens, I. Moreels, J. Mater. Chem. **22**, 10406 (2012).

[105] J. A. Osborn, Phys. Rev. **67**, 351 (1945).

[106] W. Becker, *Advanced Time-Correlated Single Photon Counting Techniques* (Springer, Berlin Heidelberg New York, 2005).

[107] J. Jasieniak, L. Smith, J. V. Embden, P. Mulvaney, M. Califano, J. Phys. Chem. C **113**, 19468 (2009).

[108] L. Carbone, C. Nobile, M. De Giorgi, F. D. Sala, G. Morello, P. Pompa, M. Hytch, E. Snoeck, A. Fiore, I. R. Franchini, M. Nadasan, A. F. Silvestre, L. Chiodo, S. Kudera, R. Cingolani, R. Krahne, L. Manna, Nano Lett. **7**, 2942 (2007).

[109] M. Cirillo, T. Aubert, R. Gomes, R. Van Deun, P. Emplit, A. Biermann, H. Lange, C. Thomsen, E. Brainis, Z. Hens, Chem. Mater. **26**, 1154 (2014).

[110] L. Biadala, B. Siebers, R. Gomes, Z. Hens, D. R. Yakovlev, M. Bayer, J. Phys. Chem. C **118**, 22309 (2014).

[111] F. T. Kämmerer, *Influence of the Shell Size and Shape on the Recombination Dynamics and Fine Structure of Core/Shell Dot-in-Rod and Dot-in-Plate Nanocrystals*, Master thesis, Technische Universität Dortmund (2014).

[112] Y. Luo, L. W. Wang, ACS Nano **4**, 91 (2010).

[113] J. Müller, J. M. Lupton, P. G. Lagoudakis, F. Schindler, R. Koeppe, A. L. Rogach, J. Feldmann, D. V. Talapin, H. Weller, Nano Lett. **5**, 2044 (2005).

[114] D. Steiner, D. Dorfs, U. Banin, F. Della Sala, L. Manna, O. Millo, Nano Lett. **8**, 2954 (2008).

[115] G. Rainò, T. Stöferle, I. Moreels, R. Gomes, J. S. Kamal, Z. Hens, R. F. Mahrt, ACS Nano **5**, 4031 (2011).

[116] O. Labeau, Ph. Tamarat, B. Lounis, Phys. Rev. Lett. **90**, 257404 (2003).

[117] C. de Mello Donegá, M. Bode, A. Meijerink, Phys. Rev. B **74**, 085320 (2006).

[118] C. She, A. Demortiere, E. V. Shevchenko, M. Pelton, J. Phys. Chem. Lett. **2**, 1469 (2011).

[119] L. Biadala, Y. Louyer, Ph. Tamarat, B. Lounis, Phys. Rev. Lett. **103**, 037404 (2009).

[120] L. Biadala, Y. Louyer, Ph. Tamarat, B. Lounis, Phys. Rev. Lett. **105**, 157402 (2010).

[121] R. W. Meulenberg, J. R. I. Lee, S. K. McCall, K. M. Hanif, D. Haskel, J. C. Lang, L. J. Terminello, T. van Buuren, J. Am. Chem. Soc. **131**, 6888 (2009).

[122] S. Neeleshwar, C. Chen, C. Tsai, Y. Chen, S. Shyu, M. Seehra, Phys. Rev. B **71**, 201307 (2005).

[123] S. A. Crooker, T. Barrick, J. A. Hollingsworth, V. I. Klimov, Appl. Phys. Lett. **82**, 2793 (2003).

[124] G. Rainò, T. Stöferle, I. Moreels, R. Gomes, Z. Hens, R. F. Mahrt, ACS Nano **6**, 1979 (2012).

[125] Al. L. Efros, M. Rosen, Annu. Rev. Mat. Sci. **30**, 475 (2000).

[126] A. Franceschetti, L. W. Wang, H. Fu, A. Zunger, Phys. Rev. B **58**, 367 (1998).

[127] H. Eshet, M. Grünwald, E. Rabani, Nano Lett. **13**, 5880 (2013).

[128] D. C. Hannah, N. J. Dunn, S. Ithurria, D. V. Talapin, L. X. Chen, M. Pelton, G. C. Schatz, R. D. Schaller, Phys. Rev. Lett. **107**, 177403 (2011).

[129] G. D. Scholes, J. Kim, C. Y. Wong, Phys. Rev. B **73**, 195325 (2006).

[130] G. D. Scholes, J. Kim, C. Y. Wong, V. M. Huxter, P. S. Nair, K. P. Fritz, S. Kumar, Nano Lett. **6**, 1765 (2006).

[131] J. Kim, C. Y. Wong, P. S. Nair, K. P. Fritz, S. Kumar, G. D. Scholes, J. Phys. Chem. B **110**, 25371 (2006).

[132] J. He, S. S. Lo, J. Kim, G. D. Scholes, Nano Lett. **8**, 4007 (2008).

[133] J. Kim, C. Y. Wong, G. D. Scholes, Acc. Chem. Res. **42**, 1037 (2009).

[134] C. Y. Wong, J. Kim, P. S. Nair, M. C. Nagy, G. D. Scholes, J. Phys. Chem. C **113**, 795 (2009).

[135] F. Liu, A. V. Rodina, D. R. Yakovlev, A. Greilich, A. A. Golovatenko, A. S. Susha, A. L. Rogach, Y. G. Kusrayev, M. Bayer, Phys. Rev. B **89**, 115306 (2014).

[136] N. R. Jana, Angew. Chem. Int. Ed. **43**, 1536 (2004).

[137] X. Wang, C. J. Summers, Z. Lin. Wang, Nano Lett. **4**, 423 (2004).

[138] A. Ghezelbash, B. Koo, B. A. Korgel, Nano Lett. **6**, 1832 (2006).

[139] K. M. Ryan, A. Mastroianni, K. A. Stancil, H. Liu, A. P. Alivisatos, Nano Lett. **6**, 1479 (2006).

[140] C. Nobile, L. Carbone, A. Fiore, R. Cingolani, L. Manna, R. Krahne, J. Phys.: Condens. Matter **21**, 264013 (2009).

[141] R. D. Deegan, O. Bakajin, T. F. Dupont, Nature **389**, 827 (1997).

[142] M. Zavelani-Rossi, M. G. Lupo, R. Krahne, L. Manna, G. Lanzani, Nanoscale **2**, 931 (2010).

[143] X. Wang, X. Ren, K. Kahen, M. A. Hahn, M. Rajeswaran, S. Maccagnano-Zacher, J. Silcox, G. E. Cragg, Al. L. Efros, T. D. Krauss, Nature **459** (2009).

[144] P. A. Knipp, T. L. Reinecke, Phys. Rev. B **52**, 5923 (1995).

[145] P. A. Knipp, T. L. Reinecke, Solid-State Electron. **40**, 343 (1996).

[146] A. M. Alcalde, G. E. Marques, G. Weber, T. L. Reinecke, Solid State Commun. **116**, 247 (2000).

[147] A. M. Alcalde, G. E. Marques, G. Weber, T. L. Reinecke, Physica B: Condensed Matter **316-317**, 459 (2002).

[148] L. Woods, T. L. Reinecke, Y. Lyanda-Geller, Phys. Rev. B **66**, 161318 (2002).

[149] L. Woods, T. L. Reinecke, R. Kotlyar, Phys. Rev. B **69**, 125330 (2004).

[150] B. L. Gel'mont, M. I. D'yakonov, Sov. Phys. Semicond. **7**, 1345 (1973).

[151] A. V. Rodina, Al. L. Efros, A. Alekseev, Phys. Rev. B **67**, 155312 (2003).

[152] D. R. Yakovlev, A. V. Platonov, E. L. Ivchenko, V. P. Kochereshko, C. Sas, W. Ossau, L. Hansen, A. Waag, G. Landwehr, L. W. Molenkamp, Phys. Rev. Lett. **88**, 257401 (2002).

[153] F. Pisanello, L. Martiradonna, G. Lemenager, P. Spinicelli, A. Fiore, L. Manna, J. P. Hermier, R. Cingolani, E. Giacobino, M. De Vittorio, A. Bramati, Appl. Phys. Lett. **96**, 033101 (2010).

[154] I. Hadar, G. B. Hitin, A. Sitt, A. Faust, U. Banin, J. Phys. Chem. Lett. **4**, 502 (2013).

[155] B. T. Diroll, A. Koschitzky, C. B. Murray, J. Phys. Chem. Lett. **5**, 85 (2014).

[156] S. A. Empedocles, R. Neuhauser, M G. Bawendi, Nature **399**, 126 (1999).

[157] A. V. Rodina, Al. L. Efros, unpublished .

[158] Al. L. Efros in *Semiconductor and Metal nanocrystals: Synthesis and Electronic and Optical Properties*, V. I. Klimov, (ed.), 103-141 (New York, 2003).

[159] M. J. Fernee, Ph. Tamarat, B. Lounis, J. Phys. Chem. Lett. **4**, 609 (2013).

[160] B. E. Kane, Nature **393**, 133 (1998).

[161] M. W. Wu, J. H. Jiang, M. Q. Weng, Physcis reports **493**, 61 (2010).

[162] E. Poem, Y. Kodriano, C. Tradonsky, N. H. Lindner, B. D. Gerardot, P. M. Petroff, D. Gershoni, Nat. Phys. **6**, 993 (2010).

[163] C. A. Leatherdale, W. -K. Woo, F. V. Mikulec, M. G. Bawendi, J. Phys. Chem. B **106**, 7619 (2002).

[164] X. Peng, Chem. Eur. J. **8**, 334 (2002).

[165] S. Xu, J. Ziegler, T. Nann, J. Mater. Chem. **13**, 2653 (2008).

[166] S. Haubold, M. Haase, A. Kornowski, H. Weller, ChemPhysChem **2**, 331 (2001).

[167] D. Battaglia, X. Peng, Nano Lett. **2**, 1027 (2002).

[168] L. Li, P. Reiss, J. Am. Chem. Soc. **130**, 11588 (2008).

[169] X. Yang, D. Zhao, K. S. Leck, S. T. Tan, Y. X. Tang, J. Zhao, H. V. Demir, X. W. Sun, Advanced Materials **24**, 4180 (2012).

Publications and conference contributions

List of publications

- L. Biadala, B. Siebers, R. Gomes, Z. Hens, D. R. Yakovlev, and M. Bayer **Tuning Energy Splitting and Recombination Dynamics of Dark and Bright Excitons in CdSe/CdS Dot-in-Rod Colloidal Nanostructures** J. Phys. Chem. C 2014, 118, 22309-22316
- B. Siebers, L. Biadala, T. Aubert, Z. Hens, A. V. Rodina, D. R. Yakovlev, and M. Bayer **Exciton spin dynamics and photoluminescence polarization in CdSe/CdS dot-in-rod nanocrystals in high magnetic fields** Submitted to Phys. Rev. B
- B. Sacca, B. Siebers, R. Meyer, M. Bayer, and C. M. Niemeyer **Nanolattices of Switchable DNA-Based Motors** Small 2012, 8, 19, 3000-3008

Conference contributions

- Mai 2012: **Regular talk**, Nanoscience with Nanocrystals 5 (NANAX 5), Fuengirola, Spain. *Spin dynamics in CdSe/CdS colloidal nanocrystals.*
- Mai 2014: **Poster**, Nanoscience with Nanocrystals 6 (NANAX 6), Bad Hofgastein, Austria. *Tuning energy splitting and recombination dynamics of dark and bright excitons in CdSe/CdS dot-in-rod colloidal nanostructures.*

Acknowledgments

Finally i want to thank the people, without whose support it would not have been possible to write this thesis.

- My family, Sarina and friends: Thank you for your love or friendship and for your support over the years! I am glad to have you!
- Manfred Bayer and Dmitri Yakovlev: Thank you for the opportunity to work at E2 and for your guidance!
- Louis Biadala: Many thanks for the nice time together in the lab and for your assistance and advice in scientific matters.
- Anna Rodina: Thank you for your contributions to our projects, for your scientific advice and nice correspondences.
- Tangi Aubert: Thank you for your incredible fast supply of samples!
- Johannes Schmutzler: Thank you for a great time in the office and elsewhere, for your support and much else...
- E2 colleagues: Thank you for the good time!